UNIVERSITY OF CALIFORNIA, SAN DIEGO

Interactions of Mesoscale Ocean Dynamics with Large-Scale Ocean and Climate Variability: Case Studies in the Mid-Latitude Pacific and Tropical Indian Oceans

A Dissertation submitted in partial satisfaction of the
requirements for the degree
Doctor of Philosophy

in

Oceanography

by

Andrew Spencer Delman

Committee in charge:

Julie McClean, Co-Chair
Janet Sprintall, Co-Chair
Lynne Talley, Co-Chair
Frank Bryan
David Checkley
Graham Elliott
Shang-Ping Xie

2016

The Dissertation of Andrew Spencer Delman is approved, and it is acceptable in quality and form for publication on microfilm and electronically:

_____

_____

_____

_____

_____
Co-Chair

_____
Co-Chair

_____
Co-Chair

University of California, San Diego

2016

DEDICATION

To Michele Dufault, who saw the wonder in the stars, and the magic in the oceans.

TABLE OF CONTENTS

LIST OF FIGURES

LIST OF TABLES

ACKNOWLEDGEMENTS

Thanks are due, first and foremost, to my advising team of Janet Sprintall, Julie McClean, and Lynne Talley. They have been indispensable; supporting me in my own scientific inquiries, while helping me refine my data analysis skills and hone my craft as a scientific writer. Their dedication to oceanography is endlessly inspiring.

I am quite thankful for my other committee members, Frank Bryan, Dave Checkley, Graham Elliott, and Shang-Ping Xie, for offering helpful commentary and their diverse perspectives on my work, and I also greatly appreciate Elena Yulaeva and Caroline Papadopoulos for their help with the technicalities of obtaining and using model output. Some of the classroom instruction that I had at Scripps was vital to shaping the approaches used in my thesis work, and I am particularly grateful for my experiences in Dan Rudnick's and Sarah Gille's classes. I was fortunate enough to have the chance to spend some time in residence at NCAR through the SUNNY program; this experience shaped my understanding of how ocean models actually work, and I am especially thankful to Frank Bryan and Justin Small for their collaboration during those visits. My appreciation also extends to Andy Thompson and the other researchers and crew involved with ChinStrAP for helping me get my sea legs.

Finally, I owe a debt of gratitude to those who have both gotten me through my thesis work and away from it sometimes: the PO class of 2009, the TG crowd, and my future in-laws for making San Diego a true home for this East Coast transplant. To my parents, and my godmother Rosemary: your joy and support in every step I take has been my foundation ever since I first became curious when looking at a map, until today. And of course, to my incredible fiancée Stacie: I can hardly imagine the journey of these past few years without you. Thank you.

Chapter 2, in full, is a reprint of the material as it appears in the Journal of Physical Oceanography, 2015, Delman, A. S., McClean, J. L., Sprintall, J., Talley, L. D., Yulaeva, E., and S. R. Jayne, copyright 2015 American Meteorological Society. I was the primary investigator and author of this manuscript; the co-authors supervised the preparation of the manuscript, and/or were responsible for running the model simulation that was used in the analysis.

Chapter 3, in full, consists of material that has been submitted for publication in Ocean Science, by Delman, A. S., Sprintall, J., McClean, J. L., and L. D. Talley. I was the primary investigator and author of this paper; the co-authors supervised and assisted with the preparation of the manuscript.

Chapter 4, in full, consists of material that is in revision for publication in the Journal of Geophysical Research: Oceans, by Delman, A. S., Sprintall, J., McClean, J. L., and L. D. Talley. I was the primary investigator and author of this paper; the co-authors supervised and assisted with the preparation of the manuscript.

Chapter 5, in full, is currently being prepared for submission for publication of the material, by Delman, A. S., McClean, J. L., Sprintall, J., Talley, L. D., and F. O. Bryan. I was the primary investigator and author of this paper; the co-authors supervised and assisted with the preparation of the manuscript, and helped with understanding the methodology of computations using the model output.

VITA

2009	B. S. in Geology and Geophysics *magna cum laude*, Yale University, New Haven, Connecticut
2010	M. S. in Oceanography, University of California-San Diego, La Jolla, California
2016	Ph. D. in Oceanography, University of California-San Diego, La Jolla, California

PUBLICATIONS

Delman, A. S., J. Sprintall, J. L. McClean, and L. D. Talley (2016). A harmonic projection and least-squares method for quantifying Kelvin wave activity, *Ocean Sci.*. Submitted.

Delman, A. S., J. Sprintall, J. L. McClean, and L. D. Talley (2016). Anomalous Java cooling at the initiation of positive Indian Ocean Dipole events, *J. Geophys. Res. Oceans*. In revision.

Delman, A. S., J. L. McClean, J. Sprintall, L. D. Talley, E. Yulaeva, and S. R. Jayne (2015). Effects of eddy vorticity forcing in the Kuroshio Extension, *J. Phys. Oceanogr.*, *45,* 1356–1375.

ABSTRACT OF THE DISSERTATION

Interactions of Mesoscale Ocean Dynamics with Large-Scale Ocean and Climate Variability: Case Studies in the Mid-Latitude Pacific and Tropical Indian Oceans

by

Andrew Spencer Delman

Doctor of Philosophy in Oceanography

University of California, San Diego, 2016

Julie McClean, Co-Chair
Janet Sprintall, Co-Chair
Lynne Talley, Co-Chair

The large-scale climate system is driven by imbalances of the reservoirs of heat contained in the world oceans. The transport and redistribution of this heat is determined in part by nonlinear mesoscale eddies (radii ∼50–200 km), as well as by planetary waves whose widths approach the size of mesoscale eddies away from the equator. In this dissertation, new analysis techniques are developed and implemented to assess oceanic phenomena in two regions: mesoscale eddy-mean flow interaction

in the Kuroshio Extension (KE) region, and the effects of coastal Kelvin waves and mesoscale eddies in the Indian Ocean south of Java. In the KE region, a jet-following coordinate reference frame is used to quantify the contributions of eddies to the vorticity budget along the KE jet in a strongly eddying ocean general circulation model simulation, the Parallel Ocean Program (POP). The jet reference frame preserves synoptic gradients of the jet that are not accurately represented in multi-year Eulerian means. This analysis found that eddies tend to accelerate the jet just downstream of crests in the topographically-induced meanders, implying an intensification of frontal gradients in these areas. In the Indian Ocean, a method involving projections of harmonic basis functions onto altimetry-derived sea level anomaly (SLA) is used to estimate Kelvin wave activity along the equatorial-coastal waveguide. The resulting Kelvin wave coefficient presents a more accurate representation of Kelvin wave activity than that from raw SLA. Moreover, values of the Kelvin wave coefficient in April-June are a robust predictor of positive Indian Ocean Dipole (pIOD) event development later in the calendar year. Finally, a temperature budget using a strongly eddying POP simulation isolates the specific contributions of mesoscale processes south of Java. It shows that Kelvin waves and local wind forcing both contribute substantially to anomalous cooling during pIOD years, while mesoscale eddies have a modest warming effect. These results suggest that mesoscale processes in the study regions have an important influence on the ocean's structure and can trigger a climate response; use of the new analysis techniques may help quantify the effects of mesoscale eddies and planetary waves elsewhere in the oceans.

Chapter 1

Introduction

In recent decades, studies of mesoscale ocean processes (with spatial scales of tens to hundreds of kilometers and temporal scales of weeks to months) have highlighted their important role in maintaining the large-scale state of the ocean, and suggested potentially coupled interactions with the atmosphere. Until the late 20th century, most research in the field of physical oceanography focused on describing and explaining the large, generally steady features in ocean basins (e.g., the subtropical and subpolar gyres, the global oceanic conveyor belt, transport of water masses), as well as features readily observable from ships and shore-based instruments (e.g., tides, surface gravity waves). The beginning of the era of satellite oceanography in the 1980s and 1990s revealed that transient mesoscale features are far more prevalent in the ocean than previously thought (Figure 1.1). As the spatial resolution of data collection and of ocean general circulation models (GCMs) has increased, mesoscale processes have been shown to produce leading-order contributions to the transport of heat, salt, vorticity, and other tracers in the global oceans (e.g., Wunsch, 1999; Williams et al., 2007). Moreover, the upper ocean's temperature and heat content plays a large part

in driving interannual and decadal variability of the climate system. The Bjerknes feedback, in which zonal atmospheric winds near the equator respond to sea surface temperature (SST) changes (Bjerknes, 1969), is a key mechanism for the evolution of the El Niño/Southern Oscillation. Other climate modes such as the Pacific Decadal Oscillation (Mantua et al., 1997) and Indian Ocean Dipole (Saji et al., 1999) have also been identified that are dependent on the distribution of SSTs. Many of the changes in SSTs that spur transitions in these climate modes appear to be driven by transient mesoscale features, rather than (or in addition to) changes in long-term mean ocean currents.

Mesoscale ocean dynamics manifest in different ways depending on the latitude of their formation. Poleward of about 10° latitude, the most potent mesoscale dynamics are found in closed rings or eddies; the strongest eddies are usually generated by barotropic and baroclinic instability near strong current shear and density gradients, though variations in wind stress curl can also induce eddy development. Once generated, the stability of an eddy is maintained by predominantly geostrophic flow around a central cold or warm core, and its dynamics are highly nonlinear, since the ratio of the flow speed rotating around an eddy is generally much higher than the speed that the eddy moves through the ocean (Figure 1.2, reproduced from Chelton et al., 2011). Within 5°–10° latitude of the equator, geostrophic adjustment happens too slowly and the translation speeds of pressure/vorticity anomalies are too slow to support the development of closed geostrophic rings; instead, wind-forced quasi-geostrophic planetary waves with stronger linear dynamics are prevalent. Planetary waves such as Kelvin and Rossby waves, also known as equatorial long waves near the equator, are often not considered to be mesoscale processes because their zonal length scales

can span most or all of an ocean basin. However, they are also highly anisotropic, with their meridional widths (hundreds of kilometers) much shorter than their zonal lengths. Furthermore, in this study we will be considering an off-equatorial area where an equatorial Kelvin wave continues propagating poleward along a coastline as a coastal Kelvin wave. As these Kelvin waves propagate away from the equator, their cross-shore width is set by the Rossby radius of deformation, which is comparable to the radius of mesoscale eddies at similar latitudes ($\sim$100–200 km). Hence, for the purposes of this study, I consider both nonlinear eddies and (mostly) linear Kelvin waves to be responsible for mesoscale dynamical processes.

This thesis seeks to identify or clarify connections between mesoscale processes and spatial or temporal variations in large-scale ocean and climate phenomena, in two specific regions of the ocean. In this work, I address questions such as: Are the mesoscale dynamics associated with eddies or Kelvin waves in these regions sufficient to account for features of the ocean's flow structure and climate variability? Can statistical relationships and budget computations provide confident assessments about the impacts of mesoscale processes, using the latest generation of observational datasets and ocean general circulation model (OGCM) simulations?

The first region studied in this thesis is along the energetic western boundary extension of the Kuroshio Current right after it separates from the coast of Japan; this area has the highest eddy activity levels in the North Pacific (Figure 1.3, upper box). Chapter 2 of the thesis uses 13 years of output from an ocean GCM to quantify the upper ocean vorticity budget and study the interactions between mesoscale eddies and the mean flow (Delman et al., 2015). Since the Kuroshio Extension jet both advects heat and acts as a barrier for cross-jet heat fluxes, the effect of eddies on the mean jet

flow's evolution influences the movement of heat through the region, which in turn may affect the atmospheric state over the North Pacific (e.g., Yulaeva et al., 2001; Kwon et al., 2011). The remainder of the thesis focuses on a region of the Indian Ocean near the south coast of Java (Figure 1.3, lower box), where both coastal Kelvin waves and mesoscale eddies are active. Chapter 3 presents a new method for quantifying equatorial and coastal Kelvin wave activity from satellite-measured sea surface height displacements, based on the projections of idealized wave profiles and a least-squares fitting technique (Delman et al., 2016a). Chapter 4 uses the method described in Chapter 3, along with other satellite and in-situ measurements of winds and ocean temperatures, to determine the degree to which wind forcing and Kelvin wave activity are effective predictors of the SST near Java and the Indian Ocean Dipole (IOD) climate mode (Delman et al., 2016b). Chapter 5 analyzes the surface mixed layer temperature budget south of Java using 31 years of ocean GCM output, including 8 positive IOD events; the objective of this chapter is to quantify the contributions of specific mesoscale processes (Kelvin waves and eddies) and the local wind forcing to anomalous SST cooling. Finally, Chapter 6 summarizes the key results of the thesis, and presents a few new research questions raised by this work.

A secondary objective of this thesis is to introduce new frameworks to estimate the specific influence of a mesoscale process. In each of the science chapters of this thesis (Chapters 2–5), I discuss and utilize a new analysis technique in order to target the effects of a specific process on the ocean state. In Chapter 2, I developed a jet-following reference frame or coordinate system to isolate the contributions to the mean flow from eddy activity unrelated to variations with the jet position. Chapter 3 is entirely focused on describing and assessing a new technique to quantify the

relative amplitudes of Kelvin waves, while Chapter 4 makes use of this technique to associate Kelvin waves with Indian Ocean Dipole predictability. Chapter 5 uses the regression of proxy indices for Kelvin wave, mesoscale eddies, and wind stress to isolate the contributions of each of these processes to mixed layer temperature change. By using these frameworks in combination with mesoscale-resolving datasets and OGCM simulations, researchers can understand the character and variations of mesoscale–large scale interactions in the global ocean, and the impacts of these interactions on climate.

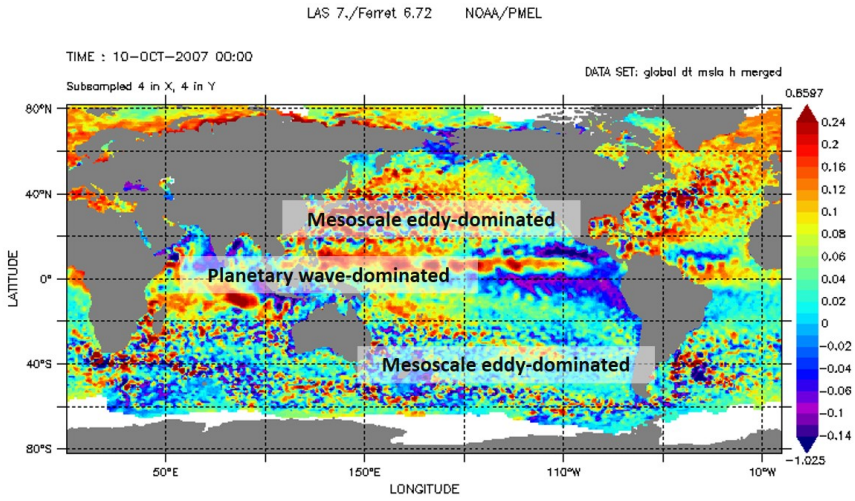

Figure 1.1: Snapshot of sea level anomaly (cm) of the surface of the ocean, on 10 October 2007, from AVISO satellite altimetry data. Annotations indicate the latitudes in which ocean variability is dominated by mesoscale eddies and planetary waves. This figure was generated on 4 April 2016, using the Live Access Server version 7.1 maintained by NOAA PMEL and hosted at http://las.aviso.altimetry.fr.

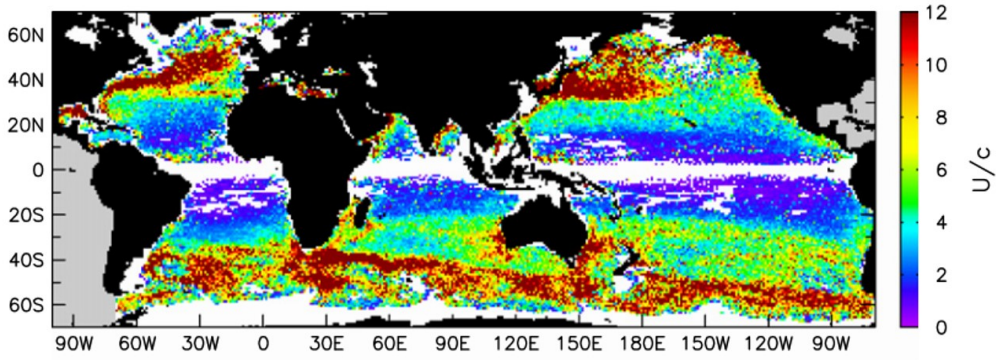

Figure 1.2: The eddy nonlinearity parameter U/c, computed as the ratio between the maximum rotational eddy flow speed U and the translation speed c of the eddy. This figure is taken directly from Chelton et al. (2011), Figure 17a.

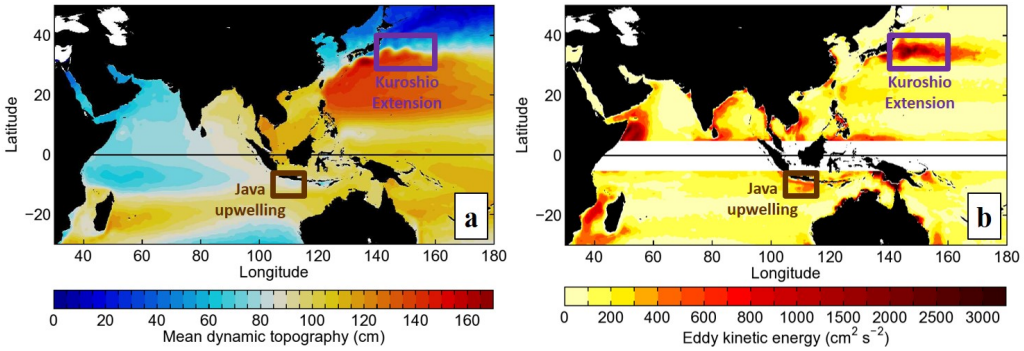

Figure 1.3: (a) The mean dynamic topography at the surface of the ocean, computed from AVISO data spanning the years 1993–2014. (b) Mean eddy kinetic energy at the ocean surface, computed from the horizontal gradients of AVISO absolute dynamic topography data with the 1993–2014 mean removed; values are not shown equatorward of 5° latitude due to the collapse of the geostrophic approximation. The two focus regions for this thesis are indicated, i.e., the Kuroshio Extension (purple box) and Java upwelling (brown box) regions.

Chapter 2

Effects of eddy vorticity forcing on the mean state of the Kuroshio Extension

Abstract

Eddy-mean flow interactions along the Kuroshio Extension (KE) jet are investigated using a vorticity budget of a high-resolution ocean model simulation, averaged over a 13-year period. The simulation explicitly resolves mesoscale eddies in the KE and is forced with air-sea fluxes representing the years 1995–2007. A mean-eddy decomposition in a jet-following coordinate system removes the variability of the jet path from the eddy components of velocity; thus eddy kinetic energy in the jet reference frame is substantially lower than in geographic coordinates, and exhibits a cross-jet asymmetry that is consistent with the baroclinic instability criterion of the long-term mean field. The vorticity budget is computed in both geographic (i.e., Eulerian) and

jet reference frames; the jet frame budget reveals several patterns of eddy forcing that are largely attributed to varicose modes of variability. Eddies tend to diffuse the relative vorticity minima/maxima that flank the jet, removing momentum from the fast-moving jet core and reinforcing the quasi-permanent meridional meanders in the mean jet. A pattern associated with the vertical stretching of relative vorticity in eddies indicates a deceleration (acceleration) of the jet coincident with northward (southward) quasi-permanent meanders. Eddy relative vorticity advection outside of the eastward jet core is balanced mostly by vertical stretching of the mean flow, which through baroclinic adjustment helps to drive the flanking recirculation gyres. The jet frame vorticity budget presents a well-defined picture of eddy activity, illustrating along-jet variations in eddy-mean flow interaction that may have implications for the jet's dynamics and cross-frontal tracer fluxes.

2.1 Introduction

The western boundary current of the North Pacific separates from the coast of Japan as a fast, energetic narrow jet known as the Kuroshio Extension (KE). The KE jet path is variable and often highly meandering as it flows eastward, crossing ridges of relatively shallow bathymetry at approximately 140°E and 160°E (Figure 2.1). Part of this meandering pattern is quasi-stationary, with mean crests in the jet path around 143–144°E and 150°E and a trough near 146°E; this pattern is attributed to lee waves downstream of the Izu-Ogasawara Ridge (Mizuno and White, 1983). The jet is flanked by recirculation gyres to the south (e.g., Niiler et al., 2003) and north (Qiu et al., 2008; Jayne et al., 2009), though the subsurface northern gyres are weaker and generally linked to troughs in the quasi-stationary meanders (Jayne et al., 2009;

Tracey et al., 2012).

The KE is also associated with the highest levels of mesoscale eddy activity in the North Pacific (Qiu and Chen, 2010). In energetic western boundary current extensions, mesoscale eddies are thought to play an important role in cross-jet transport of tracers such as heat (e.g., Wunsch, 1999; Qiu and Chen, 2005a; Bishop et al., 2013) and momentum (e.g., Hall, 1991; Adamec, 1998; Greatbatch et al., 2010; Waterman et al., 2011). Mesoscale eddy activity in the KE region is complex, and takes a variety of forms. Meanders in the KE jet are steepened, likely from baroclinic instability (as shown by Shay et al., 1995, in the Gulf Stream) driven by vertical coupling between the surface meanders and deep pressure/current anomalies (Bishop and Bryan, 2013). These meanders then frequently pinch off the jet as rings that essentially extend to the bottom of the water column. Moreover, deep topographically-controlled eddies (whether generated from the downstream jet or elsewhere) propagate generally southwestward along f/H contours, with length scales (half-wavelengths) of 175-350 km and periods of 30-60 days (Greene et al., 2012). These eddies may produce changes in the path and cross-frontal structure of the KE jet (Tracey et al., 2012; Greene et al., 2012), and drive large divergent heat fluxes across the jet (Bishop, 2013). Smaller perturbations (with approximately 100-200 km length scales and 4-60 day periods) in the KE jet, often called frontal waves, propagate downstream along the jet and may interact with the topographically-controlled eddies to amplify or damp their influence, depending on their relative phasing (Tracey et al., 2012).

Due to the highly variable path of the KE jet, time averages of velocity and state variables in the KE region often smooth or obscure the true cross-jet structure; this problem has been successfully dealt with in the KE by transforming these fields

into a stream-coordinate reference frame relative to the jet (e.g., Howe et al., 2009; Waterman et al., 2011). Waterman et al. (2011) used this approach to estimate the eddy-mean flow interaction from observations, suggesting that eddies were helping to drive the mean jet and recirculations near the eddy kinetic energy (EKE) maximum at 146°E. However, in-situ observations of eddy momentum fluxes have generally been limited to either a small number of transects or an array spanning 5°-6° longitude (i.e., the KESS array, Donohue et al., 2008), and are also constrained to time periods ranging from synoptic snapshots (Howe et al., 2009) to sporadic two year field campaigns (Waterman et al., 2011).

The extension of spatial and temporal coverage offered by ocean general circulation models (OGCMs) provides an opportunity to study the along-jet and cross-jet variations in eddy forcing. Eddy forcing likely varies with longitude along the KE jet axis, influenced by bathymetric ridges underlying the jet (Figure 2.1) as well as position relative to the maximum in EKE at 146°E. Quasi-geostrophic models of idealized western boundary current extensions (e.g., Jayne et al., 1996; Waterman and Jayne, 2011; Waterman and Hoskins, 2013) in particular suggest that the sign of eddy forcing may vary in the along-jet direction near the eastward jet's EKE maximum. Previous studies using OGCMs (Qiu et al., 2008; Taguchi et al., 2010) have considered the effect of eddy PV fluxes on the KE northern recirculation gyre at a mid-depth level ($\sim$27.6σ_θ). Qiu et al. (2008) determined that the eddy PV flux convergence largely reinforces the mean circulation at mid-depths, helping to drive the northern recirculation gyre. Additional insights can be gained from an OGCM regarding the long-term mean effects of eddy forcing in the near-surface ocean.

In this study we examine how transient mesoscale eddies redistribute vorticity

along the near-surface KE jet. The central objective of this work is to clarify the long-term effect of eddies on jet velocities and cross-frontal gradients, as well as on the recirculation gyres flanking the jet. An eddying ocean simulation, run using the Parallel Ocean Program (POP), with 13 years of simulated KE variability is used to construct a vorticity budget in the vicinity of the narrow jet. In particular, our analysis employs a jet reference frame to preserve the jet's sharp gradients and so clarify the forcing from eddy vorticity fluxes on the mean jet, and how this forcing varies with longitude as well as across the jet. The paper is organized as follows: Section 2 describes the multi-year ocean model simulation. Section 3 details the stream-coordinate or jet reference frame used in our analysis, with a comparison of the jet characteristics and eddy activity as viewed in geographic (i.e., Eulerian) and jet-following reference frames. Section 4 considers the depth-averaged vorticity budget in geographic and jet reference frame, isolating the eddy terms and detailing their contribution to the budget. Section 5 discusses patterns of eddy forcing that are identified from the jet frame vorticity budget results. In Section 6 a brief study of the long-term mean baroclinic instability criteria is presented to offer some context for the results of the jet frame analyses; Section 7 offers a short summary of our findings and some conclusions.

2.2 Model description

The Parallel Ocean Program (POP) is an ocean general circulation model that solves the three-dimensional primitive equations for ocean dynamics (Smith and Gent, 2002; Smith et al., 2010). The model was run in the global domain, with nominal 0.1° horizontal resolution (∼8 km in the Kuroshio Extension region) on a

tripole grid, with two northern poles in Canada and Russia. The grid was configured with 42 vertical levels and ∼10 m vertical spacing near the surface, and utilizes the K-profile parameterization (KPP; Large et al., 1994) scheme for finescale (∼10 m) vertical mixing. Biharmonic viscosity and diffusivity are used, with equatorial values of $\nu_0 = -9 \times 10^9\,\mathrm{m^4\,s^{-1}}$ and $\kappa_0 = -3 \times 10^9\,\mathrm{m^4\,s^{-1}}$ that decrease as a function of the grid spacing cubed at higher latitudes so that the viscous term can balance the nonlinear advection terms (Maltrud et al., 1998). Modest surface salinity restoring was incorporated to limit drift, as were partial bottom cells to improve the representation of flow over bottom topography—important for representing the interactions with the ridges that underlie the KE.

The model run was initialized from Year 30 of an existing POP run that was configured on the same tripole grid (for more details see Maltrud et al., 2010), forced with Coordinated Ocean Research Experiments (CORE) normal-year surface fluxes representing a repeating annual cycle in the atmosphere (Large and Yeager, 2004), with added synoptic-scale variability averaged to monthly intervals. Our model run was then forced with the CORE 2 surface fluxes representing synoptically- and interannually-varying atmospheric conditions during the years 1990-2007 (Large and Yeager, 2009). Daily-mean state variables, surface fluxes, and advective fluxes were archived from 1995–2007 (post-adjustment to high-frequency atmospheric forcing) for most of the North Pacific, including horizontal fluxes of momentum Uu, Uv, Vu, Vv. The effective flux velocities U and V are weighted (six-point) horizontal averages of u and v respectively, defined such that both momentum and kinetic energy are conserved by advection on an Arakawa B-grid (for details of the calculation see Smith and Gent, 2002; Smith et al., 2010). The archived horizontal momentum fluxes are

particularly useful for quantifying the role of higher frequency mesoscale variability in the vorticity balance throughout the KE region.

2.3 The jet reference frame

2.3.1 Defining a jet reference frame

Daily averages of the KE flow (e.g., Figure 2.2a-b) typically depict much sharper sea surface height (SSH) gradients across the jet than are evident from geographic means over longer time periods (Figure 2.2c-d). This discrepancy results from large short-period fluctuations in the KE jet path (e.g., Fig. 2 in Qiu and Chen, 2010), associated with propagating eddies and frontal waves. Consequently, the path of the jet varies meridionally by over 300 km in some areas (Figure 2.1)—much more than the typical KE jet width of 100-200 km (Figure 2.2a-b; Fig. 7 of Waterman et al., 2011).

A more useful method of averaging KE jet features over long time periods (e.g., Bingham, 1992; Waterman et al., 2011) is to transform data into a jet reference frame. Bingham (1992) used a jet-following coordinate frame with two horizontal dimensions: the x-coordinate was the longitude of the nearest point on the jet axis and the y-coordinate was the distance from the jet axis. Our approach differs slightly in that we retain the longitude of the data point itself as the x-coordinate, so that the effects of bathymetry are as faithfully represented in long-term means as possible. Fields in the POP model are averaged in bins that correspond to the longitude of the grid points, and their distance to the closest point on the jet axis.

To transform into the jet reference frame, it is first necessary to come up with

a consistent objective method for identifying the jet axis (the zero y-coordinate in the jet reference frame). For the upper ocean, a fixed contour of SSH or temperature (Jayne et al., 2009; Waterman et al., 2011) or identified maxima in velocity magnitude (Howe et al., 2009) may be used to define the jet axis. Other criteria used to define the jet axis may be based on velocity shear (as described in Meinen and Luther, 2003) or gradients of SSH, temperature, or other properties that vary across the front. To define a jet path that follows the along-stream direction of the flow as closely as possible, we considered jet definitions using fixed contours of SSH (50 cm; Jayne et al., 2009) and temperature (12°C at 350 m depth; Waterman et al., 2011). In addition, we implemented a "steepest (SSH/temperature) gradient" method that identifies the SSH or temperature contours at each time interval co-located with the steepest gradients of SSH and 350 m temperature in a geographic range (30°–40°N, 140°–160°E) that corresponds to the KE (Figure 2.1). Of all these methods, the SSH steepest gradient method most consistently tracked the maximum velocity jet core in POP during the 13-year study period; hence our study employs this technique as described below.

To define the jet axis for each time period that will serve as the zero-coordinate in the cross-jet direction, SSH from the model output was first averaged in 5-day periods. The 5-day time average was chosen to minimize the rapid oscillations of the jet path that can occur as closed SSH contours (representing rings) pinch off from or reattach to the jet axis contour, while still averaging at a short enough timescale to follow the variations in the jet path due to most mesoscale features.

Next, the value of the jet axis SSH contour was computed for each 5-day period. Zonal and meridional derivatives of the 5-day mean SSH were computed in the model native grid, with the SSH interpolated before the derivatives were taken

so that the zonal and meridional derivatives were computed on the same grid as the SSH values they are derived from. From the zonal and meridional SSH derivatives, the magnitude of the SSH gradient $|\nabla(\mathrm{SSH})|$ was obtained. Then the top 5% of $|\nabla(\mathrm{SSH})|$ values were binned according to the values of SSH at the same locations, creating a probability distribution function (PDF). A Gaussian smoothing function was applied to the PDF to reduce the sensitivity of the maximum in the function to isolated peaks (such as might be associated with rings), and sampling biases that might result from the position of SSH contours relative to the model grid. The value of SSH associated with the maximum in the Gaussian-smoothed PDF was the SSH contour that defined the jet axis for that 5-day period. This method allows the contour to vary with seasonal and interannual changes in steric height, rather than using the same SSH contour to represent the jet axis at all time periods.

As a final filter, the length of the jet axis SSH contour was computed for each 5-day time period; in our case this was done for a larger domain, 135°E–170°E, to allow for some continuity of the defined jet axis with regions just outside of the study domain 140°–160°E. The SSH contours that had a length below a certain threshold (80% of the zonal distance between 135°E to 170°E) were considered unreliable, as these contours likely encompass rings rather than the true KE jet axis; this can occur during instances when a large ring has gradients around its edge that are nearly uniformly as steep or steeper than those at the true KE jet axis. In our analysis the unreliable SSH contours constituted about 5% of all the jet axis contours, and the 5-day time periods corresponding to them were not included in the final averages. The remaining viable jet axes (which account for 95% of 5-day periods from the 1995-2007 model output) were used in our jet frame analyses.

2.3.2 Jet reference frame binning and time averaging

Once the jet axes have been defined for each 5-day time period, the model grid points at each time period can be assigned a distance from the nearest point on the jet axis d, and a local jet orientation angle θ that is important for averaging vector quantities in the jet frame (for a more detailed description of how d and θ are computed see the Appendix part 2.9.1). The time average relative to the jet is computed by first binning the model grid points according to their longitude ϕ and values of d. Given a scalar quantity A, the angle bracket notation $\langle A \rangle$ indicates the set of values of A located at grid points in a given bin; for a bin centered at $\phi = \phi_m$ and $d = d_n$, the set $\langle A \rangle |_{(\phi_m, d_n)}$ includes model grid points in the ranges $\phi_m - \Delta\phi/2 \leq \phi < \phi_m + \Delta\phi/2$ and $d_n - \Delta d/2 \leq d < d_n + \Delta d/2$. The bin sizes $\Delta\phi = 0.1^\circ$ and $\Delta d = 10\,\mathrm{km}$ were chosen for the purposes of this study to correspond approximately to the spacing between model grid points. Once the values of A are sorted into bins, the jet frame time average of A in a given bin is the mean of all the points in that bin, denoted by $\overline{\langle A \rangle}^j$. To apply the jet frame time average to a vector quantity $\mathbf{u}$ the components of the vector aligned with the local jet frame axes $\mathbf{u}_j = (u_j, v_j)$ must first be computed, requiring a rotation of the vector by the orientation angle θ. This process is described in more detail in the Appendix part 2.9.2.

2.3.3 Jet characteristics in the geographic and jet reference frames

Time averages of jet properties such as SSH, currents, and pressure (Jayne et al., 2009; Waterman et al., 2011) are notably different when averaged in geographic and jet reference frames. The near-axis jet frame velocity maximum is more than twice

the magnitude of the geographic mean velocity maximum in observations (Waterman et al., 2011), with steeper velocity gradients evident on the flanks of the jet. Here we consider 0–250 m depth-averaged properties of the jet that have been time-averaged in geographic and jet reference frames. The upper 250 m of the water column encompasses the fastest velocities in the jet axis core as identified from observations (e.g., Howe et al., 2009; Waterman et al., 2011) and POP. Most of the eddy kinetic energy in the region of interest as depicted by POP also occurs in the upper 250 m. Figure 2.3 shows that the jet frame velocity variance terms at 146°E (the longitude of the observations discussed in Waterman et al., 2011) decay rapidly and fairly uniformly with depth, indicating that the 0–250 m layer is representative of the upper ocean; hence we use this layer in subsequent analyses.

As with observations, the cross-jet velocity profile in POP at 146°E is much sharper in the jet frame mean $\overline{\langle \mathbf{u}_j \rangle}^{j}$ than in the geographic mean $\overline{\mathbf{u}}$ (Figure 2.4; compare to Fig. 11a in Waterman et al., 2011). The jet reference frame clearly depicts the high surface velocities (> 1 m/s) that are nearly always present at the jet axis, but often obscured in long-term geographic means. All of the eastward flow in the main jet is confined to a band $\sim$200 km wide, with clearly defined (if much slower) westward recirculations on either side of the jet. Likewise, the sharp SSH gradients in the jet reference frame (Figure 2.2e-f) are generally contained within a band of $\sim$100 km, as opposed to the more diffuse gradients observed in geographic means (Fig. 2.2c-d). Both geographic and jet frame along-jet velocity peaks in POP are similar to or slightly stronger than in observations (Fig. 11a from Waterman et al., 2011).

A different view of the 0–250 m depth-averaged EKE field also emerges when eddy velocities are computed and averaged in the jet frame vs. the geographic frame

(Figure 2.5). The region of elevated geographic mean EKE $\overline{|\mathbf{u}|^2}$ as observed from altimetry (Fig. 2.5a) has a similar spatial extent as the elevated geographic EKE region computed from SSH gradients in POP (Fig. 2.5b), though the EKE magnitudes in POP are somewhat higher. The jet path and EKE from POP is similar to that of a high resolution (nominal 0.08°) HYCOM simulation (Fig. 2a from Kelly et al., 2007), with elevated EKE tracking the jet path and the crests and troughs of the jet path and stronger EKE signatures occurring at approximately the same longitudes. In POP the elevated geographic EKE region extends ∼200 km to either side of the mean position of the jet (Fig. 2.5b); its width is coincident with the variation in range of the jet axis itself. The jet frame EKE $\overline{\langle|\mathbf{u}_j|^2\rangle}^j$ (Fig. 2.5c) is of noticeably smaller magnitude, since the jet frame EKE near the jet axis reflects mostly the variance of the along-stream flow (Fig. 2.3), and excludes the part of geographic EKE due to time-varying jet meanders. The jet frame EKE also exhibits tightly-defined extremes near the jet axis; minima are found very close to the jet axis on its southern flank, at longitudes where the mean jet is flowing northward towards a quasi-permanent crest. This suggests that the structure of the south flank of the jet is remarkably stable in some areas, even with large shifts in the jet path's position and orientation. Maxima in jet frame EKE are found on the north flank of the jet opposite these minima, while separate maxima appear >150 km south and north of the jet, on the other side of the southern and northern recirculation gyres. Section 2.6 examines the possible effect of the mean jet structure on this cross-jet asymmetry in jet frame EKE.

2.4 The vorticity budget

Our formulation of the vorticity budget considers a layer of constant depth, with two fixed levels as upper and lower depth bounds. This form is most compatible with a z-level model; i.e., one that uses depth as its vertical coordinate. The depth-averaged terms of the budget can then be time-averaged either in the geographic or jet reference frame. We first consider the geographic time averages in Section 2.42.4.1, to identify any aspects of the KE jet's structure that can be readily understood in an Eulerian coordinate system, as well as to provide a comparison with the jet frame results. The jet frame averages are then computed and discussed in Sections 2.42.4.2 (full vorticity budget) and 2.42.4.3 (eddy forcing) respectively.

The forms of the primitive u- and v-momentum equations under hydrostatic and Boussinesq approximations that conserve kinetic energy when discretized in the POP model grid (Smith and Gent, 2002; Smith et al., 2010) are

$$\frac{\partial u}{\partial t} + (uu)_x + (vu)_y + (wu)_z - fv = -\frac{1}{\rho_0} p_x + F^x \tag{2.1}$$

$$\frac{\partial v}{\partial t} + (uv)_x + (vv)_y + (wv)_z + fu = -\frac{1}{\rho_0} p_y + F^y \tag{2.2}$$

respectively. F^x and F^y represent all of the effects of external body forcing (such as wind stress) and frictional dissipation. The main distinction between (2.1)-(2.2) and the continuous momentum equations is that in the model's discretized grid, momentum is fluxed from one grid cell to the next rather than advected along a fluid parcel trajectory. For example, in the case of u-momentum with the three-dimensional del operator ∇_3 and velocity vector $\mathbf{u}_3$, momentum advection is accomplished by $\nabla_3 \cdot (\mathbf{u}_3 u)$

rather than $\mathbf{u}_3 \cdot \nabla_3 u$. The terms in the momentum equations due to the curvature of the model grid (Smith and Gent, 2002; Smith et al., 2010) can be neglected, as the study region neither encompasses a large subset of the global grid nor approaches one of its poles.

The curl of (2.1) and (2.2) is the vorticity equation

$$\frac{\partial \zeta}{\partial t} + \nabla \cdot \mathbf{\Phi} + (wv)_{xz} - (wu)_{yz} + \beta v + f\left(u_x + v_y\right) = F \tag{2.3}$$

with the two-dimensional del operator $\nabla = (\partial/\partial x, \partial/\partial y)$, the horizontal flux vector of relative vorticity $\mathbf{\Phi} = \langle (uv)_x - (uu)_y, (vv)_x - (vu)_y \rangle$ and $F = \mathbf{k} \cdot \nabla \times (F^x, F^y)$ the external vorticity forcing and internal dissipation; F is not computed explicitly in our budget, but rather considered a residual. By adding and subtracting $(vw_z)_x - (uw_z)_y$ from the $\nabla \cdot \mathbf{\Phi}$ and $(wv)_{xz} - (wu)_{yz}$ terms respectively in (2.3) and invoking continuity, we obtain a form that more closely resembles a vorticity conservation equation

$$\frac{\partial \zeta}{\partial t} + \mathbf{u} \cdot \nabla \zeta - \zeta w_z + W + \beta v - f w_z = F \tag{2.4}$$

with the horizontal velocity vector $\mathbf{u} = (u, v)$, and $W = w\zeta_z + w_x v_z - w_y u_z$. The W term represents the sum of the vertical vorticity advection and twisting terms that result from taking the curl of vertical momentum advection. Correspondingly, the horizontal advection of relative vorticity $\mathbf{u} \cdot \nabla \zeta$ and stretching of relative vorticity $-\zeta w_z$ both result from taking the curl of horizontal momentum advection.

Equation (2.4) is then depth-averaged from $z = -h$ to $z = 0$, with $h = 250$ m in the open ocean to be consistent with the analysis of jet velocity profiles and EKE (Section 2.3b). In a grid cell that has (or is adjacent to) bathymetry less than

250 m deep, h is instead the depth of the shallowest bathymetry in that cell or any adjacent cell. By not including depths that are laterally adjacent to land, the vorticity equation excludes areas where the curl of the pressure gradient in the discrete model grid is nonzero (Appendix C.2 in Yeager, 2013), and retains stretching terms near sloping bathymetry that would otherwise be effectively negated by the boundary condition $w = 0$. Hence the vorticity equation (2.4) takes the same form over shallower bathymetry as it does in areas with bathymetry deeper than 250 m (see Bell, 1999, for further discussion of this method and how it relates to other forms of the vorticity balance) for further discussion of this method and how it relates to other forms of the vorticity balance.

2.4.1 Geographic vorticity budget and eddy forcing

In order to provide a context for eddy forcing in the jet reference frame, we first consider the vorticity budget in the more commonly-used geographic reference frame. This budget is just the geographic time average of (2.4), i.e., the time mean of each of the vorticity equation terms at a fixed longitude and latitude. The geographic time average is denoted with an overbar (e.g., the time average of a term A is denoted as $\overline{A}$).

$$\overline{\frac{\partial \zeta}{\partial t} + \mathbf{u} \cdot \nabla \zeta - \zeta w_z + W + \beta v - f w_z} = \overline{F} \tag{2.5}$$

Figure 2.6 shows the geographic 1995–2007 time mean of the terms in (2.5) from POP. The tendency term $\overline{\partial \zeta / \partial t}$ (Fig. 2.6a) is negligible, as expected for a long-term (in this case, multi-year) time average. Away from the near-coastal shallow bathymetry, the dominant balance in the upper 250 m is $\overline{\mathbf{u} \cdot \nabla \zeta} \sim -\overline{\beta v} + \overline{f w_z}$, with relative vorticity advection compensated for by vertical stretching of planetary vorticity and

(to a lesser extent) planetary vorticity advection. The three-way balance is indicative of standing baroclinic lee waves generated by the underlying bathymetry (Mizuno and White, 1983), particularly the ridge at ∼140°E. Near where the jet crosses 140°E, the vertical stretching term $\overline{fw_z}$ actually has a slightly larger magnitude than the relative vorticity advection term $\overline{\mathbf{u} \cdot \nabla\zeta}$, further implicating a localized bathymetric forcing. Moreover, the sign changes in all three terms along the jet correspond to the locations of quasi-permanent crests and troughs in the KE jet (Fig. 2.6b,e,f).

The remaining terms appear to be negligible away from the coast, including the relative vorticity stretching $-\overline{\zeta w_z}$ (Fig. 2.6c), vertical vorticity advection and twisting $\overline{W}$ (Fig. 2.6d), and even the residual $\overline{F}$ (Fig. 2.6g). The fact that the residual $\overline{F}$, which encompasses wind stress and internal frictional forcing, is not of leading-order importance suggests that the Kuroshio Extension is largely an inertial jet, even as the gyre that drives it is ultimately wind-forced.

To quantify the effect of eddy vorticity forcing on the mean flow in the geographic reference frame, the standard (Reynolds) decomposition of velocity into a time-mean and time-variable or eddy component is applied.

$$\mathbf{u} = \overline{\mathbf{u}} + \mathbf{u}' \tag{2.6}$$

The eddy terms that arise from (2.5) can then be expressed on the right-hand side of the vorticity equation as a forcing on the mean flow terms. We neglect the eddy terms arising from W, since the total W (Fig. 2.6d) is negligible.

$$\overline{\mathbf{u}} \cdot \nabla\overline{\zeta} - \overline{\zeta}\,\overline{w_z} + \beta\overline{v} - f\overline{w_z} = -\overline{\mathbf{u}' \cdot \nabla\zeta'} + \overline{\zeta' w_z'} + \overline{F} \tag{2.7}$$

The sum of the two eddy forcing terms on the right-hand side of (2.7) is the eddy relative vorticity flux convergence, i.e. $-\overline{\mathbf{u}' \cdot \nabla\zeta'} + \overline{\zeta' w_z{}'} = -\overline{\nabla \cdot (\mathbf{u}'\zeta')}$. The eddy vorticity forcing in the geographic reference frame (Figure 2.7) appears to be noisy, dominated by maxima/minima at scales of 1°-2°. Note that the eddy forcing from the $\overline{\zeta' w_z{}'}$ term is essentially nonexistent away from the coast in the geographic frame (Fig. 2.7b). However as we will show below, the corresponding eddy forcing term in the jet reference frame is non-negligible.

2.4.2 Vorticity budget in the jet reference frame

Now we again consider the terms of the vorticity budget, but averaged in the jet reference frame. Performing this calculation within a curved, moving coordinate system would require numerous additional (error-prone) terms to close the budget; we sidestep this issue by computing each individual term in the budget in the native model grid (geographic frame), and then binning and averaging in the jet frame only at the end. Hence, the form of the jet frame vorticity budget that we consider first is simply the jet frame time average applied to the vorticity equation (2.4).

$$\overline{\left\langle \frac{\partial\zeta}{\partial t} \right\rangle + \langle \mathbf{u} \cdot \nabla\zeta \rangle - \langle \zeta w_z \rangle + \langle W \rangle + \langle \beta v \rangle - \langle f w_z \rangle}^{j} = \overline{\langle F \rangle}^{j} \tag{2.8}$$

Figure 2.8 illustrates the terms in the 1995–2007 jet frame mean of the vorticity equation (2.8), for all bins within the ranges 140°E $\leq \phi \leq$ 160°E and $-250\,\text{km} \leq d \leq 250\,\text{km}$. In the jet frame, $\overline{\langle \partial\zeta/\partial t \rangle}^{j}$ may be non-negligible if the local ζ tendency is correlated with shifts in the jet position. However, this is not the case in the KE jet, where the jet frame time-mean $\overline{\langle \partial\zeta/\partial t \rangle}^{j}$ (Fig. 2.8a) is still negligible.

As in the geographic frame, the jet frame time-mean vorticity budget indicates a three-way dominant balance in which $\overline{\langle \mathbf{u} \cdot \nabla \zeta \rangle}^j$ is compensated by $\overline{\langle \beta v \rangle}^j$ and $-\overline{\langle f w_z \rangle}^j$, representative of standing lee waves. Hence both geographic and jet frame vorticity budgets demonstrate that the bathymetry-induced lee waves are associated with substantial vertical displacements related to the baroclinic structure of these waves. However, the maxima and minima of these terms are of higher magnitude and are spatially more constrained in the jet frame budget than in the geographic budget.

Outside the jet core (approximately 100-200 km from the jet axis) there is a cross-jet asymmetry in the relative vorticity advection (Fig. 2.8b) and vertical stretching (Fig. 2.8f) terms that is not readily apparent in the geographic budget (Fig. 2.6b,f). In these areas on either side of the core jet, the vertical stretching term suggests downwelling south of the jet and upwelling north of the jet. We also note that in the jet frame budget, the $-\overline{\langle \zeta w_z \rangle}^j$ and $\overline{\langle F \rangle}^j$ terms are no longer negligible near the jet axis (Fig. 2.8c,g), albeit still smaller in magnitude than the three dominant terms. The jet frame residual $\overline{\langle F \rangle}^j$ (Fig. 2.8g), which encompasses wind stress and frictional forcing and was negligible in the geographic reference frame, has a spatial distribution largely consistent with a biharmonic dissipation of ζ maxima and minima on the flanks of the high-velocity jet core.

2.4.3 Eddy forcing in the jet reference frame

We now expand the jet frame vorticity budget discussed in Section 2.42.4.2 to isolate the contribution from transient eddies. Neglecting $\partial\zeta/\partial t$ and W, which were shown to be negligible in the jet frame time-mean vorticity budget (Figure 2.8a,d), we apply a jet frame mean-eddy decomposition. When using the jet frame decomposition,

computations in the jet frame can no longer be limited to binning and averaging at the end, as was the case with (2.8). Rather, it is necessary to compute a jet frame mean velocity, and project the mean velocity field back onto the model grid at each time. The jet frame eddy velocity at each model grid point and time can then be defined as the difference between the total velocity and the jet frame mean velocity for the (ϕ, d) bin associated with that grid point and time.

$$\mathbf{u}'|_{(\phi,\Theta,t)} \equiv \mathbf{u}|_{(\phi,\Theta,t)} - \overline{\langle \mathbf{u} \rangle}^{j}|_{(\phi,d)} \tag{2.9}$$

The jet frame mean velocity $\overline{\langle \mathbf{u} \rangle}^{j}$, projected onto the axes of the model grid, is computed using a binning and averaging process analogous to the jet frame time averaging for scalar quantities, but rotations are also necessary to average the along-stream and cross-stream components of the vector (see Appendix part 2.9.2 for a more detailed description). Substituting the decomposition into the jet frame-averaged vorticity budget (2.8) yields

$$\overline{\left\langle \overline{\langle \mathbf{u} \rangle}^{j} \cdot \nabla \overline{\zeta}^{j} \right\rangle - \left\langle \overline{\zeta}^{j} \overline{w_z}^{j} \right\rangle + \langle \beta v \rangle - \langle f w_z \rangle + \left\langle (\mathbf{u} \cdot \nabla \zeta)' \right\rangle - \left\langle (\zeta w_z)' \right\rangle}^{j} = \overline{\langle F \rangle}^{j} \tag{2.10}$$

with $\overline{\zeta}^{j} \equiv (\overline{\langle v \rangle}^{j})_x - (\overline{\langle u \rangle}^{j})_y$, $\overline{w_z}^{j} \equiv -(\overline{\langle u \rangle}^{j})_x - (\overline{\langle v \rangle}^{j})_y$ and the eddy terms given by

$$(\mathbf{u} \cdot \nabla \zeta)' = \mathbf{u} \cdot \nabla \zeta - \overline{\langle \mathbf{u} \rangle}^{j} \cdot \nabla \overline{\zeta}^{j} \tag{2.11}$$

$$(\zeta w_z)' = \zeta w_z - \overline{\zeta}^{j} \overline{w_z}^{j} \tag{2.12}$$

All spatial derivatives, including those contained in the gradient operator ∇, are calculated in the (Eulerian) native model grid; this precludes the need to introduce additional terms into the vorticity budget that are a function of the motion, orientation, or curvature of the reference frame. It is important to note that in the jet frame, spatial derivatives do not commute with the time averages, i.e., $(\overline{\langle u \rangle}^j)_x \neq \overline{\langle u_x \rangle}^j$. Thus $(\mathbf{u} \cdot \nabla\zeta)' \neq \mathbf{u}' \cdot \nabla\left(\zeta - \overline{\zeta}^j\right)$ and $(\zeta w_z)' \neq \left(\zeta - \overline{\zeta}^j\right) \cdot \left(w_z - \overline{w_z}^j\right)$.

As in the geographic case, the eddy terms in (2.10) can be now be expressed as a forcing on the mean flow

$$\overline{\left\langle \overline{\langle \mathbf{u} \rangle}^j \cdot \nabla\overline{\zeta}^j \right\rangle - \left\langle \overline{\zeta}^j \overline{w_z}^j \right\rangle + \langle \beta v \rangle - \langle f w_z \rangle}^j = \overline{-\left\langle (\mathbf{u} \cdot \nabla\zeta)' \right\rangle + \left\langle (\zeta w_z)' \right\rangle + \langle F \rangle}^j \quad (2.13)$$

The eddy relative vorticity advection $\overline{-\left\langle (\mathbf{u} \cdot \nabla\zeta)' \right\rangle}^j$ and eddy vertical stretching of relative vorticity $\overline{\left[(\zeta w_z)'\right\rangle}^j$ on the right-hand side of (2.13) may now be considered as forcing terms on the mean flow. The sum of the two eddy forcing terms $\overline{-\left\langle (\mathbf{u} \cdot \nabla\zeta)' \right\rangle}^j + \overline{\left\langle (\zeta w_z)' \right\rangle}^j = -\overline{\left\langle (\nabla \cdot (\mathbf{u}\zeta))' \right\rangle}^j$ is the horizontal eddy vorticity flux convergence, which comprises the total eddy forcing considered in this study. The residual $\overline{\langle F \rangle}^j$ in (2.13) is the same as for the full jet frame vorticity budget in (2.8), with a forcing that acts to damp strong ζ maxima/minima in the jet (Figure 2.8g).

As in the geographic case, the jet frame eddy forcing terms in (2.13) computed along the KE jet (Figure 2.9) exhibit small-scale noise, particularly within 50 km of the jet axis. Nonetheless, the jet frame eddy forcing distribution can be much more readily associated with plausible dynamical mechanisms than the geographic eddy forcing. To aid the interpretation of the eddy forcing, we compare the total eddy forcing with the vorticity budget terms that represent the mean flow (Figure 2.10). A qualitative comparison of the patterns in Fig. 2.10 is supplemented with spatial

correlations and projections of the mean terms onto the total eddy forcing (Table 2.1), as a first-order attempt to quantify how much of the mean circulation (as indicated by vorticity) is eddy-driven. The correlations and projections in Table 2.1 are computed separately for the high-velocity jet core and for the regions outside the jet core, as the vorticity balances in these areas are quite different. In the high-velocity jet core, the eddy forcing is most highly correlated with the mean relative vorticity advection $\overline{\left\langle \overline{\langle \mathbf{u} \rangle}^j \cdot \nabla \overline{\zeta}^j \right\rangle}^j$ and mean vertical stretching $-\overline{\langle f w_z \rangle}^j$ terms, while outside the jet core only the mean vertical stretching term $-\overline{\langle f w_z \rangle}^j$ is robustly correlated with the forcing. The projections similarly indicate that these two mean circulation terms account for most of the flow's adjustment to the influence of eddies. The spatial variations in eddy forcing and their implications for the mean circulation of the KE jet and its recirculation gyres are discussed further in Section 2.5.

2.5 Eddy forcing patterns

The eddy forcing of the mean flow in the jet reference frame (Fig. 2.9, 2.10) may be largely explained as the superposition of four patterns, represented schematically in Figure 2.11. The first three of these patterns only act within the KE jet itself, and are mainly balanced by the mean $\overline{\left\langle \overline{\langle \mathbf{u} \rangle}^j \cdot \nabla \overline{\zeta}^j \right\rangle}^j$ relative vorticity advection and $-\overline{\langle f w_z \rangle}^j$ vertical stretching terms (Figure 2.10, Table 2.1). The fourth pattern predominates on either side of the jet where the recirculation gyres are present, and is primarily balanced by the $-\overline{\langle f w_z \rangle}^j$ vertical stretching term.

Focusing first on the eddy horizontal advection forcing term $\overline{-\left\langle (\mathbf{u} \cdot \nabla \zeta)' \right\rangle}^j$ (Fig. 2.9a), a superposition of two patterns is apparent. Pattern 1 (Fig. 2.11a) is generally positive vorticity forcing to the south, and negative vorticity forcing to the

north. This corresponds to a downgradient vorticity flux across the jet, such that the eddies are acting to reduce the cross-jet vorticity contrast and decelerate the jet. Such behavior is characteristic of developing instabilities along a barotropic jet (Waterman and Jayne, 2011; Waterman and Hoskins, 2013). Pattern 2 (Fig. 2.11b), again originating from the $\overline{-\left\langle (\mathbf{u}\cdot\nabla\zeta)'\right\rangle}^{j}$ term, is a tendency of the vorticity forcing to be more positive in northward-flowing parts of the mean jet (e.g., 140°–143°E) and negative in southward-flowing parts of the mean jet (e.g., 144°–146°E). Pattern 2 is compensated for by both $-\overline{\langle fw_z\rangle}^{j}$ and $\overline{\langle \beta v\rangle}^{j}$ (Fig. 2.10c,d) in the mean flow, suggesting that eddies play a role in reinforcing the stretching and meridional motions associated with the quasi-permanent meanders in the jet; this result is consistent with estimates of eddy forcing derived from satellite observations (Qiu and Chen, 2010).

Pattern 3 (Fig. 2.11c) originates from the $\overline{\left\langle (\zeta w_z)'\right\rangle}^{j}$ term (Fig. 2.9b), and consists of both cross-jet and along-jet variations in vorticity forcing. Approximately where the mean jet is flowing northward, the vorticity forcing is positive south of and negative north of the jet axis, reinforcing Pattern 1 and the associated downgradient fluxes (corresponding to jet deceleration). Where the mean jet is flowing southward, however, the vorticity forcing pattern is the opposite—negative to the south and positive to the north of the jet. This pattern indicates upgradient vorticity fluxes, and an acceleration of the jet. Pattern 3's acceleration of the jet is partially canceled out by Pattern 1 in the $\overline{-\left\langle \overline{\langle\mathbf{u}\rangle}^{j}\cdot\nabla\bar{\zeta}^{j}\right\rangle}^{j}$ term (Fig. 2.10a), but in some areas its effect persists (e.g., at ∼144°E).

The effect of Pattern 3 may be further clarified by considering the change in along-jet velocity from west to east (Figure 2.12). A general deceleration of the jet occurs east of a maximum at 142°E, which reflects the influence of both eddy

forcing patterns 1 and 3 as well as frictional dissipation. However, at 144°–145°E and 150°–151°E the opposite occurs: a brief acceleration of the jet towards the east. Both of these locations are immediately downstream of crests in the long-term mean jet (Fig. 2.9d), and both coincide with the eddy acceleration from the $\overline{\left\langle (\zeta w_z)' \right\rangle}^j$ term (Fig. 2.9b). The acceleration of the jet at these locations thus appears to be closely related to vertical vortex stretching, likely from some combination of eddy motions and sharp curves (i.e., ζ anomalies) in the jet itself. The locations of these eddy-forced accelerations in the jet are approximately coincident with negative (upgradient) cross-stream eddy diffusivities in the upper ocean, as quantified using the same high-resolution configuration of the POP model (Chen et al., 2014). Moreover, studies in the Gulf Stream have observed near-surface cross-stream divergences (convergences) near the surface that are situated upstream (downstream) of a meander crest (Bower, 1989; Thomas and Joyce, 2010), consistent with the alternating deceleration and acceleration of the jet associated with Pattern 3. Bower and Rossby (1989) observed entrainment of fluid from outside the jet near crests but not near troughs, likewise suggesting an asymmetry in flow properties relating to the jet's meanders. Thomas and Joyce (2010) noted that the cross-stream convergence downstream of a jet crest is frontogenetic; the eddy forcing described in Pattern 3 suggests that mesoscale instabilities help support frontogenesis in these locations.

The along-jet transitions in eddy forcing represented in Pattern 3 also resemble in some aspects the downstream changes identified in idealized quasi-geostrophic (QG) studies of barotropic (e.g., Jayne et al., 1996; Waterman and Hoskins, 2013) and baroclinic (e.g., Holland and Rhines, 1980; Mizuta, 2009; Waterman and Jayne, 2011) zonal jets. In the idealized studies, eddies develop from unstable regions in the mean

flow, with downgradient eddy vorticity fluxes acting to decelerate the mean eastward jet. However, downstream of the unstable regions the QG jet stabilizes and resembles a wave radiator, with advected and radiating instabilities inducing net upgradient eddy vorticity fluxes (e.g., Holland and Rhines, 1980; Waterman and Jayne, 2011) that help to drive the mean eastward jet and its recirculation gyres. This would appear to offer an explanation for the along-jet variations in eddy acceleration of the jet, but does not explain why the eddy-induced eastward accelerations only appear in the $\overline{\left\langle (\zeta w_z)' \right\rangle}^j$ term. In the case of the barotropic jet, the only non-negligible eddy forcing term to decelerate/accelerate the mean jet is $\overline{-\left\langle \overline{\langle \mathbf{u} \rangle}^j \cdot \nabla \overline{\zeta}^j \right\rangle}^j$, but in this case it is the $\overline{\left\langle (\zeta w_z)' \right\rangle}^j$ stretching term that supplies the alternating deceleration and acceleration. Aside from this difference, our results show eddy-mean flow interactions similar to those in idealized QG zonal jets, with some additional complexity associated with the quasi-permanent meanders of the KE.

Pattern 4 (Fig. 2.11d) is the dominant eddy forcing more than 80 km from the jet axis, originating from the $\overline{-\left\langle \overline{\langle \mathbf{u} \rangle}^j \cdot \nabla \overline{\zeta}^j \right\rangle}^j$ term; it consists of negative forcing south of the jet, and positive forcing north of the jet. As this forcing is balanced mostly by $\overline{-\langle f w_z \rangle}^j$ (Figure 2.10, Table 2.1), the primary consequence of eddy vorticity forcing outside of the KE jet core is mean vertical stretching of the surface layer to the south of the jet and mean vertical compression to the north of the jet. The baroclinic adjustment to these changes could help maintain the pressure anomalies that drive the recirculation gyres—implying that eddies do indeed help drive the broader mean recirculations, even as the eddy forcing is mostly against the mean flow at the jet axis. The mean and eddy forcing terms also may be used to consider whether recirculation gyres are driven by the *mean* advection of PV anomalies from other latitudes, or by

eddy motions (for a more detailed discussion see Waterman and Jayne, 2011). If mean PV advection is the dominant mechanism, then the vertical stretching $\overline{-\langle fw_z \rangle}^j$ (Fig. 2.10d) north and south of the jet should be compensated by the mean relative vorticity advection $\overline{\left\langle \overline{\langle \mathbf{u} \rangle}^j \cdot \nabla \overline{\zeta}^j \right\rangle}^j$ (Fig. 2.10a). Partial compensation between these mean terms is shown in some areas south of the jet, particularly east of 150°E and between 144°-146°E (Fig. 2.10a,d). However, in other regions outside the jet core, mean vorticity advection does not seem capable of inducing vertical stretching of the correct sign; only the eddy forcing (Fig. 2.10e) acts consistently to stretch (compress) the upper layer south (north) of the jet core, supporting the hypothesis that the recirculations are largely eddy-driven (e.g., Jayne et al., 1996; Waterman and Jayne, 2011).

2.6 Jet instability characteristics

One possible mechanism for generating eddy activity and eddy forcing is a background state of the jet that is unstable to small perturbations. An extensive literature considers the growing and radiating modes of instability for barotropic (e.g., Kuo, 1949; Howard and Drazin, 1964; Talley, 1983a) and baroclinic (e.g., Talley, 1983b; Samelson and Pedlosky, 1990) instabilities. Here we note locations where the mean state of the jet allows for, but does not necessarily support, unstable modes. A necessary condition for baroclinic instability (Charney and Stern, 1962) is a change in sign of the Ertel potential vorticity (PV) gradient along isopycnals Q_y, in the cross-jet direction. For a zonal jet, Q_y is given by

$$Q_y \equiv -\frac{\rho}{(\rho_\theta)_z} \left\{ \frac{\partial Q_E}{\partial y} - \frac{\partial Q_E}{\partial z} \left[\frac{(\rho_\theta)_y}{(\rho_\theta)_z} \right] \right\} \tag{2.14}$$

where $Q_E \equiv -\frac{f+\zeta}{\rho}(\rho_\theta)_z$ is Ertel PV, ρ_θ is potential density, with the Coriolis parameter f and relative vorticity $\zeta = v_x - u_y$. The expanded form of Q_y is

$$Q_y = [\beta + \zeta_y] + (f+\zeta)\frac{(\rho_\theta)_{zy}}{(\rho_\theta)_z} + f\frac{(\rho_\theta)_{zz}(\rho_\theta)_y}{[(\rho_\theta)_z]^2} + \zeta_z\left[\frac{(\rho_\theta)_y}{(\rho_\theta)_z}\right] \tag{2.15}$$

with $\beta = \partial f/\partial y$ the planetary vorticity gradient. For a jet such as the KE which is generally non-zonal at a given location, the meridional y-derivatives in (2.14) and (2.15) are instead computed in the cross-jet direction. If ζ and its gradients are negligible, then this condition is equivalent to the baroclinic instability condition in Gill et al. (1974). If isopycnals are flat, i.e., $(\rho_\theta)_y = 0$, then (2.15) reduces to the barotropic instability condition that $\partial/\partial y\,(f+\zeta)$ must change sign in the cross-jet direction.

Transects (Figures 2.13a-c) of the jet at 142°E (northward mean jet, and longitude of regional jet frame EKE maximum in Fig. 2.5c), 145°E (southward mean jet), and 148°E (northward mean jet) illustrate a notable asymmetry of the KE jet's mean background state. While the PV gradient Q_y (Figures 2.13d-f) in the upper 100 m reverses on both flanks of the jet, only the gradient reversal on the north flank extends down to the thermocline and beyond. On the south flank of the jet, a strong positive gradient in Ertel PV at 100–500 m exists between the low-PV subtropical mode water south of the jet and the jet axis, consistent with observations of PV structure across the KE jet (Howe et al., 2009). The strong positive PV gradient stabilizes the southern flank of the jet—likely explaining the minima in jet frame EKE immediately south of the jet axis (Fig. 2.5c). Because of the stabilizing PV gradient in the isopycnal range $\rho_\theta = 1024.5 - 1026\,\mathrm{kg\,m^{-3}}$ (Figures 2.13d-f), the reversals in Q_y on the south flank of the jet are displaced further from the jet axis than on the north

flank, well outside the region of high velocity and high shear. This may be related to the jet frame EKE asymmetry (Fig. 2.5c), as much of the jet frame EKE is confined to the north flank of the jet.

As the jet flows eastward from 142°E (Fig. 2.13d) to 148°E (Fig. 2.13f), the zero crossing of Q_y on the north flank moves further from the high-velocity jet core and its associated shear. Thus a gradual lessening of the positive and negative Q_y gradients occurs north of the jet axis, consistent with the dampening magnitude of jet frame EKE maxima as the jet moves eastward. However, the most favorable conditions for baroclinic instability remain to the north of the jet in all transects, where the PV gradient reversal is still closer to the jet in the 100–500 m depth range. This does not explain why EKE is higher south of the jet at 145°E (Fig. 2.5c), though it must be noted that the synoptic stability characteristics of the jet vary with time, and episodic shifts in the jet's asymmetric structure might explain a shift in EKE structure. Yet the along-jet variation in jet-frame EKE (and eddy forcing; i.e., Patterns 2 and 3 discussed in Section 2.5) does not appear to result from along-jet changes in the baroclinic instability criterion, suggesting that the jet-frame EKE at 144–145°E may not be generated by the mean background state of the jet.

While the PV gradient is inconclusive regarding the along-jet variations in jet frame EKE, a comparison of the geographic vs. jet frame EKE provides more insight. The EKE maximum just south of the mean jet at 144°-145°E is particularly large in the geographic frame (Fig. 2.5b) compared to the jet frame (Fig. 2.5c), while the jet frame does not remove as much eddy variability from the EKE maximum at 142°-143°E. This suggests that the jet position has a more variable distribution at 144°-145°E. The jet frame EKE also has large, well-defined maxima approximately

200 km away from the jet in either direction, which suggests that 144°–146°E is a favored area for ring separation from the jet. Hence the displacement of the near-jet EKE maximum south of the jet at 144°–146°E (Fig. 2.5c) may be related to the complicated dynamics of the jet as rings separate from it.

2.7 Conclusions

In this study we computed a vorticity budget from the archived output of an ocean GCM using a jet-following reference frame, to elucidate eddy-mean interactions that might be partially or even fully obscured in geographic time averages. With this high-resolution model simulation, we show vorticity signatures consistent with some previously observed and explained phenomena in the KE jet: the quasi-permanent meanders which are essentially standing lee waves forced by bathymetry (White and McCreary, 1976; Mizuno and White, 1983), and the eddies playing a role in driving the time-mean recirculations (e.g., Jayne et al., 1996; Waterman and Jayne, 2011). In addition, the jet frame time mean illustrates a fundamental asymmetry of instability development in the KE. The EKE maxima in the jet frame (Fig. 2.5c) occur on the north side of the jet, opposite regions of nearly zero EKE on the south side. The asymmetry can be readily explained by baroclinic instability criteria in the jet derived from observations (Howe et al., 2009) as well as in our model (Fig. 2.13), yet this asymmetry is not at all obvious from long-term means of geographic EKE (Fig. 2.5a-b). The jet frame EKE asymmetry is also consistent with other GCM studies (Qiu et al., 2008; Taguchi et al., 2010) that indicate eddy dissipation processes are necessary to simulate a realistically weak northern recirculation gyre. Our budget also demonstrates eddy forcing behaviors near the KE jet axis that have previously

been suggested by idealized models of zonal jets or by observations, but have not been explicitly identified in GCMs. In particular, eddies were found to play a role in the acceleration of the high-velocity jet core just downstream of quasi-permanent crests in the jet, in contrast to the general decelerating trend of the jet towards the east (Fig. 2.11c, 2.12).

It is important to note that the patterns of eddy vorticity forcing identified in this study may not include all of the effects of mesoscale eddies on the vorticity structure of the jet. Rather, the primary focus of this study is on the role of eddies in the forward acceleration/deceleration of the jet, and the changes in the cross-jet gradient associated with these velocity changes. In the high-velocity jet core surrounding the jet axis, these effects can largely be described in terms of varicose modes of variability, which affect the jet's width and cross-jet structure. Fluctuations in the jet path, which correspond closely if not exactly to sinuous modes of variability, are regarded in the jet frame as part of the mean flow at weekly or longer timescales. (For more background on sinuous and varicose modes, a number of previous studies have considered their stability characteristics using analytical methods, e.g., Talley, 1983a,b; Pratt et al., 1991; Hogg, 1994). Thus the jet frame EKE and eddy forcing can be attributed mostly to varicose modes; the effects of sinuous modes are manifested in the mean circulation terms. Both sinuous and varicose modes may radiate instabilities away from the jet (Talley, 1983a,b), and the effects of sinuous modes may be quantified as eddy forcing outside the high-velocity jet core. Therefore, the jet-frame mean-eddy decomposition implemented in this study is most useful for considering the effects of time-variable motions associated with: (1) locally-growing barotropic and baroclinic instabilities that excite varicose modes of variability, as well as sinuous modes that

may radiate away from the jet, (2) frontal waves that propagate in the along-jet direction, which may involve varicose modes, and (3) entrant eddies that originate outside of the jet or leave the jet and then impinge on the jet again, such as deep topographically-controlled eddies (Tracey et al., 2012; Greene et al., 2012) whose structure is largely independent of the surface jet. Synoptic snapshots suggest that all three types of variability may contribute to the eddy forcing patterns we have identified in the Kuroshio Extension, though substantially more analysis would be needed to quantify the relative impact of each phenomenon on the 13-year averages of eddy forcing.

One limitation of using eddy vorticity forcing to understand eddy-mean flow interactions is that it is not always a straightforward task to infer the horizontal momentum forcing on the jet. For example, a gyre in near solid-body rotation has negligible relative vorticity gradients $\nabla\zeta \sim 0$, but can still experience nonlinear momentum advection from the wind or eddies spinning up the gyre. The effect of this forcing on the mean flow will appear in the vorticity budget (2.7) or (2.13) in the mean stretching terms $-fw_z$ and $-\zeta w_z$; baroclinic adjustment must then be assumed before this forcing has an effect on the horizontal velocity. This issue is of little consequence near the jet where relative vorticity is effectively the cross-jet gradient of along-jet velocity $\overline{\langle u \rangle}^j$, and momentum forcing can be directly inferred from vorticity forcing. Further away from the jet axis, however, the influence of the eddies on the recirculation gyres is only identified indirectly through the response of the $\overline{-\langle fw_z \rangle}^j$ term to eddy forcing. The residual-mean momentum equations (e.g., Andrews and McIntyre, 1976; Young, 2012) may be one solution to this problem, in which the eddy forcing is expressed directly in terms of Eliassen-Palm fluxes, and is balanced

by the acceleration of the mean velocity and a "residual" circulation. Applying this framework to a curved, time-variable jet reference frame also presents some challenges, but the ability to compare the acceleration of the mean jet to the eddy momentum forcing makes this an ideal subject for future work.

2.8 Acknowledgments

A. S. Delman (ASD) and J. L. McClean (JLM) were supported by NSF grant OCE-0850463 and Office of Science (BER), U. S. Department of Energy, grant DE-FG02-05ER64119. ASD and J. Sprintall were also supported by a NASA Earth and Space Science Fellowship (NESSF), grant NNX13AM93H. JLM was also supported by USDOE Office of Science grant entitled "Ultra-High Resolution Global Climate Simulation" via a Los Alamos National Laboratory subcontract. S. R. Jayne was supported by NSF grant OCE-0849808. Computational resources for the model run were provided by NSF resource grants TG-OCE110013 and TG-OCE130010. Output from this simulation is available through the Extreme Science and Engineering Discovery Environment (XSEDE). The authors would also like to acknowledge useful discussions with Larry Pratt and Paola Cessi during the course of this work, and the editor, two anonymous reviewers, and an associate editor whose suggestions greatly improved this manuscript.

Chapter 2, in full, is a reprint of the material as it appears in the Journal of Physical Oceanography, 2015, Delman, A. S., J. L. McClean, J. Sprintall, L. D. Talley, E. Yulaeva, and S. R. Jayne, copyright 2015 American Meteorological Society. I was the primary investigator and author of this manuscript; the co-authors supervised the preparation of the manuscript, and/or were responsible for running the model

simulation that was used in the analysis.

2.9 Appendix: A longitude-preserving jet reference frame

2.9.1 Jet frame coordinates for each grid point

In order to obtain time averages of a quantity in the jet reference frame, it is necessary to assign each point in the model grid a set of jet frame coordinates. Each grid point in the model already has a longitude ϕ and latitude Θ associated with it; thus neglecting the depth coordinate (which is not affected by the jet frame coordinate transformation) the data at each point in time t can be described as located at the geographic coordinates (ϕ, Θ, t). In the jet reference frame that is used in this study, the geographic coordinates of each model grid point are transformed into the jet frame

$$(\phi, \Theta, t) \rightarrow (\phi, d, t) \tag{2.16}$$

so only one of the three coordinate values changes; longitude and time are retained. The new coordinate d is the distance between the grid point and the nearest point on the jet axis. Positive values of d are on the "north" side of the jet axis, and negative values on the "south" side, with "north" ("south") defined as to the left (right) of the direction of jet flow. (When the jet is sufficiently meandering a point on the "north" side of the jet may actually be south of its nearest point on the jet axis, and vice versa.)

The value of d is computed for each point as follows: distances are first

computed between discrete points on the jet axis and the array of grid points in the domain. Each grid point then has a discrete point on the jet axis that is the closest to it. The calculation of the distance is refined further by computing the orientation angle θ of the line segments between each discrete jet axis point. The value of θ is then determined for each model grid point by interpolating the values of θ from the two line segments adjacent to the nearest jet axis point. Finally, the exact value of d for the point is computed from the distance between the point and the perpendicular distance to the closest of the two line segments (Figure 2.14). If the point that adjoins the two line segments (i.e., the original discrete jet axis point identified as closest) is closer than any other point on the two segments, then d is taken to be just the distance between the grid point and the original discrete jet axis point.

Note: for each model grid point and 5-day time period, the calculation just described yields a coordinate value d, but also an orientation angle θ. The orientation angle of each point is important in the calculation of vector mean quantities in the jet frame (e.g., velocities and fluxes), and therefore it is also necessary for the jet frame mean-eddy decomposition (Appendix part 2.9.2).

2.9.2 The jet frame mean-eddy decomposition

Binning and averaging scalar quantities in the jet reference frame allows for a more faithful representation of the jets synoptic structure in long-term time averages (e.g., Figure 2.2). However, in order to use the jet frame's advantages to quantify the contribution of eddies to the mean circulation, it is necessary to define jet frame means of vector quantities (namely, velocities). Then the eddy part of the circulation can be defined as the deviation of the flow field at each time coordinate (i.e., 5-day

time period) from the jet frame mean circulation.

Vector quantities that are binned and averaged in the jet frame must first be rotated by the local orientation angle θ so that the u axis is parallel to the jet orientation at the nearest point on the jet axis, i.e.,

$$\mathbf{u}_j \equiv \mathbf{R} * \mathbf{u} \tag{2.17}$$

where $\mathbf{u} = (u, v)$ and $\mathbf{R}$ is the rotation matrix

$$\mathbf{R} = \begin{bmatrix} \cos\theta & \sin\theta \\ -\sin\theta & \cos\theta \end{bmatrix} \tag{2.18}$$

The resulting along-stream and cross-stream components of velocity $\mathbf{u}_j = (u_j, v_j)$ are then binned and averaged in the jet frame, in the same way as scalar quantities are. This produces jet frame time means of along-stream and cross-stream velocity $\overline{\langle \mathbf{u}_j \rangle}^j = \left(\overline{\langle u_j \rangle}^j, \overline{\langle v_j \rangle}^j \right)$. In order to use these computed mean velocities to define the jet frame eddy velocity for each model grid point and 5-day time period, these mean velocities are then rotated back into the native model grid, using the inverse of the rotation matrix $\mathbf{R}^{-1}$ specific to that grid point and time

$$\overline{\langle \mathbf{u} \rangle}^j \equiv \mathbf{R}^{-1} * \overline{\langle \mathbf{u}_j \rangle}^j \tag{2.19}$$

and the jet frame eddy velocity is the difference between the jet frame mean in the Eulerian grid $\overline{\langle \mathbf{u} \rangle}^j$ and the total velocity, as defined in (2.9).

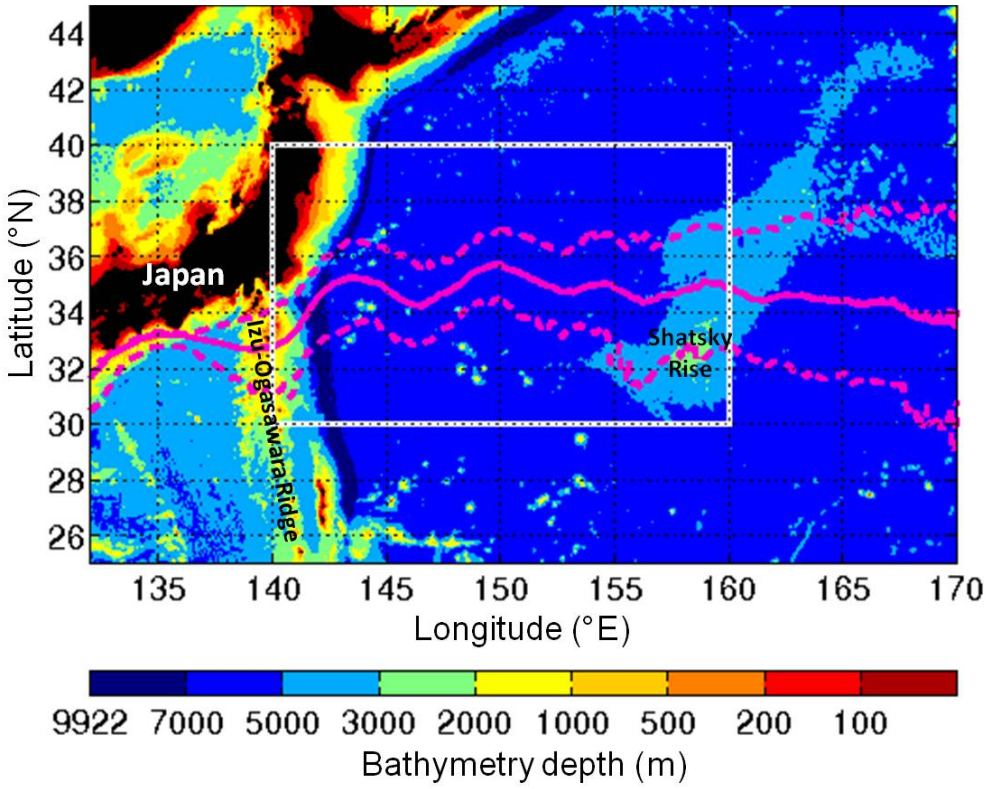

Figure 2.1: Bathymetry in the Kuroshio Extension region. The magenta lines indicate the mean (solid) and 10th/90th percentile (dashed) jet axis positions computed from POP for 1995–2007. The jet axis position for each 5-day period is defined as the 5-day mean SSH contour associated with the steepest gradients of SSH in the study region (white rectangle). The jet axis position is then extended outside the study region along the same SSH contour.

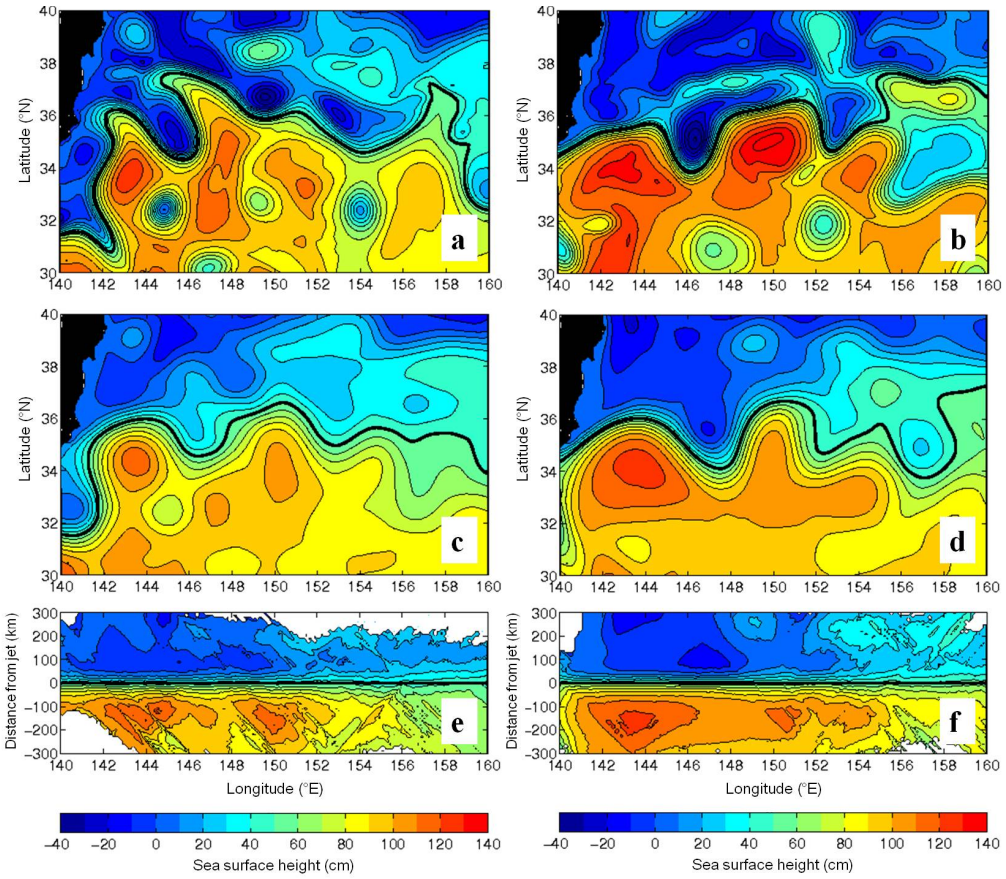

Figure 2.2: POP sea surface height (SSH) daily snapshots on (a) June 22, 1997 and (b) July 17, 1998, with the thick black line indicating the 50 cm contour. (c-d) POP SSH annual geographic means for 1997 and 1998 respectively, with the 50 cm contour indicated as in (a-b). (e-f) POP SSH annual jet frame means for 1997 and 1998 respectively, as computed using the steepest gradient SSH method; the thick black line indicates the jet axis. The color scale is the same for (a)-(f), and is indicated by the color bars below (e) and (f). The contour interval for all panels is 10 cm.

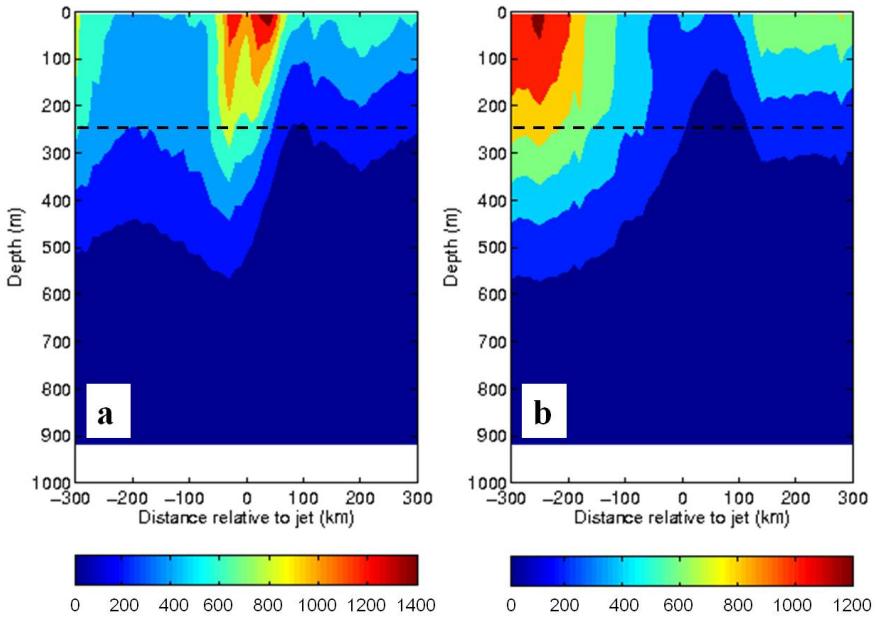

Figure 2.3: Eddy variance terms (a) $\overline{\langle u_j{}' u_j{}' \rangle}^j$ and (b) $\overline{\langle v_j{}' v_j{}' \rangle}^j$ in POP along 146°E, computed in the jet reference frame for 1995–2007. The dashed line indicates 250 m, the base of the upper layer used for depth-averaging in our analyses. The color scales are indicated below each figure, with units of $\mathrm{cm}^2\ \mathrm{s}^{-2}$. The contour interval for (a)-(b) is 200 $\mathrm{cm}^2\ \mathrm{s}^{-2}$.

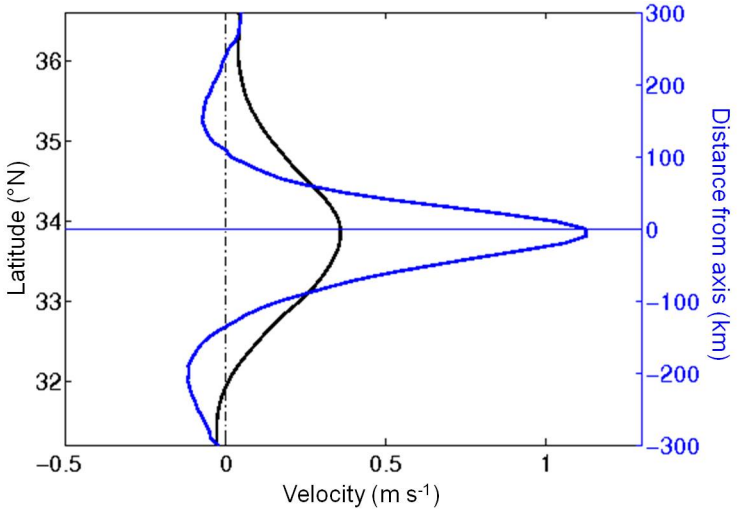

Figure 2.4: The 1995–2007 mean cross-jet velocity profile (0–250 m depth average) at 146°E in POP, as computed in the geographic (black) and jet (blue) reference frames. In the geographic reference frame eastward velocity $\overline{u}$ is plotted; in the jet reference frame along-jet velocity $\overline{\langle u_j \rangle}^j$ is plotted.

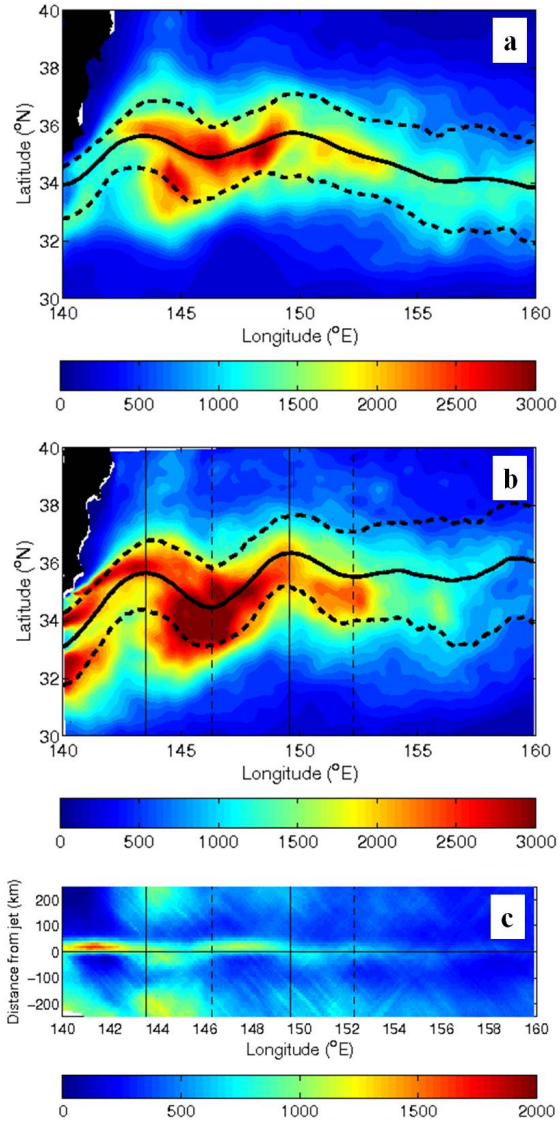

Figure 2.5: (a) 1995–2007 geographic mean geostrophic eddy kinetic energy (EKE) $\overline{|\mathbf{u}|^2}$, from altimetry-derived AVISO gridded ($\sim$1/3°) weekly maps of mean sea level anomaly. (b) 1995–2007 geographic mean surface EKE in POP, computed from sea surface height (SSH) anomalies as in (a). The thick black lines indicate the mean (solid) and 10th/90th percentile (dashed) jet axis positions computed from the altimeter (a) and POP (b) SSH gradients. (c) 1995–2007 jet frame mean, 0–250 m depth-averaged EKE $\overline{\langle |\mathbf{u}_j|^2 \rangle}^j$ in POP. The thin vertical lines in (b) and (c) denote the longitudes of crests (solid) and troughs (dashed) in the mean jet path. The color scales are indicated below each panel. The color scale for (c) is different from (a)-(b).

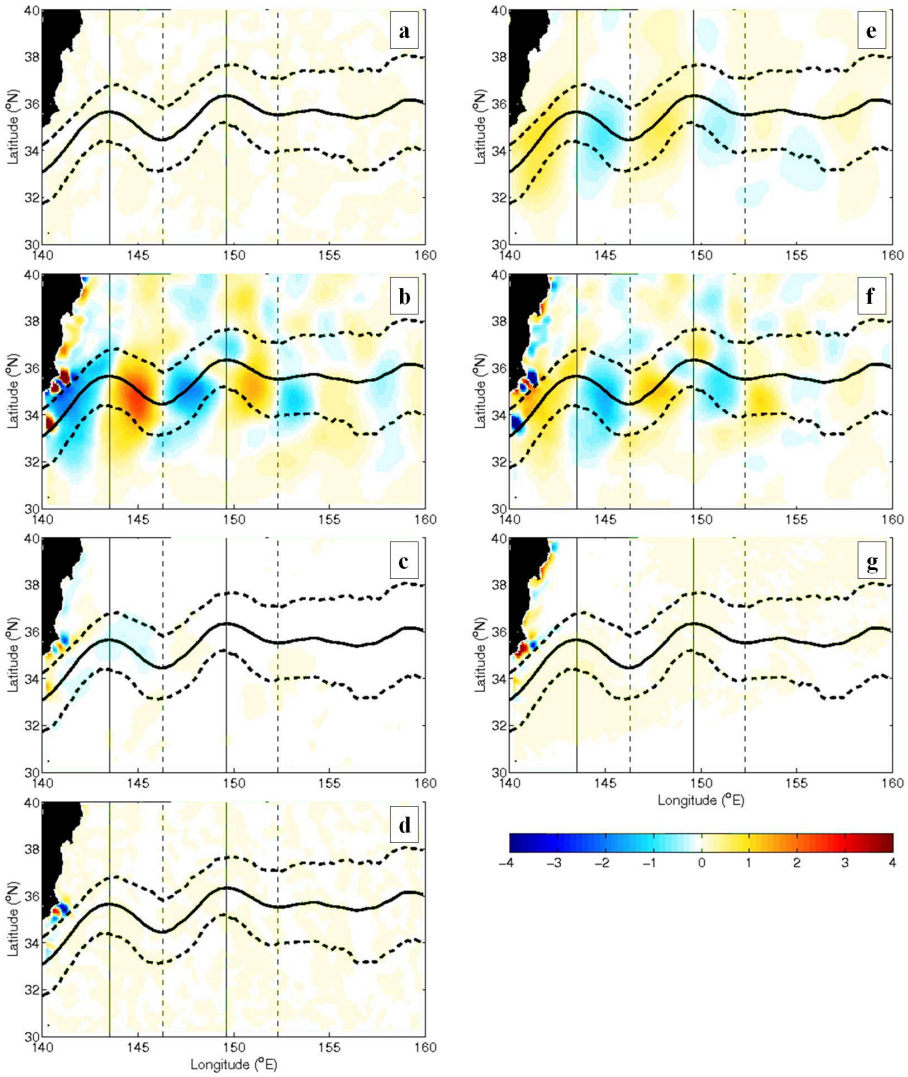

Figure 2.6: 1995–2007 geographic time mean of the terms in the full vorticity budget in equation (2.5), vertically averaged 0–250 m, from POP. The terms are the depth- and time-averaged (a) $\overline{\frac{\partial \zeta}{\partial t}}$, (b) $\overline{\mathbf{u} \cdot \nabla \zeta}$, (c) $\overline{-\zeta w_z}$, (d) $\overline{W}$, (e) $\overline{\beta v}$, (f) $\overline{-f w_z}$, and (g) $\overline{F}$, the residual. Each term has been smoothed post-averaging with a Gaussian filter (0.2° e-folding scale, 1° cutoff radius). The e-folding scale and cut-off radius were chosen to remove noise at the highest wavenumbers, while preserving forcing patterns that are evident in the jet at the spatial scales of eddies (1°–2°). Thick black lines indicate the mean (solid) and 10th/90th percentile (dashed) jet axis positions. The thin vertical lines denote the longitudes of crests (solid) and troughs (dashed) in the mean jet path. The color scale is indicated in the lower right corner and is the same for (a)-(g), with units of 10^{-11} s^{-2}.

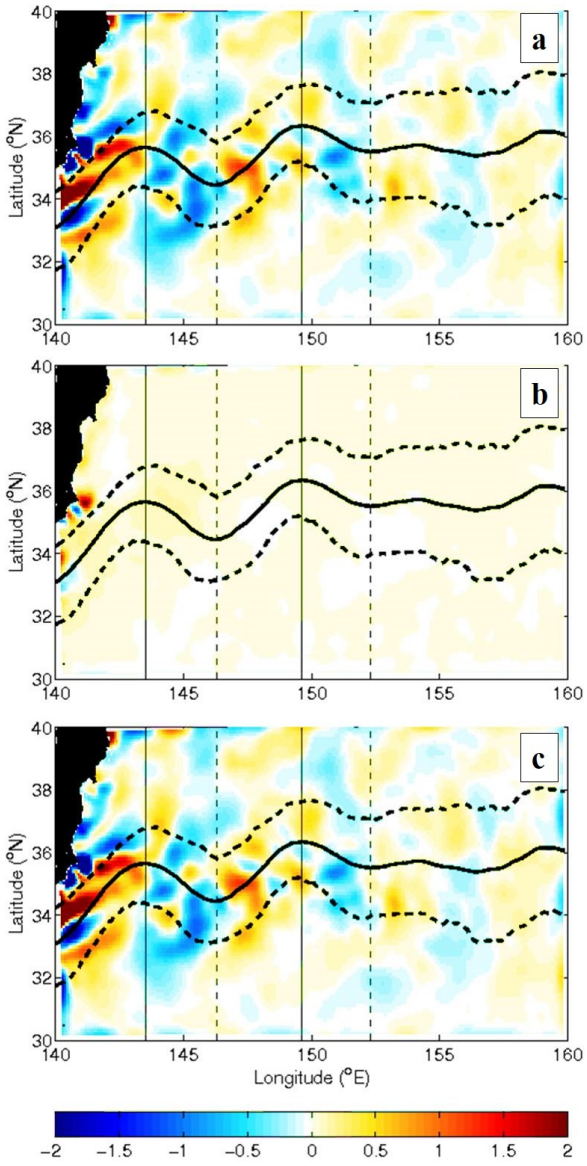

Figure 2.7: (a)-(c) 1995–2007 geographic mean eddy forcing terms in equation (2.7), vertically averaged 0–250 m, from POP. The terms are the depth- and time-averaged (a) $\overline{-\mathbf{u}' \cdot \nabla \zeta'}$, (b) $\overline{\zeta' w_z'}$, and (c) the total eddy forcing, $\overline{-\nabla \cdot (\mathbf{u}' \zeta')}$. Each term has been smoothed post-averaging with a Gaussian filter (0.2° e-folding scale, 1° cutoff radius). Thick black lines indicate the mean (solid) and 10th/90th percentile (dashed) jet axis positions. The thin vertical lines denote the longitudes of crests (solid) and troughs (dashed) in the mean jet path. The color scale is indicated at the bottom and is the same for (a)-(c), but different from Figure 2.6, with units of 10^{-11} s^{-2}.

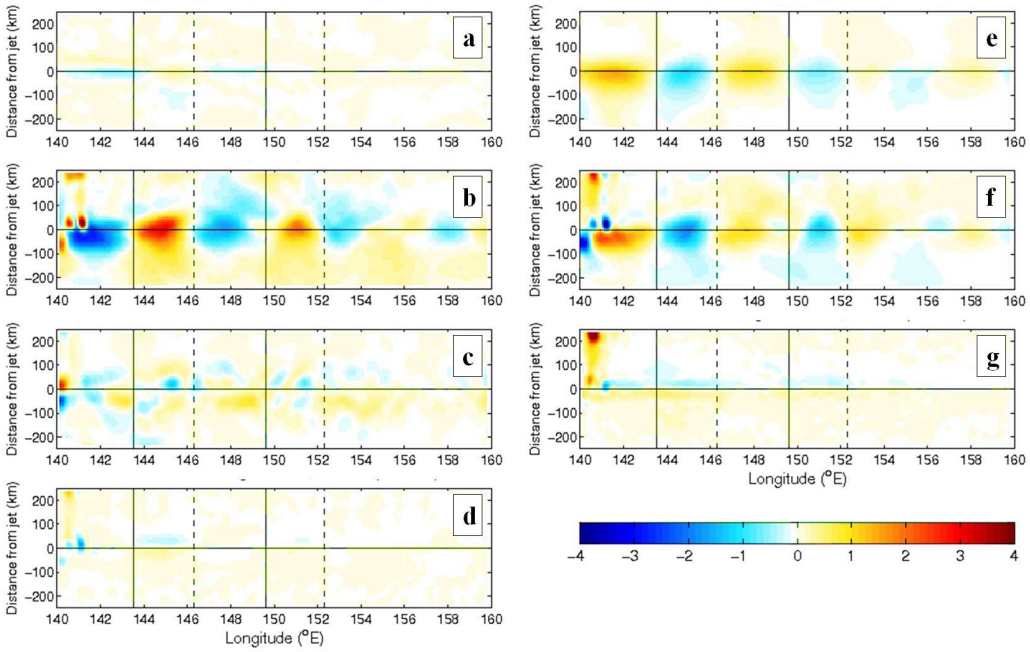

Figure 2.8: 1995–2007 jet frame time mean of the terms in the full vorticity budget in equation (2.8), vertically averaged 0–250 m, from POP. The terms are the depth- and jet frame time-averaged (a) $\overline{\left\langle \frac{\partial \zeta}{\partial t} \right\rangle}^{j}$, (b) $\overline{\langle \mathbf{u} \cdot \nabla \zeta \rangle}^{j}$, (c) $\overline{-\langle \zeta w_z \rangle}^{j}$, (d) $\overline{\langle W \rangle}^{j}$, (e) $\overline{\langle \beta v \rangle}^{j}$, (f) $\overline{-\langle f w_z \rangle}^{j}$, and (g) $\overline{\langle F \rangle}^{j}$, the residual. Each term has been smoothed post-averaging with a Gaussian filter (0.2° e-folding scale, 1° cutoff radius). Color scale is indicated in the lower right corner and is the same for (a)-(g), with units of 10^{-11} s^{-2}.

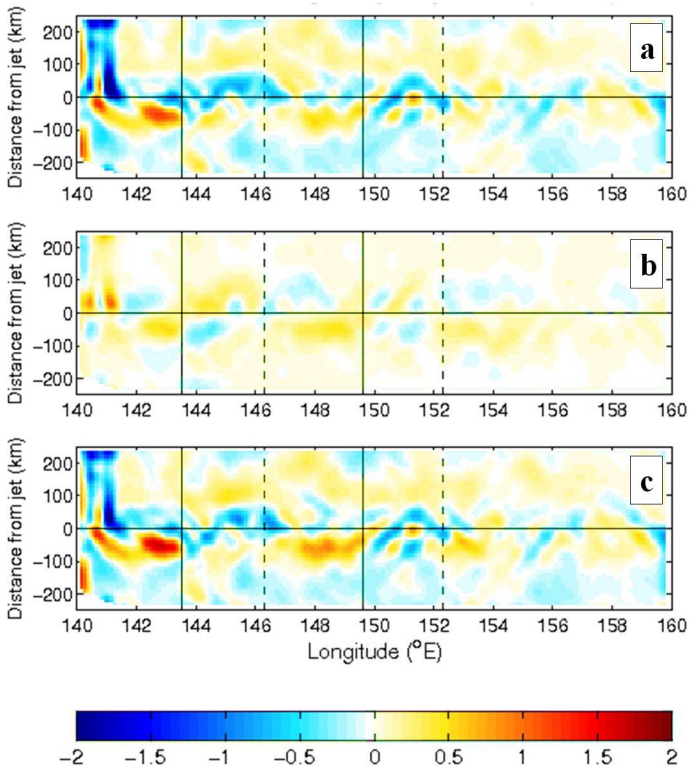

Figure 2.9: (a)-(c) 1995–2007 jet frame mean eddy forcing terms in equation (2.13), vertically averaged 0–250 m, from POP. The terms are the depth- and jet frame time-averaged (a) $\overline{-\left\langle (\mathbf{u}\cdot\nabla\zeta)'\right\rangle}^{j}$, (b) $\overline{\left\langle (\zeta w_z)'\right\rangle}^{j}$, and (c) the total eddy forcing, $\overline{\left\langle -(\nabla\cdot(\mathbf{u}\zeta))'\right\rangle}^{j}$. Each term has been smoothed post-averaging with a Gaussian filter (0.2° e-folding scale, 1° cutoff radius). Color scale is indicated at the bottom and is the same for (a)-(c), but different from Figure 2.8, with units of 10^{-11} s^{-2}.

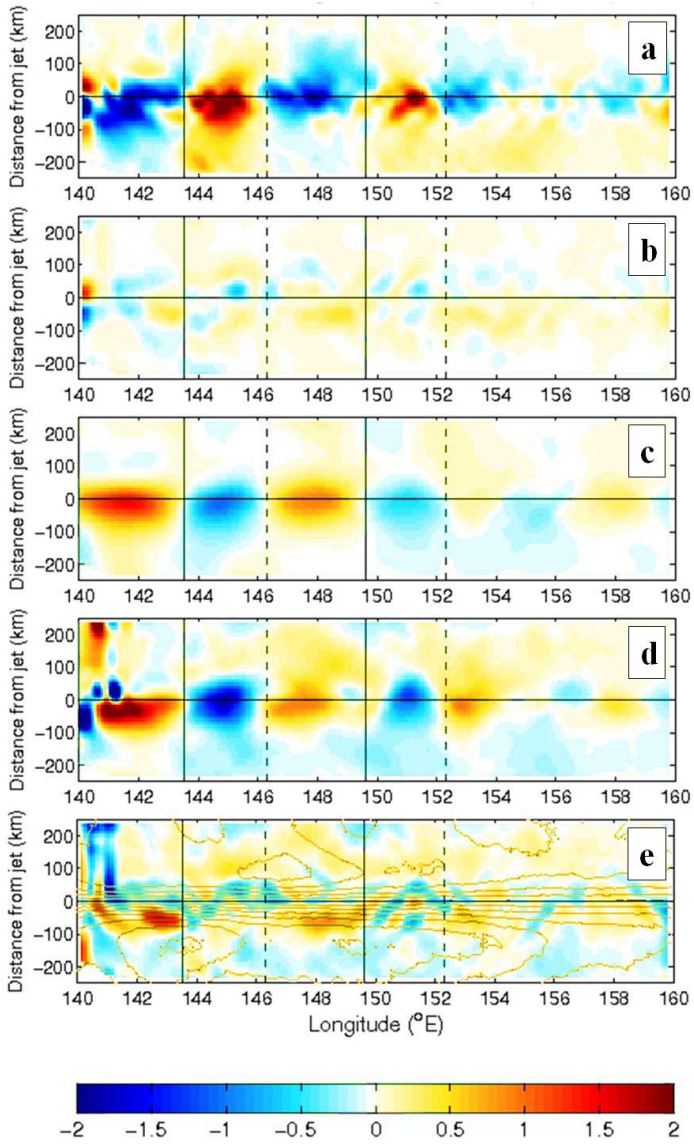

Figure 2.10: 1995–2007 jet frame mean (a)-(d) mean circulation terms in the vorticity budget in equation (2.13). The mean circulation terms are (a) $\overline{\left\langle \overline{\langle \mathbf{u} \rangle}^{j} \cdot \nabla \overline{\zeta}^{j} \right\rangle}^{j}$, (b) $\overline{-\left\langle \overline{\zeta}^{j} \overline{w_z}^{j} \right\rangle}^{j}$, (c) $\overline{\langle \beta v \rangle}^{j}$, and (d) $\overline{-\langle f w_z \rangle}^{j}$. (e) The total eddy forcing $\overline{\left\langle -\left(\nabla \cdot (\mathbf{u}\zeta)\right)' \right\rangle}^{j}$, with superimposed 1995–2007 jet frame mean SSH (thin brown contours, with a contour interval of 10 cm). Each term has been smoothed post-averaging with a Gaussian filter (0.2° e-folding scale, 1° cutoff radius). Color scale is indicated below (e) and is the same for (a)-(e), with units of 10^{-11} s^{-2}.

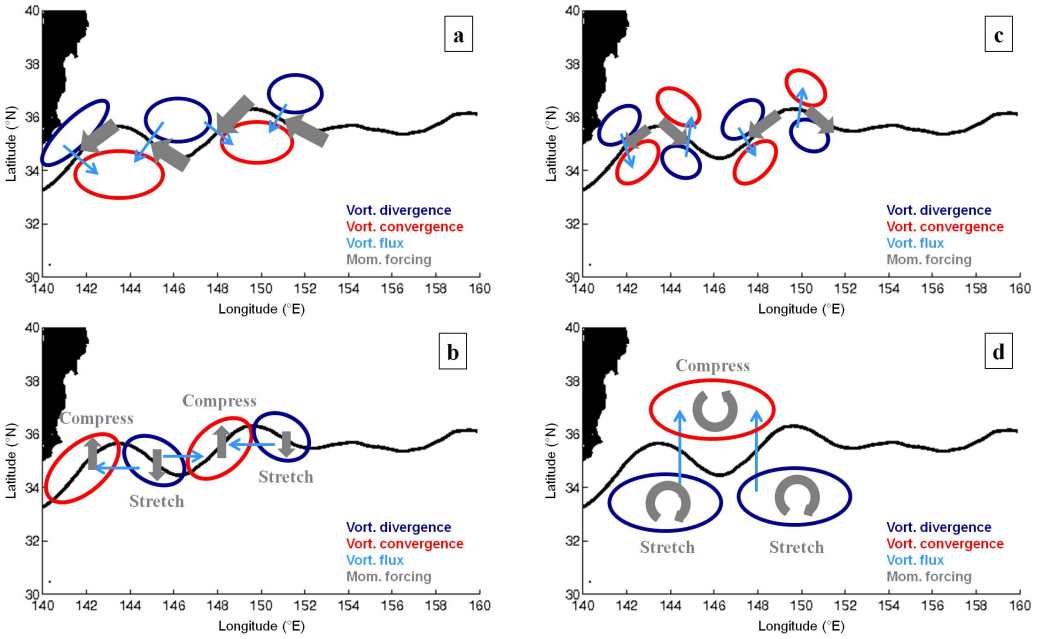

Figure 2.11: Schematic of eddy forcing patterns on the mean flow in the KE jet region; subplots show (a) Pattern 1 – jet core deceleration, (b) Pattern 2 – meander reinforcement, (c) Pattern 3 – intermittent jet core acceleration, and (d) Pattern 4 – forcing of recirculation gyres. The black line indicates the mean path of the KE jet. Ellipses indicate areas of eddy vorticity convergence (red) and divergence (dark blue), with the implied direction of eddy vorticity fluxes given by light blue arrows. The thick gray arrows illustrate the effective directions of the eddy momentum forcing from each pattern. Gray text indicates the vertical deformation of the upper layer due to the influence of the eddy forcing pattern.

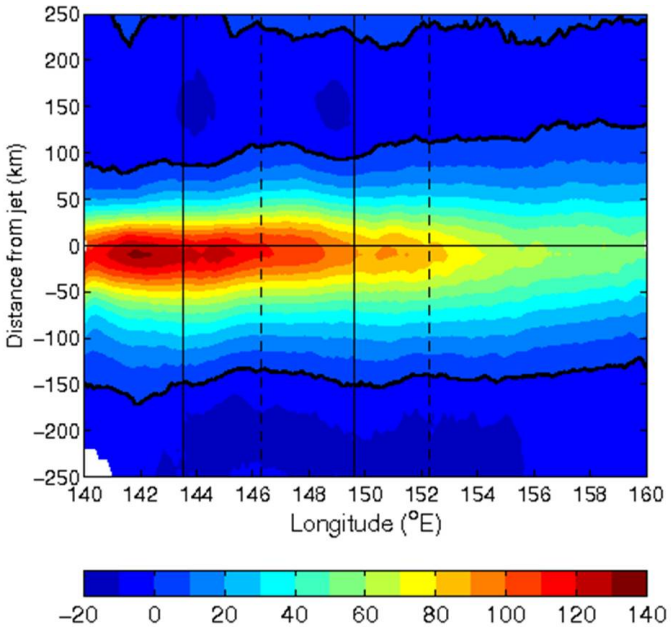

Figure 2.12: 1995–2007 jet frame mean along-jet velocity $\overline{\langle u_j \rangle}^j$, vertically averaged 0–250 m, from POP. The aspect ratio is distorted to highlight the along-jet changes in $\overline{\langle u_j \rangle}^j$. The color scale is indicated at the bottom, with units of cm s^{-1}.

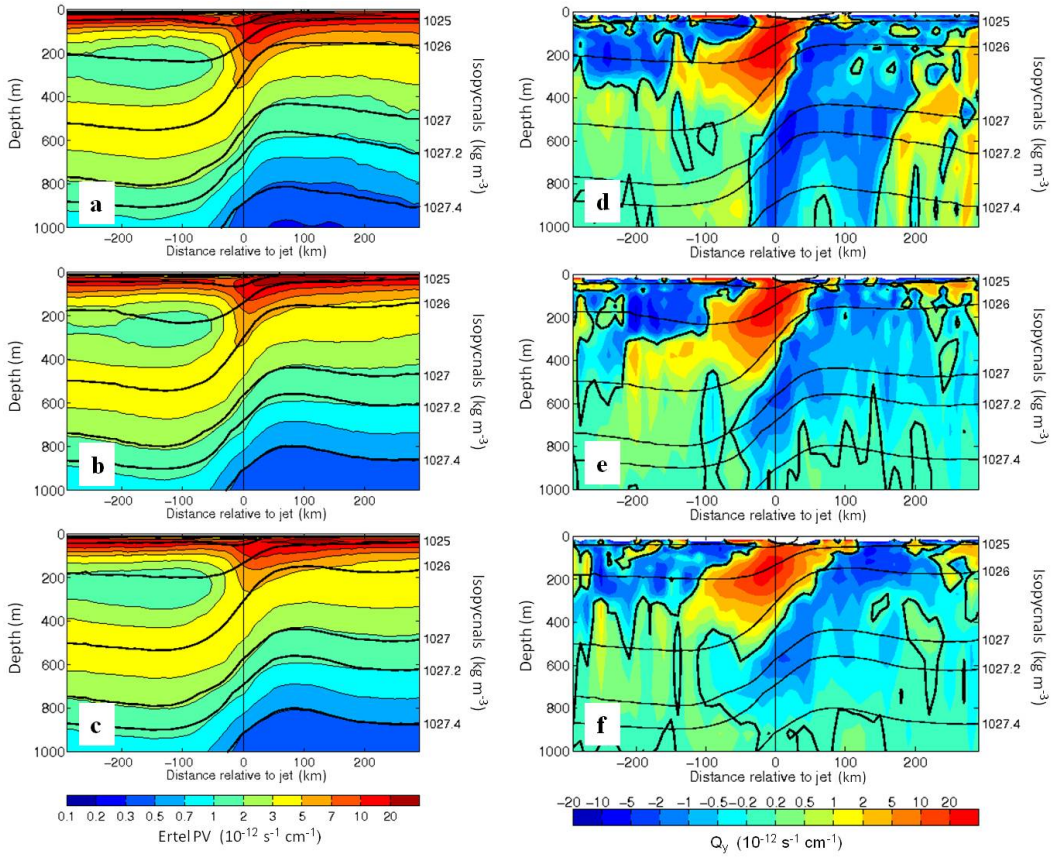

Figure 2.13: (a-c) Transects of Ertel potential vorticity from POP, 1995–2007 mean, with isopycnals (black contours) of potential densities relative to the surface (labeled on right axis) at (a) 142°E, (b) 145°E, and (c) 148°E. The color scale is indicated below (c), and is approximately logarithmic. (d-f) Same as (a-c), but colors indicate cross-jet gradient of Ertel potential vorticity (Q_y) along isopycnals. Thick black contours indicate zero crossings of Q_y, corresponding to reversals in the along-isopycnal Ertel PV gradient. The color scale is indicated below (f), and is approximately logarithmic for both negative and positive values of Q_y.

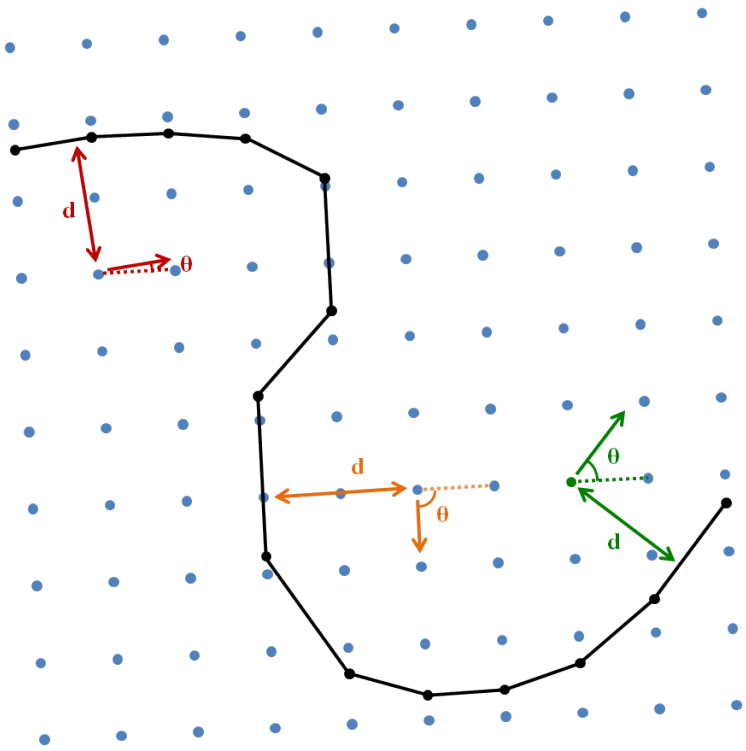

Figure 2.14: Schematic illustrating how d and θ are computed for sample model grid points, relative to a defined jet axis (black line and dots).

Table 2.1: Correlations and projections of mean terms M in the jet frame vorticity budget with the total eddy forcing $E = \overline{\left\langle -\left(\nabla \cdot (\mathbf{u}\zeta)\right)'\right\rangle}^{j}$. Both M and E first have cross-jet means at each longitude removed, to focus on the cross-jet varying part of the vorticity forcing that decelerates/accelerates the jet. The correlation of M with E is then given by $r_{ME} = [1/(\sigma_M \sigma_E)] \sum_i \sum_j M_{ij} E_{ij}$. The indicated p-values are for the correlation coefficients r_{ME} (Emery and Thomson, 2001) using the one-tailed Student's t-test, with effective degrees of freedom determined based on the decorrelation scale of the total eddy forcing in the region indicated. The forcing-normalized projection of M onto E is given by $P_{ME} = (1/\sigma_E^2) \sum_i \sum_j M_{ij} E_{ij} = r_{ME} * (\sigma_M / \sigma_E)$, with σ_X indicating the standard deviation of X. The normalization is such that the sum of the P_{ME} for all M terms is 1, though not all M terms are included below.

	Mean term M	Correlation r_{ME}	One-tailed p-value	Forcing-normalized projection P_{ME}
Within jet core	$\overline{\left\langle \overline{\langle \mathbf{u} \rangle}^{j} \cdot \nabla \overline{\zeta}^{j} \right\rangle}^{j}$	0.45	2×10^{-9}	0.47
	$\overline{-\left\langle \overline{\zeta}^{j} \overline{w_z}^{j} \right\rangle}^{j}$	0.38	8×10^{-7}	0.10
$-100\,\mathrm{km} < d < +60\,\mathrm{km}$	$\overline{\langle \beta v \rangle}^{j}$	0.28	3×10^{-4}	0.11
	$\overline{-\langle f w_z \rangle}^{j}$	0.47	2×10^{-10}	0.40
Outside of jet core	$\overline{\left\langle \overline{\langle \mathbf{u} \rangle}^{j} \cdot \nabla \overline{\zeta}^{j} \right\rangle}^{j}$	0.10	0.33	0.10
	$\overline{-\left\langle \overline{\zeta}^{j} \overline{w_z}^{j} \right\rangle}^{j}$	0.34	0.06	0.09
$-240\,\mathrm{km} \leq d \leq -100\,\mathrm{km}$ or	$\overline{\langle \beta v \rangle}^{j}$	0.21	0.17	0.09
$+60\,\mathrm{km} \leq d \leq +200\,\mathrm{km}$	$\overline{-\langle f w_z \rangle}^{j}$	0.63	5×10^{-4}	0.55

Chapter 3

A harmonic projection and least-squares method for quantifying Kelvin wave activity

Abstract

A new method for isolating the equatorial and coastal Kelvin wave signal from alongtrack satellite altimetry data is presented and applied to sea level anomaly (SLA) observations in the tropical Indian Ocean. The method consists of sequential projections onto the SLA data, starting with meridional or cross-shore Kelvin wave profiles derived from shallow water theory (y–projections). Next, Fourier basis functions in x-t (along-waveguide distance and time respectively) space with the phase speed ranges of Kelvin and Rossby waves are projected onto the y–projections. After projections in all three dimensions have been carried out, least-squares methods are applied to optimize the non–orthogonal basis function coefficients and minimize the misfit

of their along–waveguide forcing and dissipation. Lastly, the westward-propagating (Rossby wave-related) signals are removed, generating a Kelvin wave coefficient K that represents Kelvin wave activity. Along the Indian Ocean equatorial-coastal waveguide, Hovmöller diagrams of K show reduced high–wavenumber noise compared to analogous diagrams of pre-processed sea level anomaly. Results from a Monte Carlo simulation demonstrate that Kelvin wave signals generated *a priori* can be effectively isolated even when superimposed with strong Rossby waves; the signs of all but the weakest Kelvin waves are diagnosed correctly in over 90% of cases. When the method is applied to 21 years of satellite observations and the SLA signal associated with K is removed, the large residual in the equatorial SLA signal has a spatial distribution consistent with wind–forced Rossby waves. The equatorial SLA variability in the western part of the basin is poorly correlated with the SLA field associated with K, as the superimposed SLA profile of Rossby waves can distort the true origin locations of Kelvin waves in the raw SLA field. Therefore, this method offers improved tracking of Kelvin waves compared to the raw SLA dataset, and may provide the opportunity to study weakly nonlinear aspects of these waves by comparison with linear models.

3.1 Introduction

The quantification of ocean variability associated with equatorial long waves is a topic of great importance for understanding the tropical ocean and its role in climate. Since the advent of satellite altimetry, the surface manifestations of these waves and the wind forcing driving them have been tracked in datasets that now comprise over 20 years of continuous global coverage (e.g., Delcroix et al., 1994; Susanto et al., 1998; Boulanger and Menkes, 1999; Drushka et al., 2010). However, to use these observations

to better understand the behavior of these planetary waves and their relationship to climate variability, analysis techniques are needed that target the specific signatures of Kelvin and Rossby waves in satellite observations. In particular, the present study was motivated by a need to quantify the relative presence of upwelling vs. downwelling Kelvin waves in the equatorial Indian Ocean and along the coasts of Sumatra and Java, where they are influential in the evolution of Indian Ocean Dipole events as described in Chapter 4 (Delman et al., 2016b).

A variety of techniques have been employed to quantify equatorial long wave activity from satellite observations; these range from the application of sophisticated data assimilation techniques to meridional projections of sea level anomaly (SLA) data. The data assimilation approaches generally use a linear wave–propagation model, along with Kalman filters (e.g., Miller and Cane, 1989; Fu et al., 1993) or adjoints (e.g., Thacker and Long, 1988; Long and Thacker, 1989a,b) to incorporate observations. These techniques are particularly useful for cases where observations are sparse and error–prone, as is often the case for in–situ measurements, and also during the earlier years of satellite observations when spatial resolution was low (e.g., Geosat). As the spatial and temporal coverage of altimeter–derived remote sensing data increased, it was conceivable to estimate Kelvin and Rossby wave activity using solely meridional projections of SLA data, or a combination of SLA and current observations. Cane and Sarachik (1981) showed that vectors containing SLA and surface current profiles associated with a given vertical Kelvin wave mode and its associated meridional Rossby wave modes are orthogonal; this orthogonality provided the basis for an equatorial wave decomposition in numerous studies (e.g., Delcroix et al., 1994; Yuan et al., 2004; Yuan and Liu, 2009). Boulanger and Menkes (1995, 1999), BM9599 hereafter, also

carried out a decomposition using only meridional projections of SLA data that were reasonably consistent with projections derived from in–situ moorings. However, the decomposition of Kelvin and Rossby wave modes based on meridional projections of SLA alone are not orthogonal, and as Yuan et al. (2004) notes, this necessitates the inversion of an ill–conditioned matrix. An alternative approach used complex EOFs of SLA to separate Rossby and Kelvin wave signals in the equatorial Pacific (Susanto et al., 1998); one limitation of this method is that complex EOFs by definition constrain the along–waveguide and across–waveguide length scales of the waves, while shallow–water theory only constrains the across–waveguide length scale.

Here we build on the methodology of BM9599, by using the approximate phase speeds as well as cross–waveguide profiles to isolate the Kelvin wave signal. Starting with the SLA meridional projections of BM9599, we apply harmonic projections in the along–waveguide direction and in time, followed by a least–squares fit to optimize the non–orthogonal projection coefficients. The result is a Kelvin wave coefficient K that approximates Kelvin wave generation and dissipation along the waveguide, and can be used to track coastal as well as equatorial Kelvin waves. The method as described is focused only on an accurate representation of Kelvin (not Rossby) wave activity, though an extension of these techniques might enable a comprehensive decomposition of equatorial waves (as discussed in Section 3.4). The paper is structured as follows: Section 3.2 describes the satellite data used, and the harmonic projection and least–squares method that results in the Kelvin wave coefficient K. Section 3.3 estimates errors associated with the computation of K using a Monte Carlo simulation, and discusses qualitative and quantitative analyses of satellite observations to assess how effectively K describes Kelvin wave activity along the Indian Ocean waveguide.

Section 3.4 summarizes the strengths and weaknesses of the method, and considers the possibility of extending the method to quantify Rossby wave activity.

3.2 Method

3.2.1 Data

Our methodology quantifies Kelvin wave activity using AVISO Ssalto/Duacs alongtrack SLA data, specifically those from the TOPEX/Poseidon, Jason–1, and Jason–2 satellites. These satellites repeat their orbit over a given track approximately every 10 days, and the data have near–continuous coverage from September 1992 to December 2013. The reason for using alongtrack as opposed to the frequently–used gridded product is the increased spatial resolution in the along–track direction, $\sim 1/10^\circ$ compared to $1/3^\circ$ for gridded data. One of the advantages of this method is its utility for tracking waves in their transition from equatorial to coastal Kelvin waves. However, quantifying coastal Kelvin waves requires higher spatial resolution, as the baroclinic radius of deformation shrinks from $\sim$400 km at the equator to $\sim$100 km at 10°S. The disadvantage of using the alongtrack data is the large spacing between tracks in the zonal/alongshore direction ($\sim$ 300 km along the coast), but the spacing is still small relative to the along–waveguide length scale of Kelvin waves near the equator, typically >1000 km.

Due to the anisotropy of equatorial–coastal long waves, the offset angle between satellite tracks and meridional cross–sections at the equator is likewise considered to be negligible, and both ascending and descending tracks are used in the analysis. Along the Sumatra and Java coasts, only ascending (SW–NE oriented) tracks are

used in Kelvin/Rossby wave projections to best approximate a cross–shore profile. For computational expediency in the least–squares part of the solution, the method was applied to overlapping two–year subsets of the full data record, with each subset overlapping with the next one by a year. The results from each subset were then patched together using a tapered weighted averaging in the overlapping year to create a continuous field of K values for the 21–year period of record (i.e., with 20 subsets patched together). For comparison purposes and to present clear visual snapshots of variability in the Indian Ocean basin, gridded maps of SLA (MSLA) (Ducet et al., 2000) were also used to generate some of the figures in this paper.

3.2.2 Kelvin wave y–projections

The first step in the computation of the Kelvin wave coefficient K is to calculate the projection of the SLA data onto a meridional or cross–shore profile of a baroclinic Kelvin wave based on linear shallow–water theory (e.g., Gill et al., 1974; McCreary, 1981). We refer to this as the y–projection; for an equatorial Kelvin wave it is the same Gaussian profile given in Appendix A2 of Boulanger and Menkes (1995), but our analysis also considers coastal Kelvin waves for which the wave profile transitions to a decaying exponential away from the equator. For an equatorial–coastal Kelvin wave the profile is

$$h_K(y) = h_0 \exp\left[-\frac{\beta \cos\phi}{2c} y^2 \pm \frac{f_0}{c} y\right] \tag{3.1}$$

where y is the perpendicular distance relative to the equator or the coastline, h_0 is the amplitude (i.e., peak value) of the wave, f_0 is the Coriolis parameter at the latitude where the profile intersects the coast, and ϕ is the angle of orientation of the

coast relative to the east–west axis ($f_0 = 0$ and $\phi = 0$ for equatorial Kelvin waves). The sign in front of $(f_0/c)y$ for coastal Kelvin waves is chosen such that the term is always negative. As our focus here is on Indian Ocean Kelvin waves that are deflected to the south of the equator, y is negative and decreasing away from the coast, and $f_0 < 0$, so the sign is negative. The value of c for the meridional/cross–shore profiles in this analysis was taken to be 2.5 m s^{-1}. This value of c lies between the first–and second–mode baroclinic phase speeds for Kelvin waves in the region, as these two modes account for most Kelvin waves observed in Indian Ocean SLA (Drushka et al., 2010). However, using $c = 2.0$ m s^{-1} or 3.0 m s^{-1} does not produce a substantially different result.

Applied to the altimetry data, the Kelvin wave y–projection is given by

$$K_y = \frac{1}{2} \int_{-r}^{r} \left(h_{\mathrm{SLA}} - \overline{h_{\mathrm{SLA}}}\right) \frac{h_K - \overline{h_K}}{h_0} \, dy \tag{3.2}$$

for equatorial Kelvin waves and

$$K_y = \int_{-r}^{0} \left(h_{\mathrm{SLA}} - \overline{h_{\mathrm{SLA}}}\right) \frac{h_K - \overline{h_K}}{h_0} \, dy \tag{3.3}$$

for coastal Kelvin waves south of the equator, where h_{SLA} is the alongtrack altimetry profile, and r is the radius for the profile projection. The overbar indicates the meridional $\overline{a} = 1/(2r) \int_{-r}^{r} a \, dy$ or cross–shore $\overline{a} = 1/(r) \int_{-r}^{0} a \, dy$ mean (for equatorial and coastal waves respectively) of the profile a over the range being integrated. For the r value, we used 5° of latitude for equatorial Kelvin waves; r was then tapered to a distance equivalent to 3° of latitude along the coasts of Java and Nusa Tenggara to account for the smaller radius of deformation. We note that K_y is an integrated measure

of the sea level displacement; this type of measure is a more consistent indicator of Kelvin wave activity in the equatorial–coastal transition than peak amplitude, since without substantial dissipation, the peak amplitude of the wave tends to increase poleward as the radius of deformation decreases (Figure 3.1).

3.2.3 Projection using harmonic basis functions in x and t

After the Kelvin wave y–projections K_y are computed, the next step in our approach is to project K_y onto two–dimensional Fourier basis functions in along–waveguide distance x and time t. One method of separating these components is to assume that a vector $\mathbf{b}$ consisting of the alongtrack Kelvin wave projections K_y can be explained as a linear combination of two–dimensional Fourier basis functions

$$\mathbf{Am} = \mathbf{b} \tag{3.4}$$

where the columns of $\mathbf{A}$ are the basis functions $A^{\cos}_{m,n} = \cos\left[2\pi\left(k_m x - f_n t\right)\right]$ and $A^{\sin}_{m,n} = \sin\left[2\pi\left(k_m x - f_n t\right)\right]$ and x and t are along–waveguide distance and time respectively; the Fourier coefficients to be solved for are contained in the vector $\mathbf{m}$.

Basis functions $A_{m,n}$ that propagate from one side of the basin to the other at constant amplitude are most effective at representing Kelvin waves that similarly propagate across the basin with little change in amplitude. Kelvin waves that are forced and dissipate within the domain, especially with the low wavenumbers common to Kelvin waves, may have some of their energy aliased into westward–propagating signals. To resolve this aliasing issue, we introduce an additional tapering parameter

s to the basis functions (Figure 3.2). The basis functions $A_{m,n,s}$ take the form

$$A_{m,n,s} = \begin{cases} 0, & x \leq x_s - \Delta x \\ \left(1 - \frac{x_s - x}{\Delta x}\right) A_{m,n}, & x_s - \Delta x < x < x_s \\ A_{m,n}, & x \geq x_s \end{cases} \tag{3.5}$$

The tapering location x_s is varied at intervals of $\Delta x = 600$ km throughout the span of the waveguide, corresponding to the shortest wavelengths resolved along the coastal part of the waveguide (along the equator the effective Nyquist wavenumber is higher with more satellite tracks used). For $s = 1$, $x_s = x_W$ the western boundary, while for $s > 1$, $x_s = x_W + (s-1)\Delta x$. The forcing and dissipation of a wave within the domain can be expressed as the superposition of basis functions with varying s-values.

Furthermore, to reduce the number of basis functions and make the subsequent least–squares problem less underdetermined, we limit the basis functions to certain phase speed ranges associated with the waves we expect to observe using satellite altimetry. Therefore only basis functions $A_{m,n,s}$ corresponding to phase speeds $c_{m,n} = f_n/k_m$ typical of Kelvin waves (1.5 m s^{-1} $\leq c_{m,n} \leq$ 3.5 m s^{-1}), Rossby waves (-1.2 m s^{-1} $\leq c_{m,n} \leq -0.4$ m s^{-1}), and stationary signals ($k_m = 0$ or $f_n = 0$) are included in $A_{m,n,s}$, while the other basis functions are excluded. This phase–speed limitation reduces the number of basis functions to approximately twice the number of K_y values in $\mathbf{b}$. The tapered basis functions in $A_{m,n,s}$ corresponding to the phase speed ranges are projected onto the vector $\mathbf{b}$ containing the K_y values. First, a least–squares planar fit to $\mathbf{b}$ is removed, and then the basis functions are projected onto $\mathbf{b}$

$$\mathbf{m^P} = \mathbf{A}^T\mathbf{b} \tag{3.6}$$

producing a vector $\mathbf{m^P}$ of data projections that can be used to solve for the basis function coefficients $\mathbf{m}$ of identical size. For the projection values to be unbiased with respect to s, the projections are normalized by the size of the nonzero domain, expressed as a normalizing vector $\mathbf{n^P}$, with $n^P_{m,n,s} = (2/N)x_{\max}\left[x_{\max} - (x_s - 0.5\Delta x)\right]^{-1}$, and $N = \text{length}(\mathbf{b})$. Accordingly, the normalized vector of basis function projections is

$$\mathbf{m^{nP}} = \mathbf{n^P m^P} = \mathbf{n^P A}^T\mathbf{b} \tag{3.7}$$

3.2.4 Least–squares optimization and removal of westward–propagating signals

After the x–t projections have been carried out and normalized, basis function coefficients are recovered from the data projections in $\mathbf{m^{nP}}$ using least–squares methods; the solution is optimized to prevent a poorly-scaled solution with the cancellation of large coefficients in $\mathbf{m}$. In addition to constraining the size of the basis function coefficients $\mathbf{m}^T\mathbf{m}$, we chose to minimize the misfit of the rate of change in data projection values along the waveguide, $\partial\mathbf{m^{nP}}/\partial s$, in order to constrain high–wavenumber variability within the domain. We also minimize the misfit of the untapered data projection values, $\mathbf{m^{nP}}|_{s=1}$, to the $s = 1$ basis function coefficients. Hence the vector that we minimize the misfit for is

$$\mathbf{w}^T\mathbf{D}\mathbf{m^{nP}} = \mathbf{w}^T \begin{bmatrix} \mathbf{m^{nP}}|_{s=1} \\ \frac{\partial \mathbf{m^{nP}}}{\partial s}|_{s>1} \end{bmatrix} \tag{3.8}$$

where $\mathbf{D}$ is the identity operator for $s = 1$ projections, and the finite difference operator for $s > 1$ projections. The column vector $\mathbf{w}$ can be used to weight the elements of

$\mathbf{Dm^{nP}}$ relative to one another. In this case setting $\mathbf{w}$ to all ones was found to be sufficient, though accuracy may be gained in certain areas by adjusting the weighting vector; we speculate about one such case in Section 3.4. With $\mathbf{w}_n = 1$ for all n, we miminize the misfit of $\mathbf{Dm^{nP}}$ and the size of $\mathbf{m}^T\mathbf{m}$ using the cost function

$$L = \left[\mathbf{Dn^P A}^T(\mathbf{Am}) - \mathbf{Dm^{nP}}\right]^T \left[\mathbf{Dn^P A}^T(\mathbf{Am}) - \mathbf{Dm^{nP}}\right] + \lambda \mathbf{m}^T\mathbf{m} \tag{3.9}$$

Setting $\lambda = 0.1$ was found heuristically to produce the most credible reconstructions of the K_y values in $\mathbf{b}$, while reducing noise at the highest wavenumbers. The coefficient vector $\mathbf{m}$ is then given by

$$\mathbf{m} = \left[\left(\mathbf{Dn^P A}^T\mathbf{A}\right)^T \mathbf{Dn^P A}^T\mathbf{A} + \lambda\mathbf{I}\right]^{-1} \mathbf{Dn^P A}^T\mathbf{ADm^{nP}} \tag{3.10}$$

Finally, all coefficients of $\mathbf{m}$ that correspond to westward–propagating basis functions, i.e., $\mathrm{sgn}(f_n) = -\mathrm{sgn}(k_m)$, are set to zero. The resulting vector $\mathbf{m_K}$ is used to reconstruct the K_y field with the westward–propagating signals removed

$$\mathbf{b_K} = \mathbf{Am_K} \tag{3.11}$$

where vector $\mathbf{b_K}$ consists of the Kelvin wave coefficients K as a function of x and t. These computations are carried out for overlapping two–year subsets of the data, which are then merged to create a continuous field of K values for the period Sept. 1992–Dec. 2013 covered by the alongtrack SLA dataset.

3.3 Representations of Kelvin wave activity and error/variance estimates

3.3.1 Comparison of K values with raw SLA

To demonstrate how well K represents Kelvin wave activity, we present a case study where we compare the raw SLA along the IO equatorial–coastal waveguide during the year 1997 to the K_y and K values for the same period (Figure 3.3). The K_y and K values are calculated from the alongtrack SLA data at points where the satellite tracks cross the waveguide, hence these values are presented as points in Fig. 3.3b–c, whereas the raw SLA data from the gridded product are contoured in Fig. 3.3a. During the May–July period, the predominant feature in the raw SLA (Fig. 3.3a) is an eastward–propagating patch of elevated positive SLA, indicative of a downwelling Kelvin wave. However, the Kelvin wave y–projection (Fig. 3.3b) shows that this downwelling wave was both preceded and followed by upwelling Kelvin waves, both of which are much more evident in the Kelvin wave projection (Fig. 3.3b) than in the raw SLA (Fig. 3.3a). The y–projection still contains a number of westward-propagating signals (e.g., Jan.–Feb., and Oct.–Dec.) unrelated to Kelvin waves, and most likely represent Rossby waves flanking the equator. These westward–propagating signals are no longer visible in the K values for 1997 (Fig. 3.3c), and the trajectories of alternating upwelling and downwelling Kelvin waves are much more readily apparent.

The values of K can also be re–projected back into two spatial dimensions, to reconstruct the component of the SLA field that is associated with Kelvin wave activity. The reconstructed h_K is obtained by obtaining the wave amplitude h_0 associated with

K

$$h_0(x,t) = \frac{K(x,t)}{\int_{-r}^{0} \exp\left[-\frac{\beta\cos\phi}{2c}y^2 - \frac{f_0}{c}y\right]\, dy} \tag{3.12}$$

and substituting into (3.1). A comparison of the reconstructed h_K with gridded maps of SLA over a two–month period in 1997 (Figure 3.4) confirms that the Kelvin wave reconstruction is broadly consistent with the Kelvin wave activity suggested by the gridded SLA field, but also highlights some key differences. In late May and early June, an elevated SLA field persists in the eastern equatorial Indian Ocean (Fig. 3.4b–c), while the reconstructed h_K indicates that the Kelvin wave activity is changing sign from positive to negative there (Fig. 3.4g–h). In late June and early July, reconstructed h_K indicates that upwelling Kelvin wave activity is being generated from approximately 60°E eastward (Fig. 3.4i–j), while SLA is only substantially depressed east of 90°E (Fig. 3.4d–e). The discrepancy during this latter period is likely accounted for by the influence of downwelling Rossby waves on the SLA field in the central Indian Ocean; these waves have positive SLA maxima near the north and south radii of deformation, and would also elevate SLA (to a lesser extent) at the equator. Therefore, this implies that in the raw SLA field in early July 1997 (Fig. 3.4e) the upwelling Kelvin wave still present in the central equatorial Indian Ocean would not be apparent; this has potential implications for understanding the timing of the upwelling wave and where it was forced.

3.3.2 Monte Carlo–based error estimates

In order to place uncertainty bounds on the method's capacity to remove westward–propagating wave activity from the Kelvin wave estimate, we carried out

a Monte Carlo simulation. In this way the method could be applied to propagating waves whose amplitudes and K values were known *a priori*. We created 100 years of randomly–generated basis function coefficients $\mathbf{m}$, using Cholesky factorization (e.g., Gentle, 1998) to construct $\mathbf{m}$ fields whose local covariance statistics in wavenumber–frequency (k–f) space resemble values computed from the altimetry data, so that realistic Kelvin and Rossby wave signals could be generated. The $\mathbf{m}$ coefficients were adjusted so that their values are partially dependent on the local wave amplitude at the same wavenumber and frequency

$$\mathbf{m}|_{k,f,s} = \left[C_s \sum_{s'=1}^{s-1} \mathbf{m}|_{k,f,s'} \right] + \mathbf{r} \tag{3.13}$$

with C_s the location–dependent adjustment parameter and $\mathbf{r}$ the Cholesky decomposition–based random component. The variances of the basis functions were also adjusted so that the distributions of total Kelvin and Rossby wave variance along the waveguide are consistent with the variances obtained from satellite altimetry. Finally, after the artificially–generated eastward– and westward–propagating signals were combined, a small amount of white noise was added to the K_y fields; the variance of this noise is location–dependent and based on the variance in altimetry observations that could not be explained by either Kelvin or Rossby wave signals.

Once the artificial wave field was constructed, the harmonic projection and least–squares method described in sections 3.2.3–3.2.4 was applied to the artificial K_y field, and the K values derived from the basis function coefficients known *a priori* and deduced from the method were compared. An example of this for a given simulated year is shown in Figure 3.5; the artificially–generated K_y field contains signals propagating in both directions, though for most of the year the westward–propagating Rossby

waves appear to predominate (Fig. 3.5a). However, a consideration of the Kelvin wave signal $K_{\text{a priori}}$ in isolation (Fig. 3.5b) reveals that in addition to the very strong downwelling wave early in the year, a series of weak and moderate Kelvin waves propagate throughout the year. Many of these weaker waves are unidentifiable in the K_y field with the Rossby wave signals superimposed (Fig. 3.5a). However, the reconstructed Kelvin wave signal K_{reconst}, computed by applying the harmonic projection and least–squares method, recovers most of the weaker Kelvin waves in the $K_{\text{a priori}}$ signal and reproduces their approximate timing and intensity (Fig. 3.5c). In the few locations where visible discrepancies between $K_{\text{a priori}}$ and K_{reconst} are present (e.g., the intensities of the Kelvin waves in March–April, east of 90°E), high amplitude westward–propagating signals and/or sharp noisy gradients are present in the K_y field.

We now consider the error that is present in the reconstructed signal K_{reconst} relative to the original signal $K_{\text{a priori}}$, specifically $\epsilon = K_{\text{reconst}} - K_{\text{a priori}}$. When the 100–year artificial timeseries is analyzed, it is found that the normalized root–mean–square (RMS) error $\langle \epsilon^2 \rangle^{1/2} / \langle K^2_{\text{reconst}} \rangle^{1/2}$ is dependent on location along the waveguide as well as whether the fields are spatially– and temporally–filtered (Figure 3.6a). (Here the angle brackets $\langle\rangle$ denote temporal averaging over the entire 100–year time span of the simulation, but no spatial averaging other than filters applied prior to the error calculation.) The error in recovering the original Kelvin wave signal is highest near the equatorial–coastal transition of the waves, and on the eastern end of the domain; elsewhere it is confined to a fairly narrow range. However, the error magnitude also depends on whether a spatial or temporal averaging filter is applied prior to the error calculations. Except for the most error–prone regions, the error associated with unfiltered pointwise values of K is 50% to 60% of the total standard deviation of K.

If the K has a spatial moving average (boxcar) filter applied, but temporal averaging is limited to 10 day ranges (the resolution of the original points), the normalized error decreases slightly in most locations and is smoother across the waveguide. The error associated with 30–day moving averages of K (a typical timescale for intraseasonal Kelvin waves) decreases more substantially, to 35%–45% in most locations.

The probability and cumulative distribution functions associated with errors in K illustrate that errors of the same magnitude as the Kelvin waves themeselves are infrequent when a 30–day moving average filter is applied (Fig. 3.6b). Relative to the total standard deviation in filtered K, σ_K, the magnitude of the errors only exceed $0.5\sigma_K$ about 10% of the time (either positive or negative), and only exceed $1\sigma_K$ about 2.5% of the time. In this simulation, $\sigma_K \approx 1.9 \times 10^4$ m^2, so the error magnitude is less than 1×10^4 m^2 over 90% of the time. If the error is considered relative to the magnitude of the filtered reconstructed K_{reconst} at each location and time, the error variance is somewhat larger. Even so, with the weakest Kelvin waves ($|K_{\text{reconst}}| < 0.3\sigma_K$) excluded, the error will only result in misdiagnosing the sign of most Kelvin waves (i.e., $\epsilon/K_{\text{reconst}} > 1$) approximately 8.5% of the time. Moreover, the 8.5% incidence decreases further if the threshold for excluding weak Kelvin waves is raised (approximately 5.5% for a $0.5\sigma_K$ threshold and 2% for a $1\sigma_K$ threshold); thus sign misdiagnosis using this method is rarely a problem for moderate and strong Kelvin waves.

3.3.3 Kelvin wave–related and unrelated SLA characteristics

For a more comprehensive view of the variability encapsulated by the Kelvin wave coefficient K described here, we also consider the reconstructed Kelvin wave–

associated SLA field h_K, in the context of the total SLA field h_{SLA} observed by satellites over the 21–year period from 1992 to 2013. The SLA at each point in space and time can be considered as the sum of the reconstructed h_K and a residual h_{res}

$$h_{\mathrm{SLA}} = h_K + h_{\mathrm{res}} \tag{3.14}$$

with h_{res} in theory encompassing contributions to the SLA field from processes unrelated to Kelvin waves, including Rossby and other planetary waves. Figures 3.7a,b illustrates the variances of h_K and h_{res} respectively, normalized by h_{SLA}. The variance ratios of both h_K (Fig. 3.7a) and h_{res} (Fig. 3.7b) to h_{SLA} exceed 1 along some parts of the waveguide, though this is more commonly the case with h_{res}. (NB: The variance ratios can exceed 1, since the h_K and h_{res} fields are generally not orthogonal. Thus we do not describe the variance ratios as "explained variance" in the traditional sense, but rather compare the variances attributed to Kelvin waves vs. the residual to examine whether the residual signal is consistent with other phenomena such as Rossby waves.)

Additionally, we compute the correlation between h_K and the total h_{SLA} and h_{res} fields (Figure 3.8), to consider whether the sign of Kelvin wave activity covaries with that of the total SLA field and the residual. The effective degrees of freedom N^* for the correlations in Fig. 3.8 were computed from the decorrelation timescales of h_K. With 21 years of data, values of N^* range from approximately 50 to 500 over the spatial domain, with decorrelation timescales ranging from intraseasonal to semiannual. (For $N^* = 50$, correlation coefficient magnitudes exceeding 0.23 exceed the 95% confidence threshold; for $N^* = 500$ this threshold is approximately 0.08.) The correlation of h_K to h_{SLA} along the waveguide (Fig. 3.8a) is strongly positive in the eastern part of the basin and along the coast, but insignificant or negative in

the western part of the basin. The correlation of h_K to h_{res} is negative over nearly the entire domain, suggesting the tendency of h_K and h_{res} to be of opposite sign and explaining how h_{res} in particular can have a much larger variance than the total SLA field.

The variance ratios (Fig. 3.7) and correlations (Fig. 3.8) suggest different contributions from h_K and h_{res} variability in at least four distinct regions along the waveguide. In the western and central parts of the equatorial basin, even the maximum variances of h_K near the equator are only slightly more than half the variance associated with h_{res}. In this equatorial region, it is likely that most of h_{res} can be attributed to Rossby waves; indeed a linear wind–forced model of equatorial waves (Nagura and McPhaden, 2010) has shown that in the western part of the basin, Rossby waves are associated with a higher SLA standard deviation than Kelvin waves, even at the equator where Kelvin wave variability peaks. The correlation of h_K and h_{res} (Fig. 3.8) is also strongly negative here, consistent with the expected response of the ocean to a uniform zonal wind forcing, which would generate Kelvin and Rossby waves of opposite sign. In the eastern part of the basin and along the coast of Sumatra, the variances of h_K and h_{res} are more comparable, though this does not quite resemble the results from the linear forced model (Nagura and McPhaden, 2010) which show a much larger component of SLA due to Kelvin waves than Rossby waves. Near the coast of Java, the variance of h_K is much larger than that of h_{res}, suggesting that most of the SLA variability in this area can be attributed to coastal Kelvin waves. Along Nusa Tenggara (NT) the variance of h_{res} is once again comparable to or greater than h_K; this may be due in part to the complexity of the islands and bathymetry here. It is also likely that the computation of K does not accurately resolve the splitting

and diversion of Kelvin wave energy through Lombok Strait between Java and NT (e.g., Syamsudin et al., 2004; Drushka et al., 2010), since the least–squares fit exhibits a preference for slow tapering of K rather than the abrupt change in wave activity associated with the narrow strait.

Finally, the lack of a robust correlation between h_K and h_{SLA} along the equator in the western part of the basin (Fig. 3.8) implies that using raw SLA to track Kelvin wave propagation may not accurately represent where waves originate. Namely, SLA crests and troughs that only become clearly apparent in the eastern part of the basin may actually have origins further west; some specific cases of this are evident when comparing the SLA and K values for 1997 (Fig. 3.3a, c).

3.4 Conclusions

The harmonic projection and least–squares method outlined here produces a measure of Kelvin wave activity that can be applied directly to satellite observations of SLA, not only along the equator, but also along low–latitude coastal waveguides. The method removes the westward–propagating signals (i.e., Rossby wave signals) along such waveguides, and produces K coefficients that represent the time variability of Kelvin wave activity at each location along the waveguide. When filtered to remove sub–monthly temporal variability, the values of K have an RMS error of approximately 0.4 times the local standard deviation of K at most points along the waveguide; excluding the weakest waves, the method also diagnoses the sign of the Kelvin waves correctly over 90% of the time. A decomposition of the near–equatorial SLA into Kelvin wave–associated and residual components generates a residual field generally consistent with the activity of wind–forced Rossby waves, which tend to be

of the opposite sign of the Kelvin waves on which they are superimposed. Therefore the use of this method helps to isolate the Kelvin wave–associated SLA signal; it also allows for some variation in the phase speed of the waves, so a comparison of K values with the results of linear wind–forced models of equatorial waves (e.g., Yu and McPhaden, 1999; Nagura and McPhaden, 2010) may be useful in studying some weakly nonlinear aspects of Kelvin waves.

It is notable that the SLA along the equator in the western Indian Ocean is not robustly correlated with Kelvin wave activity deduced from this method, a result that has important implications for the interpretation of SLA variability at the equator. The use of this method in Chapter 4 helps show that the SLA signal of numerous intraseasonal Kelvin waves can be traced to the western equatorial Indian Ocean and co–located with zonal wind stress forcing (Delman et al., 2016b); therefore the lack of readily identifiable eastward–propagating sea level anomalies at the equator at a given time does not necessarily imply that Kelvin waves are absent. Rossby waves may be obscuring the Kelvin waves' signal on the western side of the basin, and the computation of K may assist in tracking Kelvin waves from their true generation region.

We also observe two limitations of the harmonic projection/least–squares method in the form presented here, and consider how these might be addressed. The first is the difficulty of resolving Kelvin wave activity to the east of Lombok Strait ($\sim$115°E), as evidenced by the abrupt increase in residual variance h^2_{res} (Fig. 3.7b) and decrease in h_K–h_{SLA} correlation (Fig. 3.8a) from the Java to the NT coastline. Prior analyses of altimetric SLA (Syamsudin et al., 2004; Drushka et al., 2010) indicate that about 30–50% of the Kelvin wave energy from the Java coastline continues eastward

along the NT coastline; the rest of the energy is presumed to transit north through Lombok Strait. In terms of our method, which does not track Kelvin wave energy through the strait, this would require an abrupt "dissipation" of Kelvin wave activity at Lombok Strait, which is likely not resolved by our tapered basis functions. Moreover, the overall skill of the method decreases approaching the eastern boundary of our domain and the complex topography of the Savu Sea region. One possible way to resolve the abrupt change in Kelvin wave energy across the strait using our method is to adjust the weighting $\mathbf{w}$ of the misfit of the vector in (3.8). Namely, the misfit for the tapers that span the Lombok Strait region could be weighted more heavily, so that there is less tendency for the model to continue steady propagation of Kelvin waves past the strait. Additionally, a finer tapering scale (e.g., $\Delta x = 300$ km instead of 600 km) could be adopted in this particular region, though errors due to altimetry interactions with land may still present challenges.

The second issue is that this method was developed with the specific goal of isolating Kelvin waves, while the SLA signal due to Rossby waves is treated as a residual. By contrast, linear wind–forced models and prior studies that have used SLA projections have sought to quantify the activity of Kelvin and gravest–mode equatorial Rossby waves simultaneously. The variance ratios (Fig. 3.7) and correlations (Fig. 3.8) suggest that the majority of the residual SLA field along the equator can be attributed to Rossby wave activity, and in principle there is no reason why our method could not be expanded to specifically target Rossby waves as well. One possible alteration to our method is to carry out the y–projections and the x,t–projections simultaneously; i.e., link each propagating basis function to the y–profile of a Kelvin or Rossby wave mode depending on its phase speed. Isolating the SLA displacement associated with each

mode would allow for a more complete picture of equatorial dynamics to be deduced from satellite altimetry, and this altered method will be explored in a future study.

3.5 Acknowledgements

Andrew Delman (ASD) was supported by a NASA Earth and Space Science Fellowship, grant number NNX13AM93H. Janet Sprintall (JS) and Julie McClean (JLM) were supported by NASA award number NNX13AO38G. Lynne Talley (LDT), JLM, and ASD were also supported by NSF grant OCE–0927650. The altimeter products were produced by Ssalto/Duacs and distributed by Aviso, with support from CNES (http://www.aviso.oceanobs.com/duacs/). Computations were carried out on the Geyser cluster within the Yellowstone computing environment hosted by the National Center for Atmospheric Research (NCAR).

Chapter 3, in full, consists of material that has been submitted for publication in Ocean Science, by Delman, A. S., J. Sprintall, J. L. McClean, and L. D. Talley. I was the primary investigator and author of this paper; the co-authors supervised and assisted with the preparation of the manuscript.

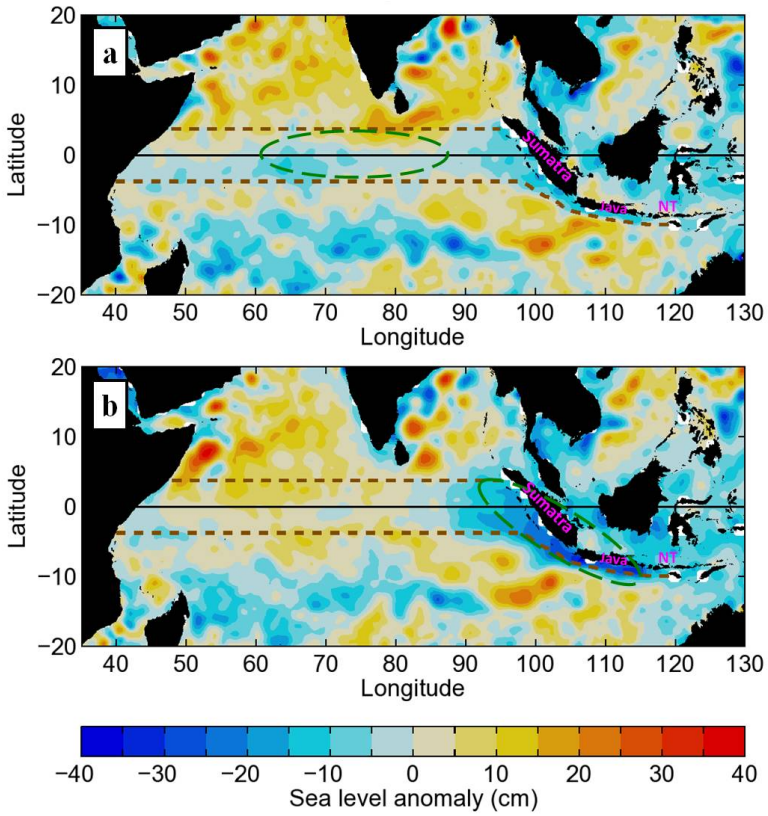

Figure 3.1: AVISO gridded sea level anomaly (SLA) in the Indian Ocean basin, on (a) June 25, 1997 and (b) July 16, 1997, with upwelling Kelvin waves (depressed SLA) peaking in the central Indian Ocean and along the Sumatra/Java coasts respectively (green dashed ellipses). The brown dashed lines indicate the radii of deformation for 1st baroclinic mode Kelvin waves, with the radius extended along the Indonesian coastal waveguide south of the equator. The locations of Sumatra, Java, and Nusa Tenggara (NT) are also indicated.

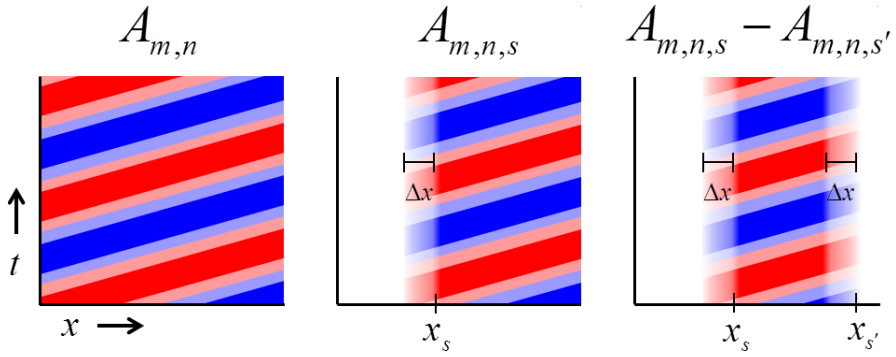

Figure 3.2: Schematic illustrating the use of tapered basis functions. (a) Profile of a non–tapered two–dimensional basis function $A_{m,n}$ in x and t. (b) Profile of a tapered basis function $A_{m,n,s}$, with tapering location $x = x_s$ and a tapering window of Δx. (c) Profile of two superimposed basis functions $A_{m,n,s} - A_{m,n,s'}$, with tapering locations of $x = x_s$ and $x = x_{s'}$ respectively; the superposition of two or more tapered basis functions allows for the forcing and dissipation of waves.

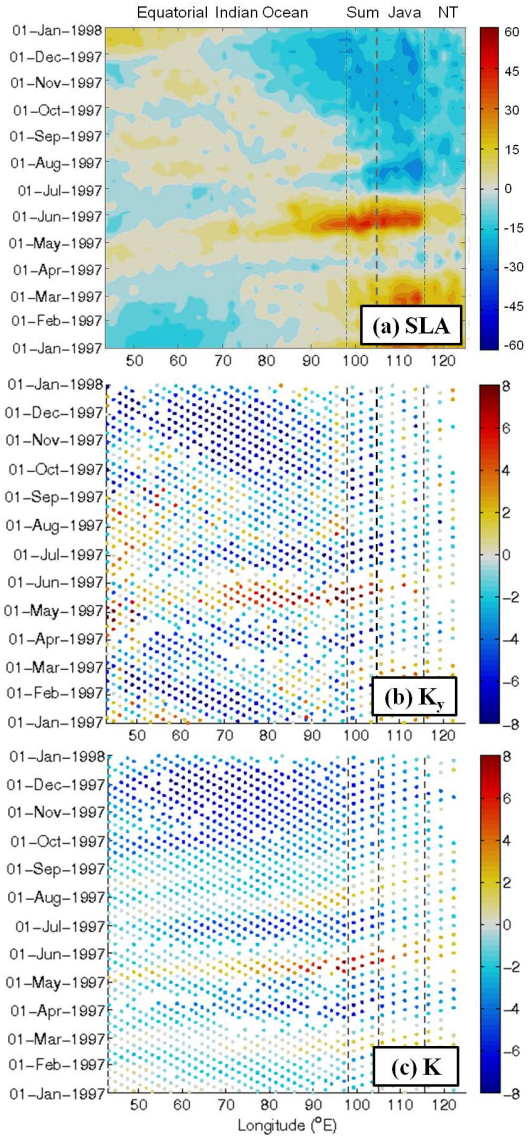

Figure 3.3: (a) Sea level anomaly (SLA) along the waveguide that crosses the equatorial Indian Ocean and follows the coasts of Sumatra, Java, and Nusa Tenggara, during 1997. The data plotted are from the 1/3° gridded AVISO product, in units of cm. (b) Kelvin wave y–projections K_y along the waveguide during 1997, derived from the alongtrack SLA data collected by the TOPEX/Poseidon satellite during 1997, in units of 10^4 m^2. (c) The Kelvin wave coefficient K values during 1997, in units of 10^4 m^2. The vertical dashed lines in each plot indicate (from left to right) the locations of the equatorial–coastal transition (98°E), the Sumatra–Java transition at Sunda Strait (105°E), and the Java–Nusa Tenggara transition at Lombok Strait (115.65°E).

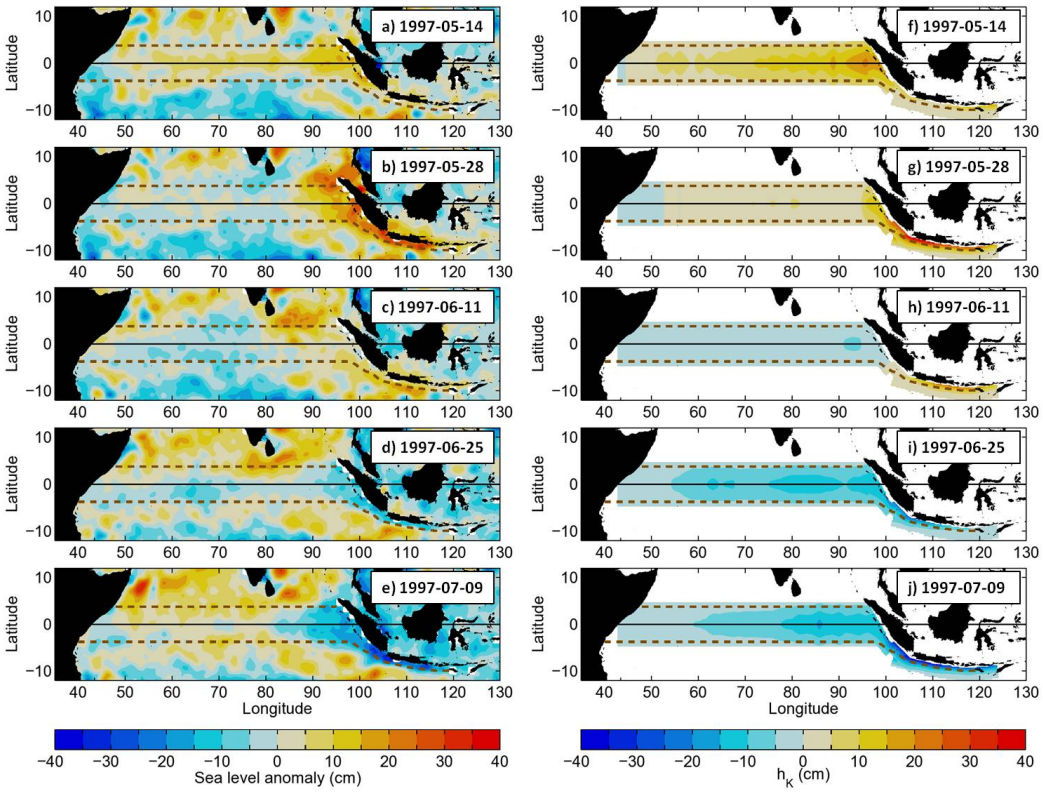

Figure 3.4: Maps of (a)-(e) SLA and (f)-(j) reconstructed h_K, the Kelvin-wave associated SLA, for snapshots (dates in the top-right corner of each panel) over a 2-month period in 1997. As in Fig. 3.1, the brown dashed lines indicate the radii of deformation for 1st baroclinic mode Kelvin waves.

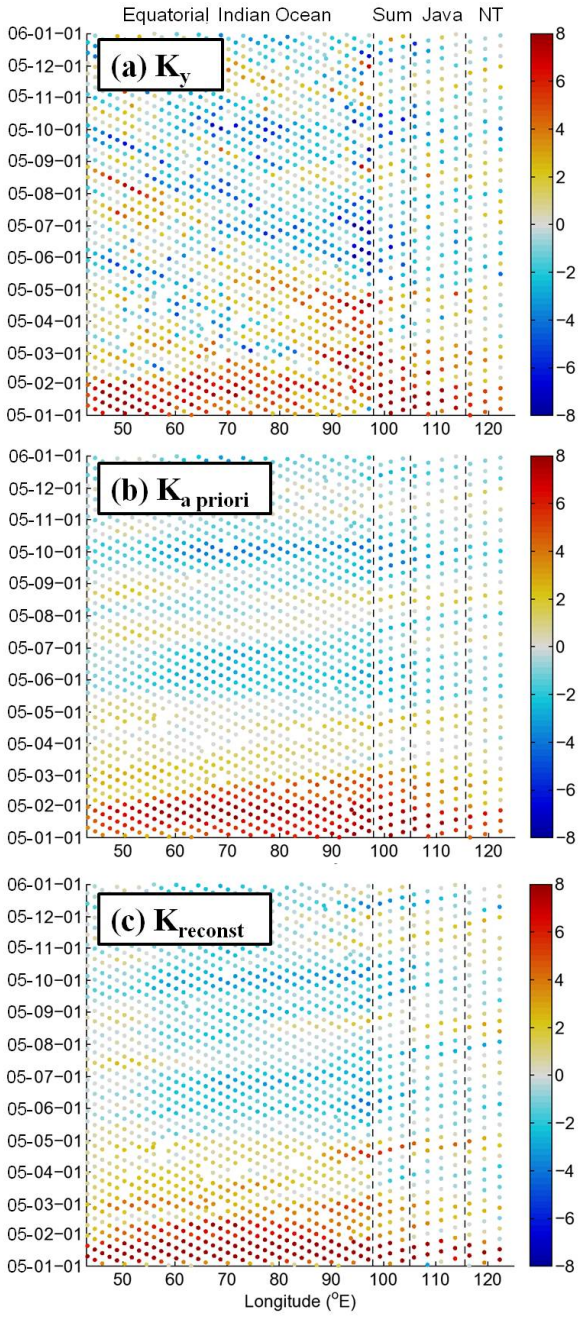

Figure 3.5: (a) Kelvin wave y-projection values K_y from year 5 of the Monte Carlo simulation, along the Indian Ocean equatorial-coastal waveguide. (b) Kelvin wave coefficient values $K_{\text{a priori}}$ generated in year 5 of the Monte Carlo simulation. (c) Reconstructed Kelvin wave coefficient values K_{reconst} for year 5 of the Monte Carlo simulation, obtained using the harmonic projection and least-squares method. All quantities are given in units of 10^4 m^2.

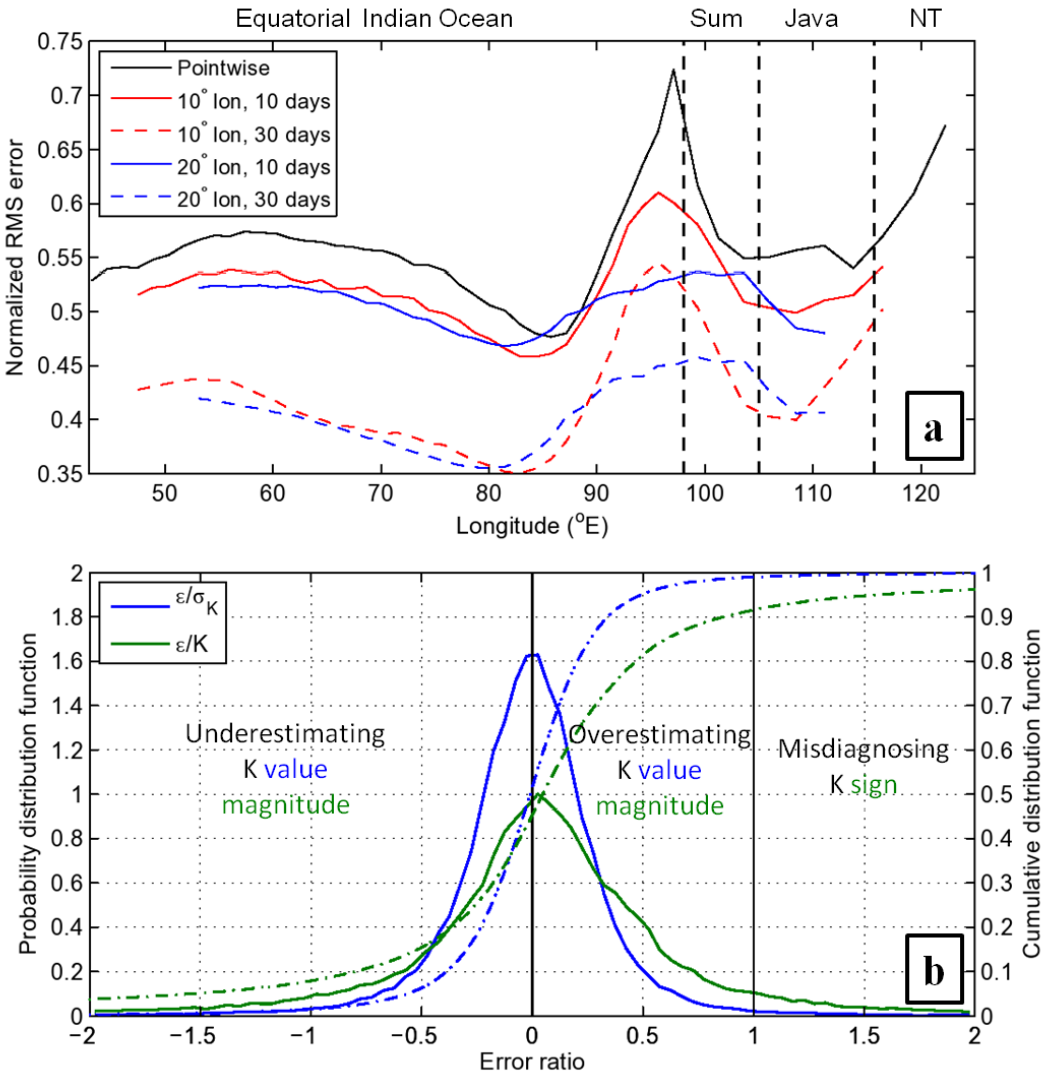

Figure 3.6: (a) Normalized root-mean-square (RMS) error estimates for K as a function of longitude along the waveguide, based on the 100–year Monte Carlo simulation and computed as $\langle \epsilon^2 \rangle^{1/2} / \langle K^2 \rangle^{1/2}$. The different curves show the effect on RMS error of applying spatial and temporal moving average filters to the *a priori* and reconstructed K values. (b) The probability distribution function (solid lines) and cumulative distribution function (dashed-dotted lines) of normalized error, with a 20° longitude and 30 day moving average filter applied prior to the error computation. The curves are shown for two different normalizations: (blue) normalized by the standard deviation of K over all longitudes and times ϵ/σ_K, and (green) normalized by the filtered reconstructed value K_{reconst} for each longitude and point in time $\epsilon/K_{\text{reconst}}$; in the latter case errors associated withe values of $|K_{\text{reconst}}| < 0.3\sigma_K$ have been excluded.

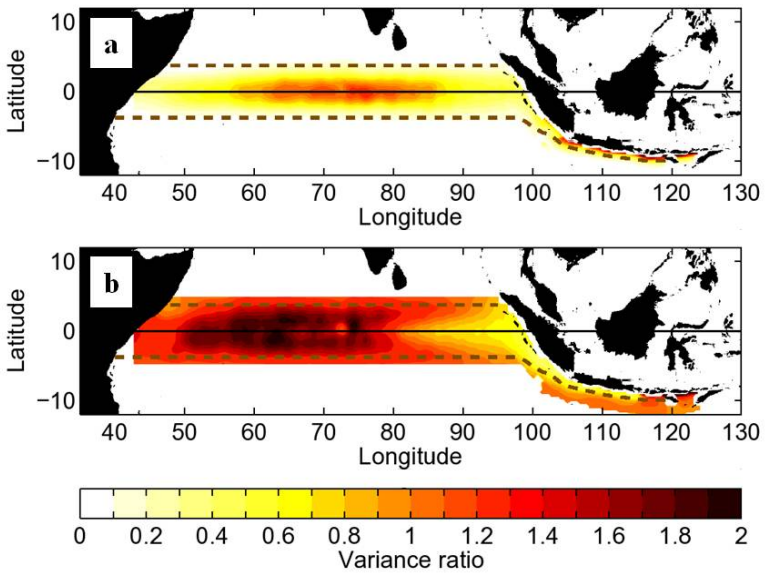

Figure 3.7: (a) The variance ratio of Kelvin wave–associated SLA to total SLA, $\langle h_K^2 \rangle / \langle h_{\rm SLA}^2 \rangle$. (b) The variance ratio of the residual to total SLA, $\langle h_{\rm res}^2 \rangle / \langle h_{\rm SLA}^2 \rangle$. The annual and semiannual harmonics have been removed by linear regression.

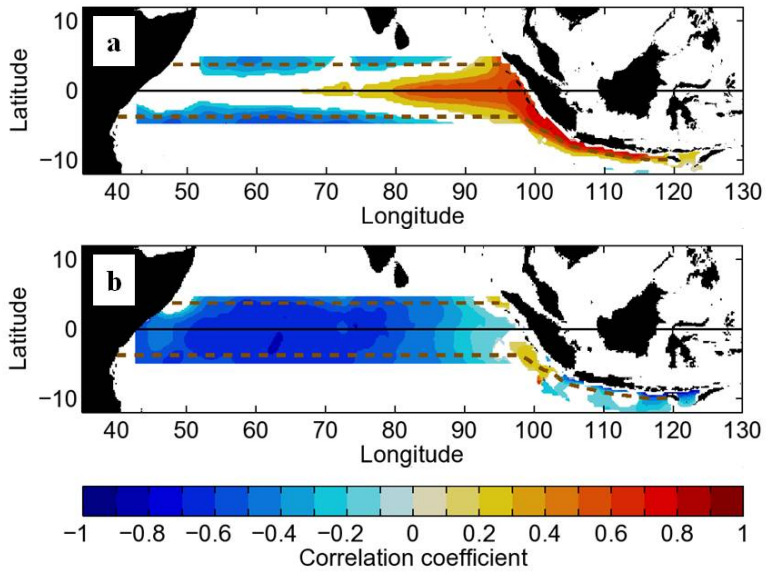

Figure 3.8: (a) The correlation coefficient of Kelvin wave–associated SLA to total SLA, $\langle h_K h_{\mathrm{SLA}} \rangle / \left[\langle h_K^2 \rangle \langle h_{\mathrm{SLA}}^2 \rangle \right]^{1/2}$. (b) The correlation coefficient of Kelvin wave–associated SLA to the residual, $\langle h_K h_{\mathrm{res}} \rangle / \left[\langle h_K^2 \rangle \langle h_{\mathrm{res}}^2 \rangle \right]^{1/2}$. The annual and semiannual harmonics have been removed by linear regression. Only correlation coefficients exceeding the 95% confidence threshold for significance (based on a Student's t–distribution) are shaded.

Chapter 4

Anomalous Java cooling at the initiation of positive Indian Ocean Dipole events

Abstract

Anomalous SST cooling south of Java during austral fall and winter (May–September) is an important precursor to positive Indian Ocean Dipole (pIOD) events. The Java SST anomalies are spatially and temporally coincident with seasonal upwelling induced locally by southeasterly trade winds. However, interannual variability of Java SST during the upwelling season is driven by remote forcing from winds along coastal Sumatra, in the equatorial Indian Ocean (EqIO), and in the vicinity of Lombok Strait. The wind forcing in the EqIO and along coastal Sumatra does not initiate SST cooling locally due to a deep thermocline and thick barrier layer, but can force upwelling Kelvin waves that induce substantial surface cooling once they

reach the seasonally shallower thermocline near the coast of Java. Satellite altimetry and a novel decomposition method involving harmonic projections and least–squares optimization are used to estimate interannual changes in Kelvin wave activity along the equatorial–coastal waveguide. All pIOD years in the satellite record have more wind–forced upwelling than downwelling Kelvin wave activity during April–June, suggesting that upwelling waves during this season are necessary for pIOD event development. However, a change to wind–forced downwelling Kelvin waves during July–August can abruptly terminate cool Java SST anomalies and weaken the pIOD event. Sumatra and Lombok Strait wind stress anomalies are the dominant drivers of the Java SST anomaly early in the upwelling season, but upwelling Kelvin wave activity in the EqIO during April–June is the most robust predictor of a pIOD event later in the calendar year.

4.1 Introduction

Indian Ocean waters to the south of Java are characterized by seasonal upwelling and surface cooling, induced by upwelling–favorable southeasterly trade winds during June–September (Wyrtki, 1962; Susanto et al., 2001). While the values of SST observed during the upwelling season are not as cool as in other major low–latitude upwelling regions (e.g., Peru, Benguela), the Java SST cooling stands in marked contrast to the rest of the Indo–Pacific warm pool; moreover, its interannual variability plays an integral role in the evolution of the Indian Ocean Dipole (IOD) (e.g., Saji et al., 1999; Webster et al., 1999; Vinayachandran et al., 1999). A positive IOD (pIOD) event, consisting of cold SST anomalies in the eastern equatorial Indian Ocean (EqIO) and warm anomalies in the western EqIO, manifests initially as cool SST anomalies south

of Java during approximately May–July (Saji et al., 1999; Feng and Meyers, 2003; Xiang et al., 2011). As this coincides with the onset of seasonal Java upwelling, the cooling in pIOD years is observed as an enhancement of the seasonal cooling. Once anomalous cooling has been established south of Java in early austral winter, cool SST anomalies may spread throughout the eastern EqIO (the IOD's eastern pole), typically during August–October (e.g., Saji et al., 1999; Susanto et al., 2001).

Studies of pIOD events (e.g., Li et al., 2003; Annamalai et al., 2003; Fischer et al., 2005; Zhong et al., 2005; Song et al., 2007; Roxy et al., 2011; Guo et al., 2015) have generally attributed the advent of cool SST anomalies to anomalous winds, either in the EqIO or along the Sumatra and Java coasts. Guo et al. (2015) consider three distinct mechanisms for generating pIOD events: a Walker circulation anomaly induced by a developing El Niño, an anomalous SST pattern in the year following El Niño that produces easterly wind anomalies in the EqIO, and anomalous cross–equatorial winds in the EqIO. All three of these mechanisms force the ocean predominantly at or near the equator, but SST cooling resulting from the forcing only appears initially in a small region south of Java, with no anomalous cooling in the EqIO until several months later (e.g., Saji et al., 1999). Moreover, during weaker pIOD events cool SST anomalies may never expand to the rest of the eastern EqIO (e.g., Du et al., 2012, 2013).

While cooling in the larger eastern EqIO in August–October has been attributed to a variety of mechanisms, including anomalous upwelling/advection and feedbacks with the atmosphere (Murtugudde et al., 2000; Vinayachandran et al., 2002; Du et al., 2008; Halkides and Lee, 2009; Horii et al., 2009, 2013; Wang et al., 2014), less is known about the specific processes for producing the earlier cool SST anomalies

south of Java in May–July. In addition to alongshore wind–induced seasonal SST cooling south of Java in austral winter, a variety of other processes contribute to mixed layer temperature changes in the region and may control the interannual variability of Java SST. Kelvin waves propagating southeastward from the EqIO along the coasts of Sumatra and Java (Figure 4.1) can affect the magnitude of cooling by shoaling or deepening the thermocline (Murtugudde et al., 2000; Sprintall et al., 2000; Vinayachandran et al., 2002), perturbing the 20°C isotherm depth by as much as 50 m along the Java coast (Sprintall et al., 2000). Mesoscale eddies, generated by baroclinic instability between the upwelling region and the South Equatorial Current to the south (Feng and Wijffels, 2002; Yu and Potemra, 2006), may transport warmer surface waters onshore to counter the upwelling-induced cooling (Ogata and Masumoto, 2010). Additionally, the influx of relatively warm water from the Indonesian Seas through Lombok Strait may impact the SST south of Java (Qu et al., 1994; Susanto et al., 2001; Du et al., 2005).

Many of the processes that control Java SST are influenced in turn by the anomalous winds previously linked to pIOD development, but internal ocean anomalies may also affect how SST anomalies manifest, both south of Java and in the larger eastern EqIO. Much of the eastern EqIO has a warm, salinity–stratified barrier layer that separates the cooler thermocline waters from the surface mixed layer (e.g., Sprintall and Tomczak, 1992; Masson et al., 2002); the barrier layer modulates changes in the mixing of heat and momentum that allow SST cooling to spread to the broader eastern EqIO in pIOD years (Masson et al., 2004). Unlike in the broader eastern EqIO (e.g., near Sumatra), seasonal winds south of Java already induce a favorable subsurface stratification for surface cooling; thus coastal Java is uniquely positioned

to produce changes in circulation and feedbacks in the atmosphere that eventually cool SSTs along coastal Sumatra and in the eastern EqIO. Therefore mechanisms that generate anomalous SST cooling south of Java may also be key predictors for the evolution of pIOD events.

In this paper we consider whether local and/or remote (EqIO) winds, by forcing offshore Ekman transport and upwelling Kelvin waves respectively, can explain the initiation and persistence of cool SST anomalies south of Java in pIOD years. To address this question, we identify the locations and characteristics of wind forcing and Kelvin wave activity associated with both strong and weak pIOD events. The emphasis on the role of wind forcing and Kelvin waves in this study is guided by previous work (e.g., Annamalai et al., 2003; Guo et al., 2015) that highlights wind forcing in the evolution of pIOD events. Nonetheless, inflows from Lombok Strait and mesoscale eddies may also be influential, particularly as a negative feedback after anomalous Java SST cooling has been initiated. The paper is organized as follows: Section 4.2 details the datasets that are used in this study. Section 4.3 presents an analysis of the effects of local and remote winds on Java SST anomalies, including a discussion of how the subsurface stratification affects the upper ocean's response to forcing. Section 4.4 focuses on isolating the Kelvin wave signal along the equatorial-coastal waveguide in pIOD years. Section 4.5 compares spatially–averaged predictors that represent the wind, Kelvin wave, and Lombok Strait influences on Java SST and IOD variability, and Section 4.6 considers the implications of these analyses for understanding anomalous Java SST cooling episodes and the evolution of pIOD events.

4.2 Data

4.2.1 Satellite data

In this study we make use of a suite of satellite data consisting of surface wind stress, SST, and sea surface height measurements. High–resolution (0.25° x 0.25°) Cross–Calibrated Multi–Platform (CCMP) 10 meter winds and pseudostresses (wind stresses) from the NASA Jet Propulsion Laboratory (Atlas et al., 2011), with 5–day means in the zonal and meridional directions, were used for the period July 1987–December 2011. The CCMP product is used because it has higher spatial resolution than datasets with more recent coverage (e.g., NCEP/NCAR and ECMWF reanalyses), which is an important consideration when resolving winds near the coast of Java and Lombok Strait.

The optimal interpolation SST product from NOAA (Reynolds et al., 2007; Reynolds, 2009) was used that includes data from the Advanced Very High Resolution Radiometer (AVHRR) on multiple satellites. The AVHRR SST record has daily temporal resolution, 0.25° x 0.25° spatial resolution and spans September 1981–December 2013.

In order to quantify the activity of Kelvin waves, surface sea level anomaly (SLA) (Ducet et al., 2000) was used as a proxy for wave–related displacements of the thermocline, with coverage during the period September 1992–December 2013. We make use of two datasets: (1) the alongtrack delayed–time SLA and (2) gridded delayed–time merged reference maps of SLA, both from Archiving, Validation, and Interpretation of Satellite Oceanographic Data (AVISO). The alongtrack data were used specifically to compute a coefficient representing Kelvin wave activity, as described

in Chapter 3 (Delman et al., 2016a). We use alongtrack SLA to quantify Kelvin wave activity because the higher resolution in the along–track direction (approximately 1/10°, vs. 1/3° for gridded) is advantageous for resolving coastal Kelvin waves, particularly as the radius of deformation shrinks to ∼100 km at 10°S. For coastal Kelvin waves only ascending (SW–NE oriented) tracks are used as these are most nearly perpendicular to the coastline, while for equatorial waves both ascending and descending tracks are used. The gridded maps of SLA were used to compute pressure gradients associated with surface currents in the vicinity of Lombok Strait. The alongtrack and gridded datasets have both been processed to correct for orbital variations, atmospheric distortions, and tidal aliasing; in the alongtrack data a low–pass filter was applied in the alongtrack direction to remove wavelength variations shorter than 65 km (CNES, 2014). The alongtrack dataset has a resolution of ∼10–15 km in the alongtrack direction, with a repeat cycle of approximately 9.9 days; the tracks are spaced up to 3° of longitude apart in near–equatorial regions. The gridded dataset has an approximate spatial resolution of 1/3° x 1/3° in near–equatorial regions, at weekly time intervals. While the quality of both datasets is likely degraded within 10 km of the coast (CNES, 2010), the deformation radius of a mode-1 baroclinic Kelvin wave is over 100 km along the entire Sumatra-Java coastal waveguide; hence most of the cross–shore profile of these Kelvin waves should be well–resolved.

As noted, each of the three satellite datasets cover different time periods; that of the Reynolds SST data is longest (1981–2013) and it encompasses those covered by the CCMP wind product and the AVISO SLA data. When analyses are based on just one dataset (e.g., climatologies and SST–based time series, including the IOD index), the entire time period is used. Correlations between two datasets use the overlapping

period of the two datasets. For the study of Java SST/IOD predictors in Section 4.5, quantities from all three datasets are considered side–by–side; thus the overlapping period 1993–2011 of all three datasets is used to remove seasonal means and normalize by the standard deviation.

4.2.2 In–situ based climatologies

To describe the subsurface stratification along the Kelvin waveguide, we use the World Ocean Atlas 2013 version 2 (WOA13 V2) climatologies of temperature and salinity (Locarnini et al., 2013; Zweng et al., 2013). These data consist of monthly means in bins of size 1/4° x 1/4° in the horizontal and 5 meters in the vertical (for the upper ocean), computed from in-situ measurements during the period 1955–2012. In–situ measurements (particularly of salinity) are sparse and unevenly distributed in the coastal regions near Sumatra and Java, so a spatial filter was applied to smooth the WOA13 V2 climatologies. The spatial filter was an anisotropic Gaussian, with cutoff radii of 3° and 1° in the along–waveguide and across-waveguide directions respectively, and e–folding scales of half the cutoff radii in each direction. The filter also weighted the number of observations for each bin within the cutoff radii. For points along the waveguide where fewer than 10 observations were available within the cutoff radii, or where the Gaussian–weighted position of the observations was offset by more than 0.5° from the original waveguide point, the temperature and salinity values were instead linearly interpolated from points with more observations. The values of temperature and practical salinity were then converted to conservative temperature and absolute salinity using the TEOS–10 Gibbs Sea Water oceanographic toolbox (McDougall and Barker, 2011).

4.2.3 Mixed and barrier layer definitions

One objective of this study is to understand how the thickness of the barrier layer affects the SST response along the Kelvin waveguide, and in particular along the coasts of Sumatra and Java. We define the base of the isothermal layer, and then the base of the mixed layer relative to the isothermal layer following the methodology of Sprintall and Tomczak (1992) and Sprintall and Roemmich (1999). The base of the isothermal layer is defined by the depth at which conservative temperature is $\Delta T_c = 0.2°\mathrm{C}$ below its value at the 10 m reference level (de Boyer Montégut et al., 2004). The mixed layer base is defined as the depth where potential density $\rho_\theta = \alpha\,(\Delta T_c) + \rho_\theta|_{10\,\mathrm{m}}$, with $\rho_\theta|_{10\,\mathrm{m}}$ the potential density at 10 m depth, and α the thermal expansion coefficient $\partial\rho_\theta/\partial T_c$ at 10 m depth. We have used $\Delta T_c = 0.2°\mathrm{C}$ for consistency with our definition of the isothermal layer base. The barrier layer is then given by the difference between the mixed and isothermal layers. It is worth noting that computing the mixed and barrier layer thicknesses based on averaged temperature and salinity fields will yield a somewhat different result than if the thicknesses are computed from individual temperature and salinity profiles prior to averaging. Hence these computations are intended to provide an overview of along–waveguide variations in the barrier layer, rather than accurate representations of the true climatological mixed and barrier layer thicknesses. (Qiu et al. (2012) give more reliable estimates of these thicknesses for the broader EqIO based on individual Argo profiles, though profiles are too sparse to effectively carry out the same analysis along coastal Sumatra and Java.)

4.3 Wind influence on Java SST variability

4.3.1 Regional wind and SST climatologies, and interannual variability

During the mean climatological year, the southeasterly trade wind belt in the subtropical southern Indian Ocean shifts northward in austral fall, reaching its most equatorward position in approximately July–August (Figure 4.2). Upwelling-favorable alongshore wind stress occurs along the Java coast, which causes SSTs near eastern Java to cool from 28–29°C in March–April (Fig. 4.2e) to about 25.5°C in July–August (Fig. 4.2g); they are 2°C cooler than SSTs at the same latitude in the interior of the Indian Ocean. This cooling is also observed to the east of Java along the southern coasts of Nusa Tenggara, but does not extend further northwest along the Sumatra coast (Fig. 4.2g,h). The lack of seasonal cooling along the coast of Sumatra may be attributed in part to weaker alongshore winds (Figure 4.2c,d). Additionally, a thick barrier layer in austral winter (Sprintall and Tomczak, 1992) tends to inhibit SST cooling from any upwelling–favorable wind stress west of Sumatra. The barrier layer in this area results from abundant precipitation near Sumatra exerting a freshening influence on the mixed layer (e.g., Murtugudde and Busalacchi, 1999; Masson et al., 2002).

To assess the overall effects of wind in the region on interannual variability, lagged correlations of box–averaged May–July Java SST anomalies with surface wind anomalies throughout the Indian Ocean region were computed for varying wind orientations and lags (Figure 4.3). Confidence levels for the correlations (shaded in Fig. 4.3) were determined according to the methodology in (Emery and Thomson,

2001), with 24 degrees of freedom; according to the methodology, each 3–month period is one independent realization. The period May–July was chosen to correspond to the season when pIOD–associated Java SST cooling episodes are initiated. SST anomalies south of Java are only weakly related ($|r| < 0.5$) to wind stress anomalies in the same location, regardless of lag (Figure 4.3a). However, Java SST correlations are much more robust ($|r| > 0.7$) with winds south and west of Sumatra. This is especially true for winds in an upwelling–favorable alongshore orientation at or slightly less than the mode–1 baroclinic radius of deformation a from the equator ($a \approx 400$ km) and coast ($a \approx 150$ km at 7°S, at the southern end of Sumatra). The optimum lag of these correlations is with the winds near Sumatra leading Java SST by 10 days (Figure 4.3b), consistent with the approximately 2–3 m s^{-1} phase speed of coastal Kelvin waves in the region (Iskandar et al., 2005; Drushka et al., 2010).

Winds elsewhere in the Indian Ocean region during May–July are also robustly correlated with Java SST (Fig. 4.3). To investigate the possibility that these influences are independent of Sumatra winds, the correlation analysis in Figure 4.3 was repeated with southeasterly winds off Sumatra removed by linear regression from the time series of both Java SST and wind anomalies. As a result, wind anomalies in two other areas also seem to exert a remote influence on SST south of Java (Figure 4.4): (1) a region in the western equatorial Indian Ocean (∼48°–63°E), and (2) on either side of Lombok Strait and Nusa Tenggara. The first area shows a statistically robust correlation between winds in a south–to–southeasterly orientation in the western EqIO and Java SST, with winds leading Java SST by 40–50 days. The zonal wind component of this correlation may represent the influence of Kelvin waves forced by winds in this region; however, no physical mechanism is immediately apparent for meridional winds in the

western EqIO to affect Java SST. When considering individual years (not shown), the meridional component of the wind was not consistently southerly in cool Java SST anomaly years; rather, the correlation was primarily due to the presence of northerly wind anomalies preceding warm Java SST anomalies in May–July.

In the second region, adjacent to Lombok Strait and Nusa Tenggara, wind stress anomalies in a south–southwest orientation are associated with negative SST anomalies south of Java, with the wind leading SST by about 10 days. The near–surface transport through Lombok Strait is known to be sensitive to zonal wind variations in the internal Indonesian seas (Schiller et al., 2010). We suspect that Ekman flow through Lombok Strait may be important in the evolution and particularly the duration of Java SST cooling, as horizontal advection of warmer waters from the strait is a mechanism for the termination of seasonal Java SST cooling (Du et al., 2005). The possible impact of this mechanism during individual years will be discussed in Section 4.5.

4.3.2 Java SST anomalies during pIOD years

Java SST anomalies (apart from the seasonal upwelling, which is forced by local winds) are closely related to the phase of the IOD, and also reflect the considerable variation in the intensity and spatiotemporal extent of pIOD events (e.g., Du et al., 2013; Guo et al., 2015). Every pIOD event observed during the July–December period (when atmosphere–ocean coupling is active in pIOD evolution) is associated with strong cooling south of Java, with Java SST anomalies reaching or surpassing -1σ (Figure 4.5). However, sometimes cooling south of Java is associated with weak pIOD events; these episodes have brief peaks (1–2 months' duration) exceeding 1σ in the Java SST anomaly and IOD index, but the July–December 6–month averages of the

Java SST anomaly and IOD index do not exceed 1σ. (We do not consider events for which the Java SST anomaly or IOD index exceed 1σ only in January–June, as the absence of seasonal trade winds during austral summer and early fall inhibits atmosphere–ocean coupling at the IOD's eastern pole.) In this study, events for which the IOD index exceeds 1σ in the July–December average are "strong" pIOD events, while briefer excursions of the July–December IOD index and Java SST anomaly beyond 1σ which do not meet the strong criterion are "weak" pIOD events. By these criteria, five strong pIOD events (1982, 1994, 1997, 2006, 2012) and five weak pIOD events (1983, 1987, 2003, 2008, 2011) can be found in the satellite SST record; three of each type fall within the 1993–2011 period covered by all three of the satellite datasets (wind stress, SLA, and SST).

We construct composite SST and wind anomalies in the region during the beginning of the three strong pIOD events 1994, 1997, and 2006 (Figure 4.6). Shading in Fig. 4.6 indicates regions in which the SST (Fig. 4.6a,b) and wind speed (Fig. 4.6c,d) values during all three events are at least 0.3 times the composite values, with the same sign (for SST) or direction (for wind). Composite SST anomalies south of Java during strong pIOD years decrease to -1°C or lower between May and July (Figures 4.6a,b) and are mostly confined to the immediate coastal region south of Java. However, the corresponding surface wind anomalies (Figures 4.6c,d) are very weak in the same region south of Java, and not likely to induce the observed anomalous SST cooling. Much greater upwelling-favorable wind anomalies are apparent to the west of Sumatra, extending into the eastern equatorial Indian Ocean.

The lack of influence from local wind anomalies south of Java, also reflected in the wind–SST correlations (Fig. 4.3, 4.4), is surprising given the importance of local

wind forcing in the seasonal SST cooling, and the disconnect between SST anomalies and local wind forcing remains unexplained. One possibility is that upwelling–favorable wind forcing south of Java also tends to coincide with wind forcing of warm surface water through Lombok Strait, neutralizing the effect of wind anomalies south of Java when they are not supported by remote forcing.

4.3.3 Vertical stratification and barrier layers

The pIOD composites in Fig. 4.6 raise the question of why substantial cool SST anomalies do not appear west of Sumatra in the early stages of pIOD events (Fig. 4.6a,b), even though this is where upwelling–favorable wind anomalies are located (Fig. 4.6c,d). One reason for this might be the presence of a deep thermocline and a thick barrier layer west of Sumatra, which must be eroded before upwelling-induced surface cooling can occur (Murtugudde and Busalacchi, 1999; Masson et al., 2004; Qiu et al., 2012). Subsurface climatologies illustrate that the thermocline along the Kelvin waveguide is deepest in the eastern EqIO, with the 20°C isotherm depth greater than 120 m and the 25°C isotherm depth at almost 100 m (Fig. 4.7a). In addition, the near-surface ocean is much fresher near Sumatra and Java than in most of the EqIO (Fig. 4.7b), due to precipitation near Sumatra and outflow from the Indonesian seas on either side of Java. Where the thermocline is deep, this surface cap of relatively fresh water lies above a thick layer of weakly–stratified warm water; thus a barrier layer of 10–30 meters is commonly observed in the eastern EqIO and along coastal Sumatra during May–July (Fig. 4.7a–b). Below the barrier layer in these areas there is a thick layer (up to 40 meters) of only slightly cooler waters with a weak vertical temperature gradient. By contrast, upwelling-favorable seasonal winds near Java raise the 25°C

isotherm to shallower than 50 meters in the May–July climatologies, with SST means approaching 25° in the middle of the upwelling season (Fig. 4.2g). Just south of the eastern side of Java, there is a steep vertical temperature gradient at 20–40 m depth just below a thin seasonal mixed layer and the barrier layer is essentially nonexistent, so cooler waters can be efficiently entrained into the mixed layer.

4.4 Kelvin wave variability and influence on upwelling

Coastal Kelvin waves can induce substantial changes in the subsurface current and temperature structure south of Java, elevating or depressing the thermocline by as much as 50 meters from its mean depth (Sprintall et al., 2000; Susanto et al., 2001; Syamsudin and Kaneko, 2013). Model studies have implicated equatorial–coastal Kelvin waves as a mechanism for inducing SST cooling at the eastern pole of the IOD (Murtugudde et al., 2000; Vinayachandran et al., 2002; Fischer et al., 2005). Here we use satellite observations spanning two decades and covering seven pIOD events to test the hypothesis that Kelvin waves, by enhancing upwelling and shoaling isopycnals in the upper ∼100 meters of the ocean, are necessary to produce anomalous SST cooling south of Java and the subsequent development of pIOD events.

Satellite SLA data (alongtrack and gridded) have previously been used to track the motion of intraseasonal Kelvin waves along the Sumatra–Java coastal waveguide (Syamsudin et al., 2004; Drushka et al., 2010). However, SLA contains a variety of signals (e.g., steric height, Rossby waves, mesoscale eddies) unrelated to the desired Kelvin wave signal. Studies in the equatorial Pacific (e.g., Delcroix et al., 1994;

Boulanger and Menkes, 1995) have used the linear shallow–water theory of Cane and Sarachik (1976, 1981) to decompose zonal current and SLA anomalies into Kelvin and Rossby wave components. Boulanger and Menkes (1995, 1999) projected the theoretical meridional sea level profiles of Kelvin wave and higher-mode Rossby waves onto SLA data to compute coefficients representing Kelvin and Rossby wave activity in the equatorial Pacific; Yuan and Liu (2009) applied this method previously to the equatorial Indian Ocean. We use these prior analyses as our starting point, while recognizing that the exact method of decomposing Kelvin and Rossby waves used by Boulanger and Menkes (1995, 1999) may not be effective for off-equatorial coastal Kelvin waves, due to the differences in structure between equatorial and coastal Kelvin waves. Therefore projections of meridional/cross–shore profiles are followed by projections of harmonic basis functions in the along–waveguide direction and time, with least–squares methods used to separate and remove westward–propagating signals. A detailed description of our method is given in Chapter 3 (Delman et al., 2016a).

The result of our decomposition analysis is a Kelvin wave coefficient K; physically, K represents the displacement of the sea level associated with Kelvin wave activity, integrated across the meridional (cross–shore) profile of the equatorial (coastal) Kelvin wave. Positive K values (elevated sea level) represent downwelling Kelvin waves that deepen the thermocline, and negative K values (depressed sea level) represent upwelling Kelvin waves that shoal the thermocline. We use this quantity as opposed to the wave amplitude; although the latter is directly proportional to K at a given location. The maximum amplitude of Kelvin waves increases as the wave moves poleward along the coast, as the radius of deformation shrinks and the cross–shore profile becomes more exponential. In contrast, the use of K depicts a smoother

transition of wave activity from the equator to the coastal waveguide.

4.4.1 Wind stress and Kelvin coefficient comparison

In the strong pIOD years covered by all three satellite datasets (1994, 1997, 2006), an easterly wind anomaly during April–June (Fig. 4.8a–c) forces or enhances an upwelling Kelvin wave (Fig. 4.8d-f) as indicated by negative K anomalies relative to climatological means. The arrival of this wave along the coast of Java is coincident with a sharp decrease in SST south of Java (to anomaly values $< -1°$C) during May–July (Fig. 4.8g–i). During three weak pIOD years (2003, 2008, 2011), wind stress and K anomalies (Figure 4.9) follow many of the same patterns observed in strong pIOD years; in particular, an easterly wind–forced upwelling Kelvin wave (Fig. 4.9a–b,d–e) induces a sharp decrease in Java SST anomaly in May–July 2003 and 2008 (Fig. 4.9g,h). However, in late austral winter the evolution of the weak pIOD events diverges from the stronger events; during the August–September time frame in 2003 and 2008, a downwelling wave forced by westerly wind anomalies returns the Java SST anomaly to near zero. The year 2011 is somewhat different in that Java SST anomalies never decrease beyond $-1°$C, though the anomalies remain weakly but consistently negative until November (Fig. 4.9i).

The evolution of Java SST during strong vs. weak pIOD years suggests two distinct phases: (1) an "initiation" phase in May–July, during which a sharp Java SST cooling of at least 1°C is necessary for a strong pIOD event to ensue, and (2) a "persistence" phase in August–September, during which an already–established Java cooling can be reversed and weaken the developing pIOD event. The strong pIOD years have predominantly upwelling–favorable winds and Kelvin waves during

both phases. Two of the weak pIOD years have predominantly upwelling–favorable influences during the initiation phase but not in the persistence phase (2003, 2008); in 2011 upwelling Kelvin waves appear to be dominant in the EqIO during both phases, but the wind forcing in the eastern EqIO and along coastal Sumatra oscillates between downwelling– and upwelling–favorable (Fig. 4.9c). As our satellite data only cover 3–4 pIOD events of each type (strong and weak), the distinctions between different types of pIOD years are not statistically robust. Nonetheless, the large seasonal cycle in the tropical Indian Ocean still constrains the time periods when wind forcing can effectively produce Java SST anomalies on the order of 1°C (Susanto et al., 2001).

A closer inspection of the wind stress and K anomalies in Fig. 4.8 and 4.9 reveals that some of the upwelling waves are generated by relatively weak easterly wind anomalies along the waveguide; this includes the upwelling wave in May 1994 that appears to induce Java SST anomalies less than -2°C. To gain some insight into how wind stress forces Kelvin waves, we considered the local forcing of K by the zonal/along–shore wind stress τ^x and its time-derivative $\partial\tau^x/\partial t$. The linear predictive model for upwelling (Gill et al., 1974) suggests that the time-derivative of isopycnal displacement (and therefore of K) is a function of the local wind stress τ^x as well as the horizontal derivative of isopycnal displacement, so according to this model it would be expected that

$$\frac{\partial K}{\partial t} + c\frac{\partial K}{\partial x} \sim \tau^x \tag{4.1}$$

where $c = 2.5$ m s^{-1} is the Kelvin wave phase speed and $\sim$ indicates proportionality in time, for a given location x along the waveguide.

Correlations of the left– and right–hand sides of (4.1) were computed by

averaging each side of (4.1) in bins of size $x_{\text{avg}} = 1111$ km (10° at the equator) and varying bin sizes t_{avg} in time (Figure 4.10a). Partial derivatives are then computed by taking the difference between averaged quantities spaced at intervals of $\Delta x = x_{\text{avg}}$ and $\Delta t = t_{\text{avg}}$ for $\partial/\partial x$ and $\partial/\partial t$ respectively. These correlations show that K is only significantly forced by τ^x for time averages shorter than 20–40 days, depending on the location.

In addition, correlations were also computed between the left–hand side of (4.1) and the Eulerian time derivative of wind stress $\partial\tau^x/\partial t$.

$$\frac{\partial K}{\partial t} + c\frac{\partial K}{\partial x} \sim \frac{\partial \tau^x}{\partial t} \tag{4.2}$$

The forcing of K by $\partial\tau^x/\partial t$ as in (4.2) reflects what might be expected once the isopycnal displacement due to wind forcing has reached a steady state, and the input from the winds is essentially balanced by pressure gradients and currents induced in the ocean. It seems that $\partial\tau^x/\partial t$ is more effective at forcing K than τ^x at all intraseasonal timescales (Figure 4.10b), including the timescales (40–80 day periods, or $t_{\text{avg}} \approx$ 20–40 days) at which Kelvin waves are most commonly observed. The correlations with $\partial\tau^x/\partial t$ also peak with the changes in wind stress slightly leading changes in K (Fig. 4.10c–f), consistent with a causal influence from changes in wind forcing, whereas the correlations with τ^x peak with the Kelvin waves leading the wind stress.

This result suggests that the forcing and propagation of Kelvin waves are more complicated than the simple linear model would suggest, particularly at longer timescales. A forcing of $\partial K/\partial t$ by $\partial\tau^x/\partial t$ suggests that K will tend to vary in phase with τ^x, as is observed; however, it also implies that the largest–magnitude values of K

may not be associated with the strongest wind forcing, but rather with large changes in the wind forcing. Giese and Harrison (1990) suggest some mechanisms to explain why the Kelvin wave propagation might diverge from the Gill et al. (1974) model, such as variations arising from background currents and nonlinearities internal to stronger Kelvin waves. The delayed oscillator effect may also play a role; westerly wind forcing along the equator early in the year (January–March) may generate upwelling Rossby waves that reflect off the boundary and precondition the thermocline for shoaling by directly-forced upwelling Kelvin waves, as in the equatorial Pacific during the decaying phase of El Niño (McPhaden and Yu, 1999). Long wave reflections at the western boundary have been implicated in the termination of pIOD events (e.g., Yuan and Liu, 2009), and some pIOD years (1994, 2006, 2008, 2011; see Fig. 4.8a,c and Fig. 4.9b,c) are preceded by predominantly westerly EqIO wind anomalies in January–March. The western boundary reflection of Rossby waves would be expected to have the most impact on locations near the western boundary and longer timescales; this is indeed observed to some extent (Fig. 4.10b), though this does not completely explain why $\partial\tau^x/\partial t$ is more influential than τ^x at nearly all timescales. Variations in the value of c along the waveguide may also have an effect, as c is affected by the depth of the pycnocline, and some of the wave–associated mass flux is reflected where the value of c changes (e.g., Long and Chang, 1990).

4.4.2 Kelvin wave activity in the initiation and persistence phases

The interannual variability of K along the waveguide during austral fall and winter is related to the phase of the IOD that develops during each year (Figure 4.11).

In April–June (leading the "initiation phase" of Java SST by 1 month), both strong and weak pIOD years had mean negative K anomalies in the EqIO and along the Sumatra–Java coast (Fig. 4.11a). Conversely, most (though not all) years that had consistently negative K anomalies in the EqIO became either a weak or strong pIOD year. It should be noted that there appears to be no clear distinction between the K anomalies of weak and strong pIOD years during this phase. The year 2011 in particular had some of the lowest mean K anomaly values in the EqIO during the period of record, but only weak cooling was observed south of Java (Fig. 4.9i).

In July–August (leading the "persistence phase"), the difference in K anomalies between strong and weak pIOD years becomes more apparent (Fig. 4.11b). Three of the four strong pIOD years (1994, 1997, 2006) also had the most negative K anomalies in the EqIO and along Sumatra during this period. Meanwhile, the two weak pIOD events (2003, 2008) for which anomalous cooling effectively ended during the persistence phase had mean positive K anomalies in the EqIO. The strong pIOD year 2012 managed to attain Java SST anomalies of $-1°$C (Fig. 4.5a) despite only modestly negative EqIO K anomalies in both initiation and persistence phases; though stronger K anomalies were present along coastal Sumatra during the initiation phase (Fig. 4.11b).

The analyses of K suggest the following series of events at the initiation of pIOD events: anomalous easterly wind forcing at the equator induces upwelling Kelvin waves (or strengthens waves that propagate from the western boundary), with frequencies of 40–80 days consistent with forcing by Madden–Julian Oscillation variability. These waves elevate the thermocline along the Kelvin waveguide by 10–30 meters (Vinayachandran et al., 2002; Fischer et al., 2005). This is insufficient

to produce surface cooling initially along the equator and coastal Sumatra, where climatologically there is no substantial vertical temperature gradient in the top 80 meters. However, when these waves reach Java (about 15–40 days after the initial wind forcing), the maximum amplitude of the waves can increase to as much as 50 meters according to mooring data (Sprintall et al., 2000). Moreover, the already shallow seasonal thermocline during May–July allows much cooler water to be entrained into the mixed layer, inducing SST anomalies of –1° to –2°C. The oceanic circulation changes and atmospheric feedbacks resulting from these Java SST anomalies, in combination with ongoing upwelling–favorable forcing in the eastern EqIO, generate the more widespread negative SST anomalies at the IOD's eastern pole during a pIOD event. As stated previously, it seems that most of these processes need to happen in the April–June period at the equator and May–July period south of Java in order for a pIOD event to occur. However, westerly wind forcing and downwelling Kelvin waves generated in July–August (reaching the Java coast during August–September) can change the trajectory of a pIOD event, weakening and terminating it early as in 2003 and 2008 (Fig. 4.9d–e,g–h; Fig. 4.11b).

4.5 Predictability of Java SST and IOD variability from wind stress, Kelvin waves, and Lombok Strait flow

4.5.1 Definition of predictors

Thus far, we have established that remote wind forcing is a primary control on SST anomalies south of Java during the onset of the upwelling season, when pIOD events begin to develop (Fig. 4.3 and 4.4). Upwelling Kelvin waves are likely the primary mechanism for conveying wind forcing along the waveguide during pIOD years, from the EqIO and coastal Sumatra to coastal Java.

To better describe how these mechanisms behave during the onset of pIOD years relative to other years—and hopefully enhance predictability of anomalous Java cooling and the pIOD events that follow—we now define a series of spatially– and temporally–averaged predictors that summarize various influences on Java SST and evolving IOD events (e.g., wind stress, K values, and SSH). (The geographical averaging ranges and lead times to impact Java coastal region for each predictor are given in Table 4.1). All of the predictors are computed so that negative (positive) values of the predictor have a cooling (warming) effect on the Java SST anomaly.

We also define two predictors that are proxies for the pressure–driven near–surface flow through Lombok Strait, computed as the (gridded) SLA differences near the strait in the zonal and meridional directions (Table 4.1), approximating the variability of the geostrophic and direct pressure–driven components respectively. Gridded maps of SLA from AVISO have been used previously as an effective proxy for

variations in Lombok Strait, particularly at monthly and longer timescales (Sprintall and Révelard, 2014). Our proxies are used with the caveat that these represent the flow variations expected near the inflow and outflow regions of the straits, rather than the flow within the strait that can not be directly resolved using AVISO altimetry.

4.5.2 Predictor analysis

Correlations of the influence indicators with Java SST anomaly and −(IOD index) (Figure 4.12) have been computed for both the initiation and persistence phases of Java SST cooling; the sign of the IOD index is reversed to agree with the Java SST anomaly. Predictors with lead times of 10 days were averaged April 21–July 21 (July 22–September 20) for the initiation (persistence) phase, whereas predictors with 30–day lead times were averaged April 1–July 1 (July 2–August 31) for the initiation (persistence) phase. Predictors were also correlated with July–December values of Java SST anomaly and −(IOD index). The latter accounts for influences that may take considerably longer to affect the SST field (e.g., due to a barrier layer inhibiting surface cooling), but that have a robust impact on SST in the period when pIOD events reach their peak.

The initiation phase correlations (Fig. 4.12a) confirm that wind forcing along coastal Sumatra and near Lombok Strait is influential in determining the evolution of Java SST anomalies early in the upwelling season, as shown in Fig. 4.3a. However it is the EqIO K anomaly that has the most robust correlation with July–December −(IOD index). The latter result suggests that distantly–forced equatorial Kelvin waves in April–June may be a consistent predictor of the eastern–pole cooling associated with pIOD events. Though the waves' impact on the eastern EqIO is delayed by

the deep thermocline and the presence of the barrier layer (Fig. 4.7), the changes in horizontal and vertical circulation associated with these waves can ultimately drive the substantial cooling observed throughout the eastern EqIO during strong pIOD events (e.g., Masson et al., 2004; Halkides and Lee, 2009). EqIO wind forcing is not as robust a predictor of the IOD index as the EqIO K anomaly, though the correlation of EqIO wind stress anomaly and July–December $-$(IOD index) is still statistically significant. This implies that the magnitude of the wind forcing in the EqIO does not completely explain the early evolution of pIOD events, and that other aspects of the forcing (e.g., location and phasing with Kelvin waves) should be considered.

The Lombok Strait proxy indicators suggest a potentially statistically significant role in damping anomalous cooling south of Java, by transporting warm surface waters from the Java Sea. However, anomalous pressure gradients associated with upwelling Kelvin waves would induce anomalous southward flows through the strait (e.g., Sprintall et al., 2009). Thus it is not clear from the correlations whether anomalous flows through the strait are a cause or an effect of Java SST anomaly changes.

The persistence phase correlations (Fig. 4.12b) show a similar hierarchy of influences, with the exceptions that Lombok Strait winds no longer significantly affect Java SST, and wind stress anomalies in the EqIO appear to be much more strongly associated with Java cooling and the IOD index than they were earlier in the season. It must be cautioned that EqIO wind anomalies in this phase may be in part a result rather than a cause of cool Java SST anomalies, since Java (and Sumatra) SST anomalies have the potential to influence EqIO winds late in the upwelling season through Bjerknes feedback with the atmosphere.

When considering individual years, the initiation phase EqIO wind stress

anomaly does not predict a clear distinction between cool and warm Java SST anomalies later in the year (Fig. 4.13a), but negative K anomalies do (Fig. 4.13b). Kelvin wave activity is also a better predictor of the IOD index than wind stress (Fig. 4.13c,d); all seven pIOD years have EqIO K anomalies less than -0.5σ; all other years have EqIO K anomalies above this value, though in some cases not by much (Fig. 4.13d).

4.6 Conclusions

The upwelling region south of Java, where cool SST anomalies are a critical precursor to pIOD events, is subject to numerous local and basin–scale forcings from wind stress, planetary waves, and anomalous outflows from the Indonesian Seas. Analyses of remote sensing data show that while local winds drive Java seasonal upwelling, the SST variability related to pIOD events is driven almost exclusively by anomalous forcing further west along the Indian Ocean equatorial–coastal waveguide. This result implies that Kelvin waves are a necessary mechanism for anomalous Java SST cooling to occur. Moreover, due to a barrier layer and deep thermocline in the eastern EqIO and coastal Sumatra, the region south of Java is the first area where upwelling Kelvin waves propagating from the EqIO encounter ideal conditions for entraining cooler water into the mixed layer. A Kelvin wave coefficient K, which quantifies Kelvin wave activity from altimetry data, confirms that Kelvin wave activity is robustly associated with Java SST cooling and the phase of the IOD that subsequently develops (Fig. 4.11, 4.12); individual upwelling Kelvin waves can be directly linked to changes in the Java SST anomaly when these waves reach Java (Fig. 4.8, 4.9). These results are consistent with modeling studies that link Kelvin wave activity to anomalous

cooling in the eastern pole of the IOD (Murtugudde et al., 2000; Vinayachandran et al., 2002; Fischer et al., 2005). However, our results provide observational evidence that Kelvin waves have a direct impact on Java SST anomalies in pIOD years, and that Kelvin wave activity in austral fall (April–June) is a robust predictor of the IOD phase in austral winter and spring (Fig. 4.12a).

The timing of anomalous Java SST cooling suggests two distinct phases in pIOD event evolution: (1) an initiation phase (May–July) when anomalous Java SST cooling must occur in order to allow atmospheric and oceanic feedbacks sufficient time to support a pIOD event, and (2) a persistence phase (August–September) during which a nascent pIOD event may be weakened or terminated before the feedbacks produce substantial cooling west of Sumatra and a strong pIOD event. Only cool Java SST anomalies that persist through the upwelling season are associated with the evolution of strong pIOD events. The ability of Java SST to affect basin–wide SST anomalies is likely also dependent on the subsurface stratification west of Sumatra. During the persistence phase, an already established Java SST cooling can be interrupted by downwelling Kelvin waves (as in 2003 and 2008), which also disrupt the shoaling of the thermocline necessary for SST cooling west of Sumatra. Thus weak pIOD events are distinguished from strong events largely by their early termination; this is generally consistent with studies that have differentiated pIOD events based on the timing of their onset and decay (Du et al., 2013; Deshpande et al., 2014).

Correlations between EqIO wind stress anomalies in the initiation phase and the IOD index later in the year are also lower than correlations with K anomalies in the same location, implying that it is not just the magnitude of zonal wind forcing that determines the strength of upwelling Kelvin waves, Java SST cooling, and pIOD events.

If the wind forcing propagates at a speed not too different from the Kelvin wave phase speed, as has been observed with Madden–Julian Oscillation events in the Pacific (Hendon et al., 1998), then even a smaller–magnitude wind forcing may generate a strong upwelling Kelvin wave. There is some evidence that such a favorable phasing of wind forcing and an upwelling Kelvin wave occurs during the initiation phase of many pIOD events (particularly 1994, 2003, and 2006; compare Fig. 4.8a/d, 4.8c/f, 4.9a/d). Other factors may also have an effect on the strength of developing Kelvin waves: these include the reflection of upwelling Rossby waves at the western boundary, nonlinear modification of Kelvin waves by background currents (e.g., McPhaden et al., 1986) and instability waves, phase speed changes that are internal to stronger Kelvin waves (Giese and Harrison, 1990), and mass fluxes that reflect from the wave due to changes in the thermocline depth (e.g., Long and Chang, 1990).

In addition to the Java upwelling region, the Sumatra coastal region and Lombok Strait are two areas where oceanic processes may have an important effect on developing pIOD events. However, additional in–situ coastal measurements are needed to track changes in subsurface stratification associated with Kelvin waves as pIOD events evolve. A shoaling of the deep thermocline off Sumatra is necessary for the SST cooling west of Sumatra that occurs during strong pIOD events. The erosion of the initially thick barrier layer in this region is driven by the decrease in thermocline depth, rather than the reduction in the surface freshwater flux due to decreased precipitation (Qiu et al., 2012). The thermocline shoaling is in turn the result of horizontal advection and wind–induced upwelling of cooler waters (e.g., Du et al., 2008; Halkides and Lee, 2009; Horii et al., 2013), which may be related to the same upwelling Kelvin waves that produce anomalous cooling south of Java.

The impact of Lombok Strait transport on evolving Java SST anomalies and pIOD events, either directly through transport of warm fresher surface waters or via mesoscale eddies generated near its outflow (Du et al., 2005; Ogata and Masumoto, 2010), is also difficult to quantify relative to other influences. Wind stress anomalies may be an important control on Java SST anomalies during the early part of the upwelling season (Fig. 4.12a), and the near-surface pressure–driven flow through the strait may act as a negative feedback on SST cooling events south of Java. Since the dominant control on upper ocean flow through Lombok Strait is the pressure anomaly south of Java (Sprintall and Révelard, 2014), we consider it likely that the influence of Lombok Strait is to dampen existing Java SST anomalies or restrain their growth. Any clear influence of Lombok Strait flow anomalies on the persistence or termination of pIOD events could only be identified once the causal influence of Java surface cooling on the strait's transport is taken into consideration. Temperature and salinity budgets using ocean models and data assimilation products would be an effective way to quantify the distinct contribution of Lombok Strait variability to temperature and salinity changes in the surface waters south of Java, and will be the subject of future analysis.

4.7 Acknowledgements

Andrew Delman (ASD) was supported by a NASA Earth and Space Science Fellowship, grant number NNX13AM93H. Janet Sprintall (JS) and Julie McClean (JLM) were supported by NASA award number NNX13AO38G. Lynne Talley (LDT), JLM, and ASD were also supported by NSF grant OCE–0927650. The optimal interpolation SST data were produced and distributed through the National Centers

for Environmental Information (NCEI) of NOAA (https://www.ncdc.noaa.gov/oisst). The altimeter products were produced by Ssalto/Duacs and distributed by Aviso, with support from CNES (http://www.aviso.oceanobs.com/duacs/). The World Ocean Atlas 2013 version 2 (WOA13 V2) data were produced and distributed through NCEI (http:// www.nodc.noaa.gov/OC5/woa13/).

Chapter 4, in full, consists of material that is in revision for publication in the Journal of Geophysical Research: Oceans, by Delman, A. S., Sprintall, J., McClean, J. L., and L. D. Talley. I was the primary investigator and author of this paper; the co-authors supervised and assisted with the preparation of the manuscript.

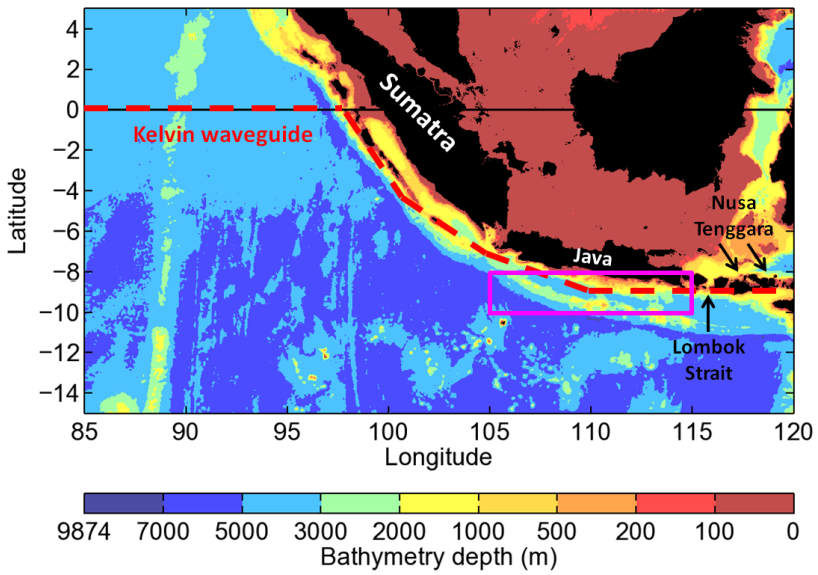

Figure 4.1: Map of the region around the eastern pole of the IOD, indicating the locations of the waveguide, islands, Lombok Strait, and the region averaged for the Java SST anomaly index (magenta box).

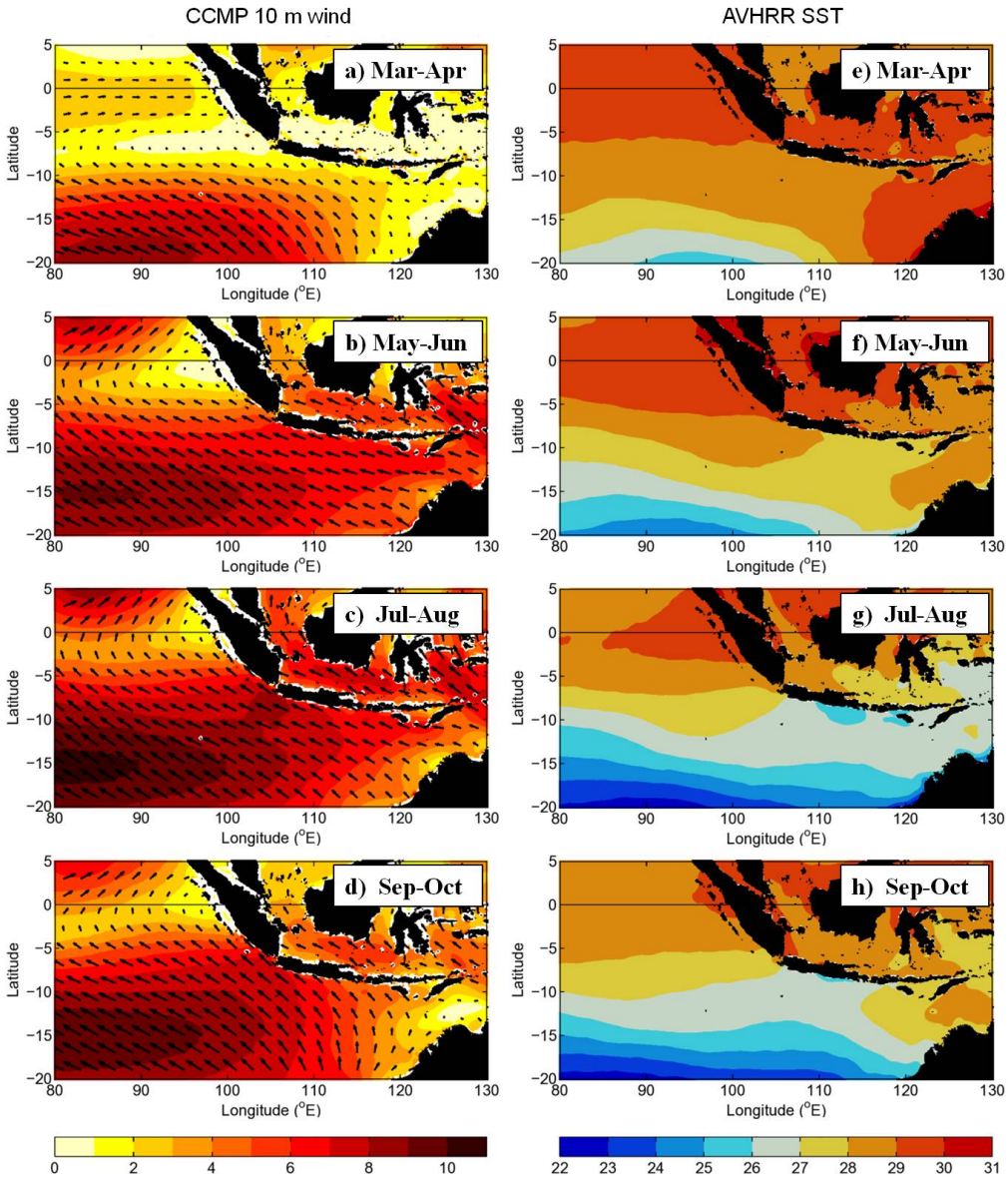

Figure 4.2: (a)–(d) 1988–2011 climatological means of CCMP 10 m wind vectors (m s^{-1}) and wind speed (color shading); and (e)–(h) 1982–2013 climatological means of AVHRR SST (°C) in the southeastern tropical Indian Ocean during the month ranges indicated.

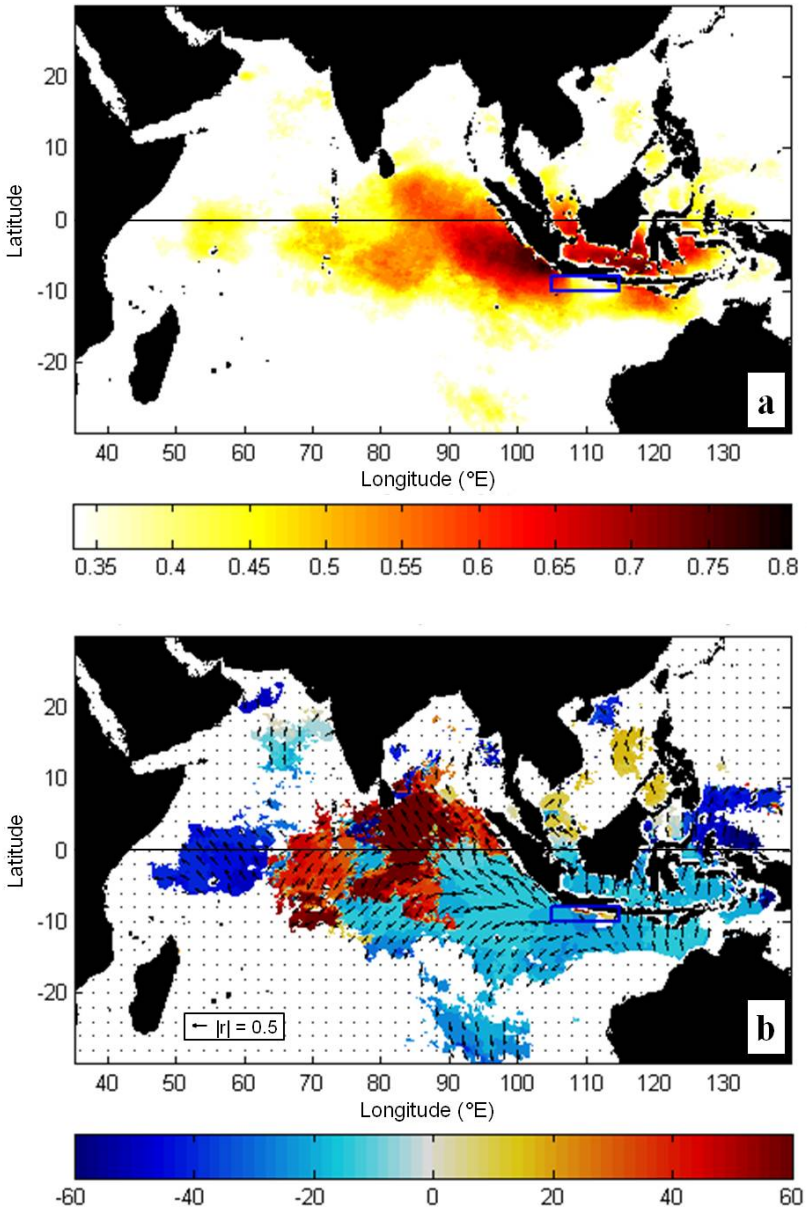

Figure 4.3: (a) Magnitude and (b) lag (days) and wind orientation, of maximum correlation coefficient $|r|$ of CCMP wind stress anomalies with SST anomaly in box south of Java (blue), May–July. Negative (positive) lags indicate the wind leading (lagging) the SST. Directional arrows in (b) have lengths proportional to the correlation coefficient in (a), with the scale arrow in the lower–left corner of (b) indicating the length of an arrow for $|r| = 0.5$. Only >95% confidence correlations are shaded.

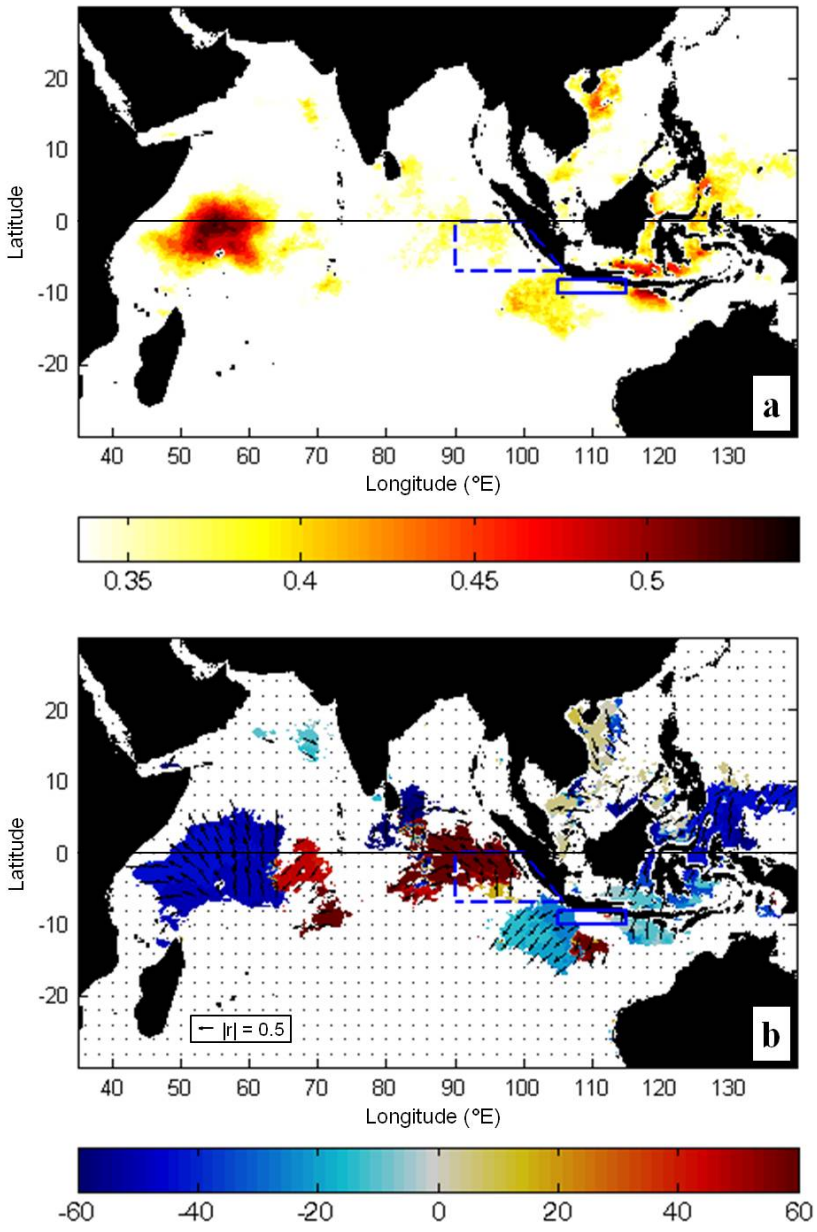

Figure 4.4: Same as Figure 4.3a–b, except that a linear regression of the NW–SE oriented (upwelling–favorable) wind stress anomalies averaged west of Sumatra (in region outlined by dashed blue lines) has been removed. Only >95% confidence correlations are shaded.

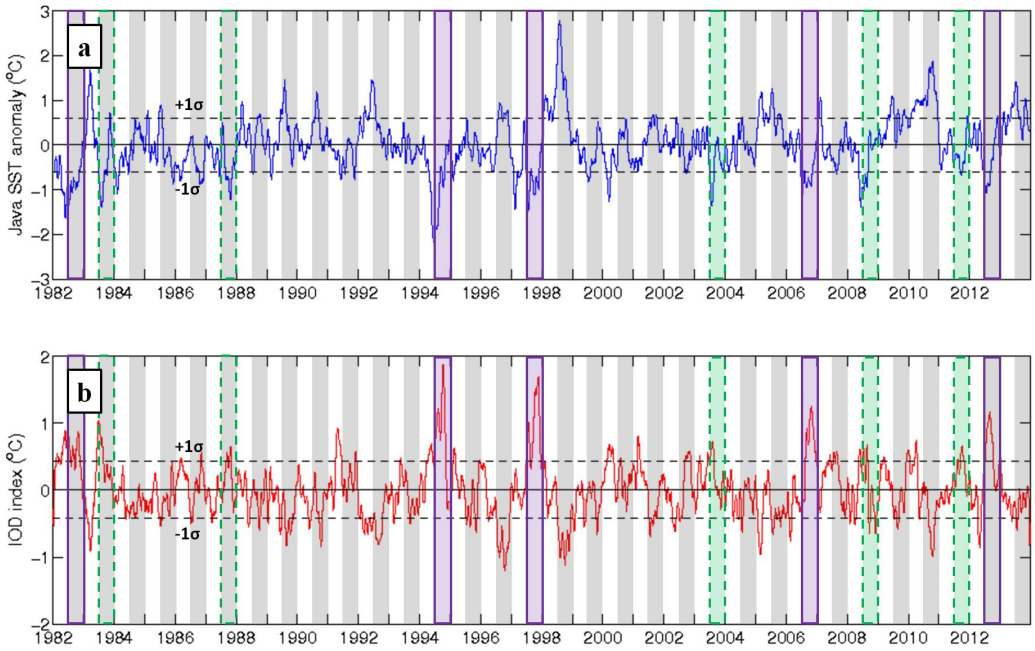

Figure 4.5: (a) Time series of AVHRR SST anomalies averaged in a box south of Java (see Figure 4.1), smoothed using a 30–day moving average. (b) Time series of the Indian Ocean Dipole mode index as defined by Saji et al. (1999), derived from AVHRR SST. Horizontal dashed lines in both plots indicate 1 standard deviation σ from the mean, while shading indicates the July–December period used to define pIOD events. Purple outlines indicate "strong" pIOD events, while the green dashed outline indicates "weak" pIOD events; the three events of each type that fall within the coverage period of all satellite datasets (1993–2011) are also shaded in color.

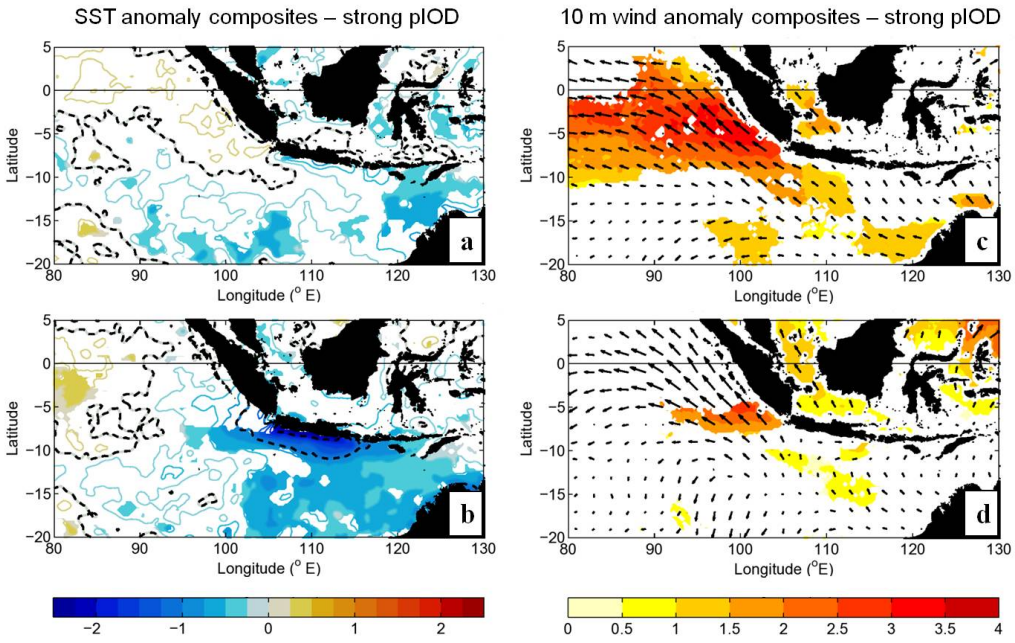

Figure 4.6: (a) Composite SST anomalies (color contours, and shading) from three strong pIOD years during the months when anomalous Java SST cooling started (May 1994, June 1997, June 2006). The contour interval is 0.25°C, and contours with black dashes indicate intervals of 1°C. (b) Same as (a), but for the months when anomalous Java SST cooling reached its peak magnitude (June 1994, July 1997, July 2006). (c) Composite 10 m wind velocity anomaly vectors during the same months as in (a). Shading indicates the magnitude of the composite wind anomaly (m s^{-1}). (d) Same as (c), but for the same months as in (b), when Java SST cooling reaches its peak magnitude.

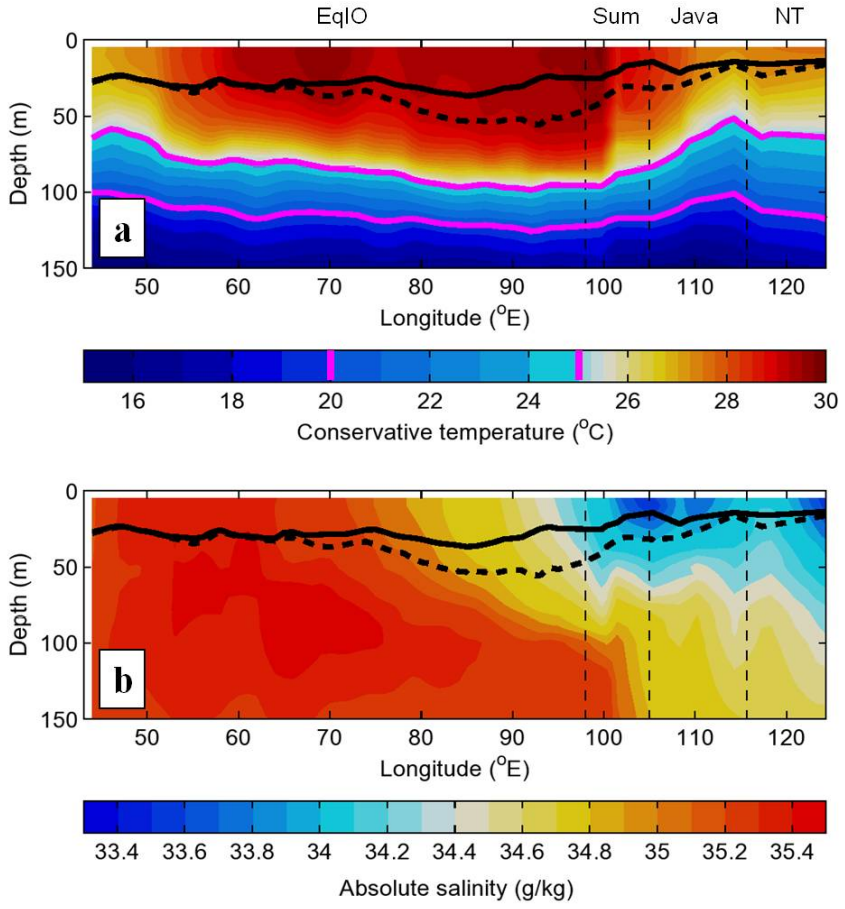

Figure 4.7: (a) May–July conservative temperature climatology and (b) absolute salinity climatology along the IO Kelvin waveguide (see Fig. 4.1), from WOA13 V2. The thin vertical dashed lines indicate the approximate longitudes of transition between equatorial–coastal Sumatra (98°E), coastal Sumatra–Java (105°E), and Lombok Strait (115.65°E). The locations of the equatorial IO (EqIO) and coastal Sumatra (Sum), Java, and Nusa Tenggara (NT) are indicated at the top. The magenta lines in (a) indicate the 20°C and 25°C isotherms. Thick solid (dashed) lines in both panels indicate the base of the mixed (isothermal) layers respectively; the layer between the two lines is the barrier layer.

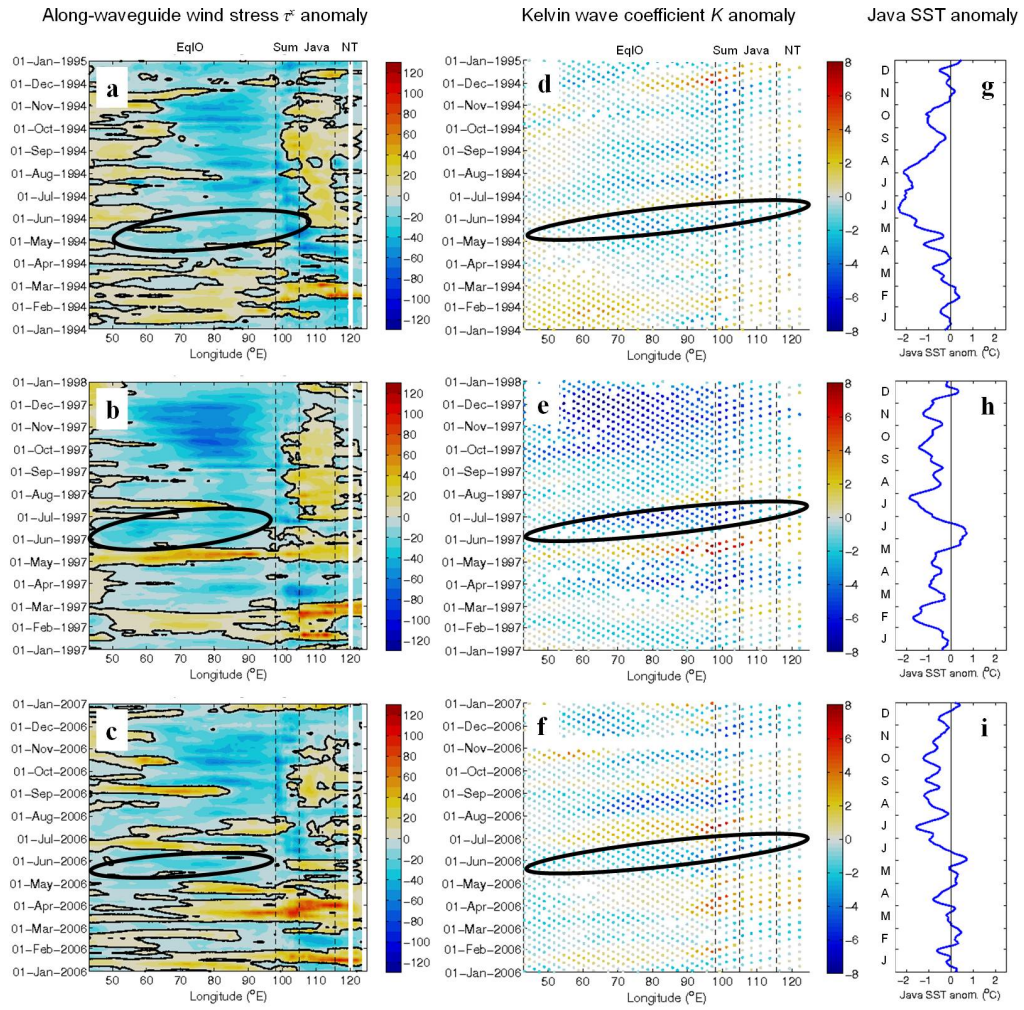

Figure 4.8: (a)–(c) Wind pseudostress anomaly (m^2 s^{-2}), oriented along the Indian Ocean–Indonesian waveguide, plotted for the three strong pIOD years (a) 1994, (b) 1997, and (c) 2006. Positive (negative) values indicate westerly/downwelling (easterly/upwelling)-favorable wind stress. The thick contour indicates zero wind stress. (d)–(f) Kelvin wave coefficient K anomaly for the same three years as in (a)–(c) respectively, with units of 10^4 m^2. Positive (negative) values represent downwelling (upwelling) Kelvin waves. The ellipses in (a-f) indicate wind stresses forcing upwelling Kelvin waves that initiate anomalous Java SST cooling. (g)–(i) SST anomalies south of Java (averaged 10°–8°S, 105°–115°E), smoothed using a 10–day moving average, for the same three years as in (a)–(c).

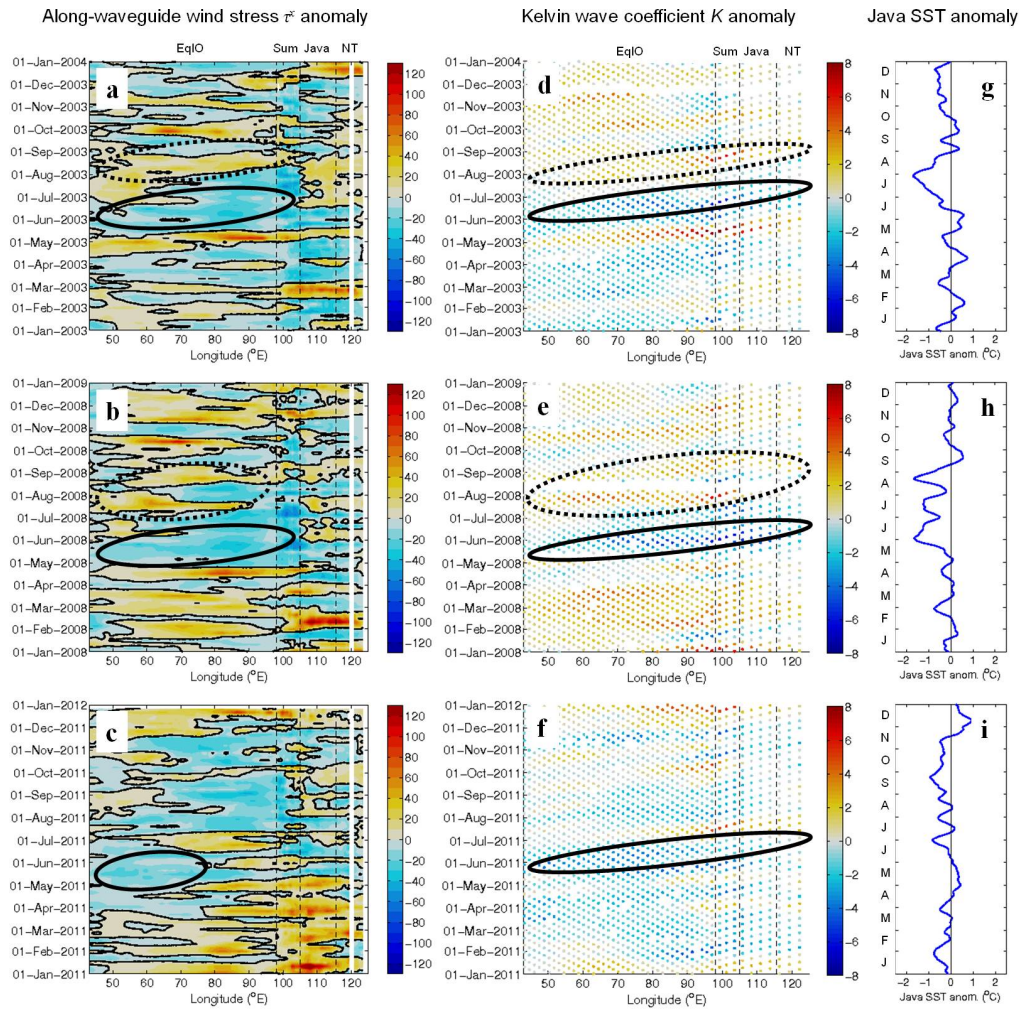

Figure 4.9: Same as Figure 4.8, but for the three weak pIOD years 2003, 2008, and 2011. The solid ellipses indicate wind stresses and Kelvin waves associated with the initiation of anomalous Java SST cooling as in Fig. 4.8, while the dotted ellipses (for 2003 and 2008) indicate wind stresses and Kelvin waves associated with the termination of cooling.

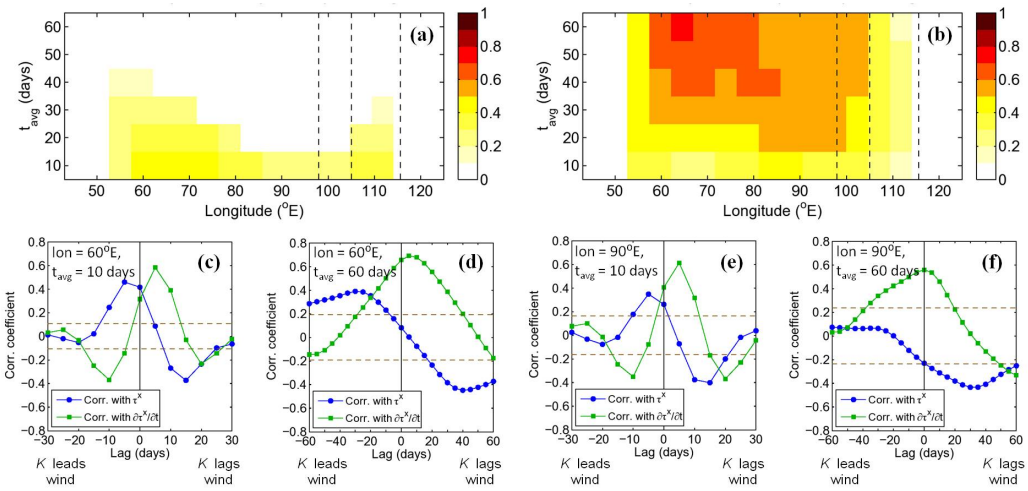

Figure 4.10: (a) Correlation of zonal/along-waveguide wind stress τ^x with $\partial K/\partial t + c(\partial K/\partial x)$ at zero lag, for various points along the waveguide and time-averaging ranges t_{avg}. Only values that exceed the 95% confidence threshold for significance of the correlations are shaded. (b) Same as (a), but for the correlation of $\partial\tau^x/\partial t$ with $\partial K/\partial t + c(\partial K/\partial x)$ at zero lag. (c-d) Lagged correlations of $\partial K/\partial t + c(\partial K/\partial x)$ with τ^x and $\partial\tau^x/\partial t$ centered in the western (60°E) EqIO, with averaging periods of $t_{\text{avg}} = 10$ and 60 days respectively. (e-f) Same as (c-d), but centered in the eastern (90°E) EqIO. The horizontal dashed lines indicate the 95% confidence thresholds for the correlations.

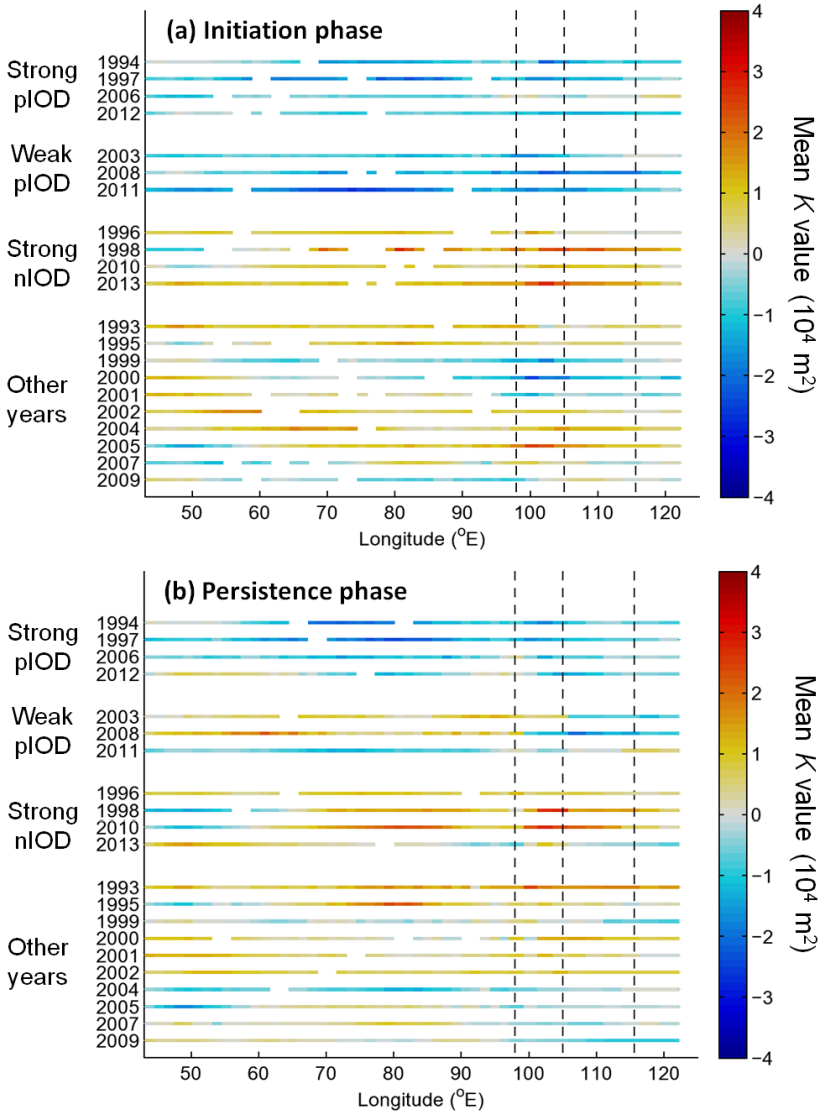

Figure 4.11: (a) Mean Kelvin wave coefficients K during April–June (i.e., "initiation phase" minus 1 month lead time) of each calendar year in the range 1993–2013, plotted as a function of longitude and phase of the IOD. (b) Same as (a), but for mean values of K during July–August ("persistence phase" minus 1 month lead time) of each calendar year, as a function of longitude.

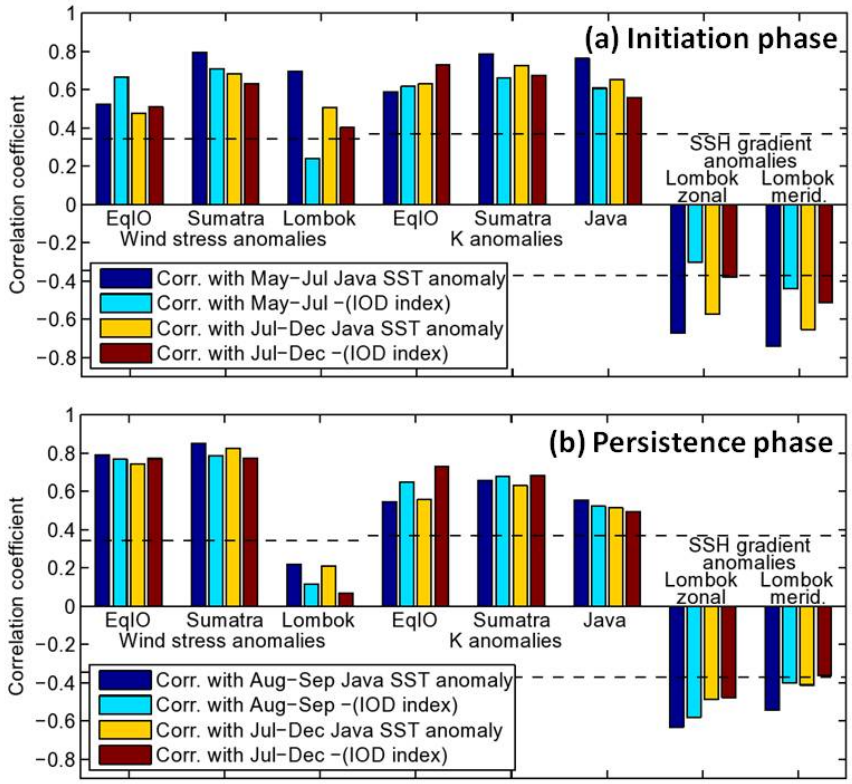

Figure 4.12: Correlations of the predictors described in Table 4.1 with the Java SST anomaly and −(IOD index). (a) Correlations of the initiation phase predictors (averaged for May–July minus lead times specified in Table 4.1), with the Java SST anomaly and −(IOD index) for both May–July and July–December. The dashed horizontal lines indicate 95% confidence levels for the significance of the correlations. (b) Same as (a), but for the persistence phase (August–September minus lead times) predictors.

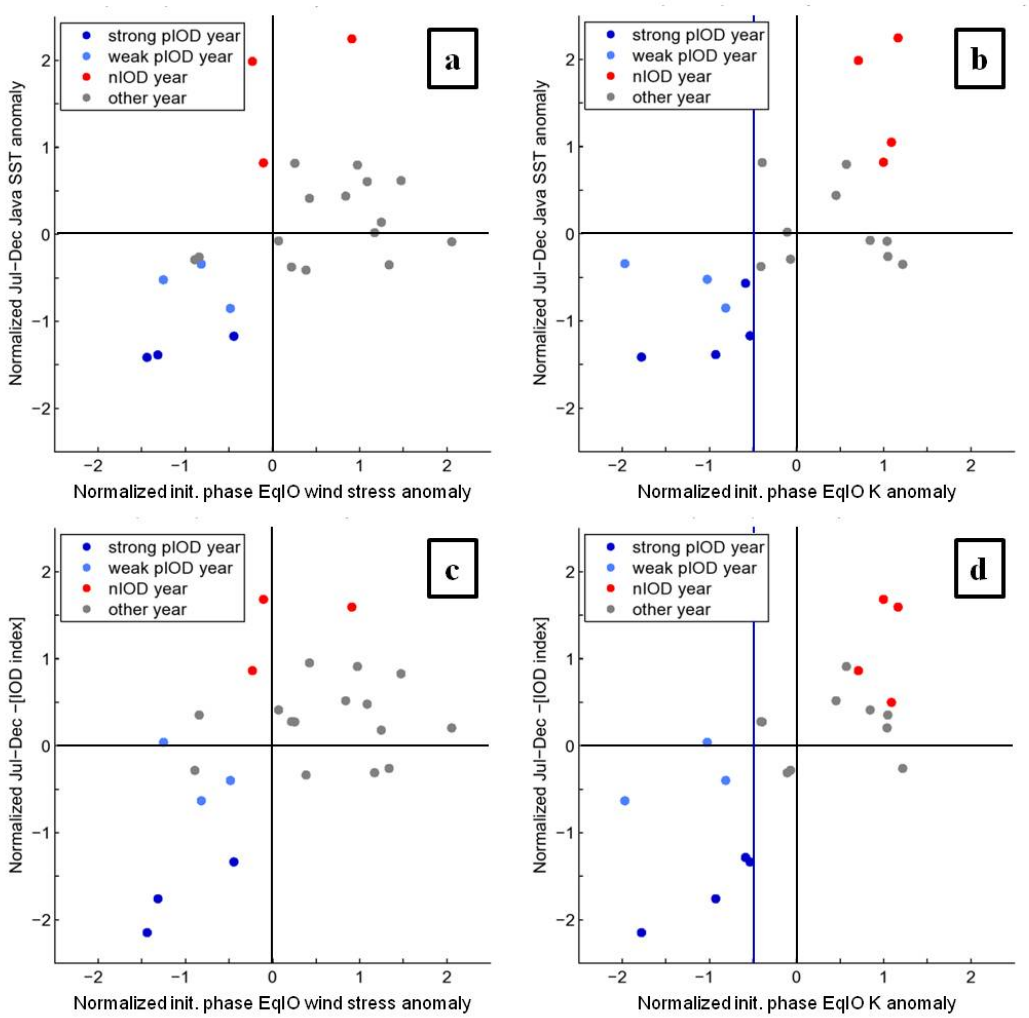

Figure 4.13: (a) Normalized EqIO wind stress anomaly predictor for the initiation phase (April 1–July 1), and the July–December Java SST anomaly. Color shading indicates the phase of the IOD. Both the predictor and the SST anomaly have been normalized by their standard deviations for 1993–2011. (b) Same as (a) but for values of the EqIO K anomaly predictor. The vertical blue line indicates the -0.5σ value of K. (c,d) Same as (a,b) respectively, but plotted with $-$(IOD index) on the y–axis, normalized by its standard deviation for 1993–2011.

Table 4.1: Description of the geographic (spatial) and lead time averaging used to define the indices and predictors in Figures 4.12 and 4.13. The IOD index is computed using the method defined by Saji et al. (1999). The wind stress orientation corresponds to the wind stress direction of negative values of the index; e.g., a wind stress orientation of 90° (E) indicates that easterly winds are averaged and correlated with cool Java SST anomalies.

Averaging quantity	Region	Geographic range for averaging	Wind stress orientation (of negative values)	Lead time for averaging
IOD index and Java SST anomaly				
SST anomalies	IOD index	(50°E ≤ lon ≤ 70°E, 10°S ≤ lat ≤ 10°N) − (90°E ≤ lon ≤ 110°E, 10°S ≤ lat ≤ 0°)		0 days
	Java SST	105°E ≤ lon ≤ 115°E, 10°S ≤ lat ≤ 8°S		0 days
Predictors				
Wind stress anomalies	EqIO	50°E ≤ lon ≤ 90°E, 5°S ≤ lat ≤ 5°N	90° (E)	30 days
	Sumatra	90°E≤lon < Sumatra coast, 7°S≤lat≤0°	135° (SE)	10 days
	Lombok	115°E ≤ lon ≤ 120°E, 10°S ≤ lat ≤ 6°S	210° (SSW)	10 days
Kelvin coeff. K anomalies	EqIO	50°E ≤ lon ≤ 90°E		30 days
	Sumatra	98°E ≤ lon ≤ 105°E		10 days
	Java	105°E ≤ lon ≤ 115°E		0 days
SSH gradient anomalies	Lombok zonal	(116°E < lon≤117°E, 10°S < lat≤7°S) − (114.5°E < lon≤115.5°E, 10°S < lat≤7°S)		10 days
	Lombok merid.	(114.5°E < lon≤117.2°E, 8°S < lat≤7°S) − (114.5°E < lon≤117.2°E, 10°S < lat≤9°S)		10 days

Chapter 5

Process-specific contributions to anomalous Java mixed layer cooling during positive IOD events

Abstract

The seasonal upwelling region along the south coast of Java is the first area to exhibit negative SST anomalies associated with positive Indian Ocean Dipole (pIOD) events; this anomalous cooling may be influenced by a variety of phenomena that traverse the region. In order to estimate the relative impacts of local wind stress, coastal Kelvin waves, and mesoscale eddies on the evolution of anomalous SSTs, a temperature budget is computed from the output of a strongly eddy-active ocean general circulation model simulation. The dominant contributions to the seasonal cycle cooling during May-July (the onset period of both seasonal and anomalous pIOD cooling) are from a reduction in incoming shortwave radiation and from vertical mixing,

consistent with earlier studies in the region; however, the model output also resolves an advective contribution not identified in the earlier work. Composite temperature budget anomalies for pIOD years identify advection as the mechanism for the initial pIOD-associated cooling. In order to understand which process(es) are responsible for the anomalous advective cooling, a regression methodology is employed to quantify the advective contributions from anomalous velocities and temperatures associated with specific processes. Using this method, local wind stress forcing and Kelvin waves are found to have comparable contributions to anomalous cooling, while mesoscale eddies have a very modest warming effect on the eastern side of the upwelling region. The attribution of a substantial part of the cooling to local wind stress appears to be inconsistent with earlier work showing a lack of robust correlations between local wind stress and Java SST. This discrepancy may be due to errors in wind stress observations near the coast, differences between observations and the wind stress product used to force the model, or the possibility that Kelvin waves contribute more to cooling by enhancing favorable conditions for turbulent vertical mixing.

5.1 Introduction

The waters along the south coast of Java experience seasonal upwelling and surface cooling during austral winter (e.g., Wyrtki, 1962; Susanto et al., 2001). This cooled water contrasts with the warm tropical waters of the Indian Ocean to the west and the Java Sea to the north, as well as with the relatively warm waters of the Indonesian Throughflow flowing out from Lombok Strait to the east. While the seasonal upwelling is driven largely by upwelling–favorable southeasterly trade winds (Susanto et al., 2001), the intensity of the cooling varies on interannual timescales

and is thought to play a role in the initiation of positive Indian Ocean Dipole (IOD) events (e.g., Saji et al., 1999; Xiang et al., 2011). The elevated interannual variability of sea surface temperatures (SSTs) associated with the eastern pole of the IOD first appears off the coast of Java in June-July (Susanto et al., 2001; Xie et al., 2002), from where it spreads to the west of Sumatra; this variability can mostly be attributed to SST cooling episodes that begin south of Java, at the onset of positive IOD (pIOD) events (e.g., Saji et al., 1999; Du et al., 2012). However, few studies have focused on the specific mechanisms for producing anomalous cooling south of Java. An analysis by Meyers (1996) suggested that thermocline depth and SST anomalies near the coast of Java might be forced remotely by zonal wind stress in the equatorial Indian Ocean. More recent work (Chen et al., 2015; Delman et al., 2016b) indicates that SST anomalies near Java are very weakly correlated with local wind stress anomalies; much more robust correlations are found with wind stress anomalies in the equatorial Indian Ocean. When bandpass filtering for intraseasonal timescales, Chen et al. (2015) found a particularly strong correlation between equatorial wind stress anomalies and thermocline depth anomalies along coastal Java/Sumatra at 10–20 day lags, a timescale consistent with the propagation of Kelvin waves from the equatorial Indian Ocean along the Sumatra waveguide to the Java coast.

Given the implications of Java and Sumatra upwelling for regional climate, the area has been a focus of numerous upper ocean and mixed layer temperature budget studies derived from observations (Horii et al., 2009, 2013), ocean general circulation models (OGCMs; Vinayachandran et al., 2002; Wang et al., 2014), and data assimilation reanalysis products (Du et al., 2008; Halkides and Lee, 2009). These previous analyses have identified some combination of vertical entrainment,

horizontal advection, and surface latent heat loss as the drivers of anomalous cooling. However, some of these analyses have focused on the broader eastern pole of the IOD (Vinayachandran et al., 2002; Wang et al., 2014), or observations at a mooring well west of Java (Horii et al., 2009, 2013). While these other regions in the IOD's eastern pole do ultimately experience cooling during pIOD events, the seasonal shoaling of the thermocline and coolest SST anomalies are concentrated within ∼200 km of the coast of Java during the earliest months of the events (Saji et al., 1999; Delman et al., 2016b).

Du et al. (2008) looked specifically at the budget south of Java using the Simple Ocean Data Assimilation (SODA) product, which was run with 0.4° x 0.25° horizontal resolution and remapped onto a 0.5° x 0.5° grid, and found the net surface heat flux (presumably from latent heat loss) and vertical entrainment to be the most consistent cooling influences in composites of pIOD years. Based on comparisons to time series of local wind stress and zonal current anomalies, they attributed the anomalous cooling mostly to local winds, with some remote influences at times when wind stress anomalies could not explain zonal current anomalies. However, the attribution of cooling largely to surface fluxes is inconsistent with the weak correlations to local wind stress (Chen et al., 2015; Delman et al., 2016b). Halkides and Lee (2009) used the Estimating the Circulation and Climate of the Ocean (ECCO) data assimilation product with 1° zonal x 0.3° meridional resolution (within 10° of the equator), to average the temperature budget in a larger horizontal box including coastal areas of Sumatra as well as Java. They examined both the seasonal cycle of the budget and the anomaly budget during specific pIOD years; seasonal cooling was driven by surface fluxes and subgrid–scale vertical mixing, but in the anomaly budget vertical

advection became the dominant term producing cooling, with additional contributions from vertical mixing and meridional horizontal advection. The discrepancy between the results from SODA and ECCO may be the result of differences in the time range spanned by the simulations or the grid resolutions; if the latter plays a role, then a higher-resolution model or reanalysis product that resolves coastally–trapped planetary waves and upwelling should present a clearer picture of the dynamical contributions to temperature changes in the region.

Advective and vertical mixing contributions to the temperature budget may be the result of a number of processes that affect mesoscale dynamics in the region south of Java. Intraseasonal Kelvin waves with periods ranging from 20–70 days in austral winter (e.g., Iskandar et al., 2005; Drushka et al., 2010; Iskandar et al., 2014) propagate from the equatorial Indian Ocean, driven mostly by equatorial zonal wind stress. Upwelling Kelvin waves that are generated along the equator in approximately April-June encounter a deep thermocline and a salinity-stratified barrier layer near Sumatra, inhibiting cooling west of Sumatra, but can produce cooling when reaching the shallower thermocline along the Java coast during May-July (Delman et al., 2016b). Moreover, the prevalence of upwelling Kelvin waves during the early part of the Java upwelling season is a robust predictor of anomalous Java cooling and the development of pIOD events in the latter half of the calendar year (Delman et al., 2016b). This suggests that coastal Kelvin waves might produce surface mixed layer cooling anomalies in the Java temperature budget by changes to horizontal and vertical advection, and possibly also by altering the background stratification that controls vertical mixing. Mesoscale eddies generated in the South Equatorial Current (SEC) south of the Lombok Strait outflow (e.g., Feng and Wijffels, 2002; Yu and Potemra,

2006) have been implicated as a possible warming influence to counter the development of anomalous cooling. Ogata and Masumoto (2010) in particular found that advection by intraseasonal velocity and temperature anomalies produced a net warming in the region during the 1994 pIOD event, though their budget was averaged over a much larger spatial domain and did not specifically associate the intraseasonal anomalies with mesoscale eddies (vs. intraseasonal planetary waves, for example).

Hence local wind stress, Kelvin waves, and mesoscale eddies all may influence surface mixed layer temperature changes in this region, but aside from the Ogata and Masumoto (2010) study of mesoscale eddies, previous temperature budget analyses have not attempted to quantify the contribution from each process. Many of the model simulations and data assimilation products used in these earlier analyses were only marginally able to resolve the cross-shelf structure of coastal Kelvin waves and mesoscale eddies, which both have length scales in this region of approximately 100 km. However, a recent global OGCM simulation (Johnson et al., 2016) at approximately 10 km (0.1°) horizontal resolution has all of the terms archived that are needed to close the temperature budget, providing us with the opportunity to isolate the specific contributions of these processes to a critical phase in the development of pIOD events.

This study focuses specifically on the temperature budget in the region south of Java, using 31 years of strongly eddy–active ocean general circulation model output containing 8 pIOD events to elucidate the roles of local wind stress, coastal Kelvin waves, and mesoscale eddies in pIOD event evolution. Our hypothesis, based on previous work highlighting the importance of remote forcing (Chen et al., 2015; Delman et al., 2016b) and mesoscale eddies (Ogata and Masumoto, 2010), is that the local response to the passage of Kelvin waves produces more anomalous cooling

than local wind stress during pIOD years, and that mesoscale eddies flux warmer waters onshore to counter some of this cooling. In order to highlight the impacts that produce cool Java SST anomalies during pIOD years, which peak in July-August, we consider the contributions to the temperature tendency during the months May-July as the cooling develops. The paper is organized as follows: Section 2 details the characteristics of the model simulation and remote sensing observations used, along with comparisons of the model's surface state to observations during pIOD years. Section 3 discusses the form of the temperature budget applied to the model simulation output in this analysis. Section 4 focuses on the box–averaged temperature budget south of Java, summarizing the seasonal cycle and the composite anomalies associated with pIOD events, and presenting comparisons to prior budget studies. Section 5 illustrates the spatial distribution of the seasonal cycle and composite pIOD anomalies using regional horizontal maps of the budget terms. Section 6 employs a decomposition of the advective term in the temperature budget into contributions from wind stress, Kelvin waves, and mesoscale eddies, presenting their effect on the mapped composite temperature budget. Finally, Section 7 discusses the implications of these results and relates them to earlier statistical studies of observations and models in the region.

5.2 Analysis tools

5.2.1 Model description

The temperature budget analysis in this study was computed using output from an atmospheric reanalysis-forced simulation of the Parallel Ocean Program (POP; Smith and Gent, 2002; Smith et al., 2010) version 2, the ocean component of the

Community Earth System Model (CESM). The configuration and physics of the POP run is described in more detail in Johnson et al. (2016), so we will only discuss some attributes most relevant to our budget analysis here. The POP model was coupled to the ice model component of CESM, the Community Ice CodE (CICE; Hunke and Dukowicz, 1997; Hunke and Lipscomb, 2010) version 4, in the CESM framework. It was configured on a global tripole grid (Murray, 1996), with two north poles over North America and Asia (Smith et al., 2010). The model was run with an eddy–active horizontal resolution of approximately 0.1° in the tropics, and 62 vertical levels with 10 meter spacing at depths shallower than 160 meters; topography was represented with partial steps (Adcroft et al., 1997), so that many cells adjacent to topography were discretized as partial bottom cells (Smith et al., 2010). Density and other thermodynamic properties were computed using the equation of state in McDougall et al. (2003). Diabatic vertical mixing and convection (the latter is nonzero only for unstable density profiles in the surface boundary layer) were computed implicitly using the K–profile parametrization (KPP) of Large et al. (1994). Horizontal viscosity and diffusivity were computed using biharmonic operators (Smith et al., 2010), with biharmonic viscosity and diffusivity values that are proportional to the cube of the local grid spacing. For this run, equatorial values of biharmonic viscosity and diffusivity were set at $\nu_0 = -2.7 \times 10^{10}\,\mathrm{m^4\,s^{-1}}$ and $\kappa_0 = -3 \times 10^{9}\,\mathrm{m^4\,s^{-1}}$ respectively (Bryan and Bachman, 2015).

The coupled POP/CICE run was forced at the surface with the Coordinated Ocean–Ice Reference Experiments (CORE) dataset (Large and Yeager, 2004, 2009). Version 2 of this dataset (CORE.v2) has merged atmospheric reanalysis and remote sensing products to create two products: (1) a "normal year" forcing product (CORE–

NYF.v2) consisting of a single year climatological cycle with added stochastic synoptic–scale forcing, and (2) an interannually–varying forcing product (CORE–IAF.v2) representing the years 1948–2009 (Large and Yeager, 2009; Griffies et al., 2012). The simulation used here was initialized at rest from the World Ocean Circulation Experiment (WOCE) global hydrographic climatologies of temperature and salinity (Gouretski and Koltermann, 2004), and run with CORE–NYF.v2 forcing for 15 years (Bryan and Bachman, 2015). The simulation was then run with interannually–varying CORE–IAF.v2 forcing representing the years 1977–2009 (Johnson et al., 2016). During the interannually–forced portion of the run 5–day averages of state variables and all of the terms that contribute to the temperature, salinity, and momentum tendencies were archived. Due to the abrupt shift from normal–year to interannually–varying forcing, the first two years of the interannually-varying portion of the run are regarded as a transition period and are not used in the budget analysis. Instead, as in Johnson et al. (2016), we use the output representing the years 1979–2009; the beginning of this time period also corresponds to the start of the earliest remote sensing datasets that contribute to the CORE forcing products. Most of our analysis will be focused on years that contain pIOD events, which for the purposes of our study are years in which the Java SST anomaly decreased to -1°C or lower at some time during the upwelling season of May-October. According to this criterion, 8 pIOD years occurred in the 31 years of model output (1982, 1983, 1994, 1997, 2003, 2006, 2007, 2008); though the actual timing of cooling onset varies, the period of cooling development in each year overlaps with at least some part of May-July.

5.2.2 Remotely-sensed data

To obtain an estimate of how accurately the model represents the state of the near–surface ocean, two remote sensing observational datasets were used for comparison with the model run.

The first of these datasets is the optimal interpolation SST product from NOAA (Reynolds et al., 2007; Reynolds, 2009), with temperature data collected from the Advanced Very High Resolution Radiometer (AVHRR) mounted on multiple satellites. The AVHRR SST data has been gridded with 0.25° x 0.25° spatial resolution and daily temporal resolution; the dataset begins in September 1981 and spans all 8 pIOD years considered in the model budget analysis.

The second dataset consists of gridded maps of absolute dynamic topography (MADT) from Archiving, Validation, and Interpretation of Satellite Oceanographic data (AVISO) (Ducet et al., 2000). The AVISO MADT data have a spatial resolution of 1/3° x 1/3° and daily temporal resolution, starting in January 1993. Therefore, the AVISO MADT record spans 6 of the 8 pIOD years considered in our analysis. In comparisons of AVISO MADT with the model sea surface height (SSH), the mean of each dataset across the entire spatial and temporal domain is removed. The means are removed so that the differences in the datasets reflect the spatial and temporal variability of SSH gradients that represent current flows, rather than biases in the absolute values of SSH relative to the geoid that are dynamically unimportant.

5.2.3 Comparison of the model's surface state to remote sensing observations

The Java upwelling region is subject to numerous types of dynamics that affect the regional ocean's mean state (e.g., currents and strait flows) and its variability (e.g., Kelvin waves and mesoscale eddies), which must be simulated with some degree of accuracy for the model budgets to be representative of the actual ocean. Seasonally, the area of cool SSTs associated with the upwelling is bounded by two straits transporting warmer waters from the interior Indonesian seas (Figure 5.1). These two straits—Lombok Strait and Sunda Strait—also provide approximate boundaries for the extent of the coolest SST anomalies during pIOD years (Figure 5.2). Of these straits, Lombok Strait to the east carries a much higher volume transport, and is also closest to the seasonal core of SST cooling near the east end of Java. Adequate simulation of the transports through the straits, as well as of the general circulation patterns and ambient temperature gradients in the region, are needed to simulate how effectively processes (e.g., wind forcing, Kelvin waves, and mesoscale eddies) produce cooling or warming.

Since our focus is on the evolution of temperature anomalies during pIOD years, we restrict our validation to the onset of pIOD events only (May-July of pIOD years). We consider the bias (i.e., difference between the mean values of the OGCM and satellite observations) and RMS difference (between the OGCM and observational values on the same dates). When comparing the model SST to satellite observations during the onset of pIOD events during May-July, the model has a substantial warm bias in the Indian Ocean just south of the eastern part of Java, and extending eastward off the coast of Nusa Tenggara (Figure 5.3a). The outflow from Lombok Strait has a

particularly warm bias (> 1.5°C) relative to AVHRR satellite observations (Fig. 5.3a). The biases in surface dynamic topography gradients near Lombok Strait also suggest that the model is transporting too much water through the strait (Fig. 5.3b). This may have implications for how well the model represents the contribution of the strait flow to temperature tendency. The SST bias has a zonal gradient along the coast of Java, and therefore might have some effect on the zonal advective terms. However, there is not much of a cross–shore (meridional) gradient in the bias south of Java (Fig. 5.3a) and therefore the model's representation of the meridional advective terms should be minimally impacted.

With the bias removed, the root–mean–square (RMS) difference in temporal variability of SST between model and observations is approximately 0.5°C in most areas, with slightly higher values of 0.6–0.7°C in narrow regions near the coasts of Sumatra, Java, and Nusa Tenggara (Fig. 5.3c). These values are still small relative to the magnitudes of the anomalies associated with pIOD events, generally -1°C to -2°C near the coast (Figure 5.2b). The RMS difference values for dynamic topography (Fig. 5.3d) have maximum values where mesoscale eddies are most active, which is expected given that eddies are not forced directly by the atmosphere; it just indicates that the timing of mesoscale eddies in POP is different from observations.

Another criterion for assessing the suitability of the model for the study of anomalous Java cooling events is to examine the evolution of seasonal temperature and composite anomalies from pIOD years, as observed by satellites (Fig. 5.1, 5.2) and generated in the model (Fig. 5.4). (NB: The model averages presented here are for mixed layer-averaged temperature and velocity rather than surface values, though the model surface values are very similar.) In the observed seasonal climatology for

July–August (peak months of Java cooling) the most salient feature is a patch of cool SSTs south of eastern Java, extending about 200 km offshore (Fig. 5.1). Likewise, in the model's seasonal climatology for the onset and peak of Java cooling (Fig. 5.4a, b), the cooling is more pronounced at the eastern end of Java, consistent with the seasonal thermocline being shallower in this area (e.g., see Fig. 7 of Delman et al., 2016b). Model composites for pIOD years show temperature and velocity distributions that are a straightforward intensification of the seasonal cooling near the coast and enhanced flow from Lombok Strait (Fig. 5.4c, d). Model SST anomalies during pIOD years are most pronounced near the eastern end of Java at first (Fig. 5.4e), but cooling is more evenly distributed along the Java coast by the peak season (Fig. 5.4f); the spatial distribution and the magnitude of pIOD SST anomalies compares favorably with observations (Fig. 5.2). One difference from the observations is that SST anomalies along the southern Sumatra coast are almost as cool as those along the Java coast (Fig. 5.4e, f). This feature is most likely related to the warm bias in the model south of Java (Fig. 5.3a), which implies a weaker along–shore temperature gradient between the Sumatra and Java coasts.

5.3 Mixed layer temperature budget formulation

The form of the temperature budget used in this study follows the essential form introduced by Kim et al. (2004) and further developed in Kim et al. (2006, 2007). These studies (which we collectively refer to as Kim04–07) quantified temperature tendency contributions in the ECCO data assimilation product. One feature present in the Kim04–07 budgets that diverges from many earlier mixed layer budget studies (e.g., Qiu and Kelly, 1993; Qu, 2003; Dong and Kelly, 2004) is the explicit separation

of three terms: resolved–scale vertical advection, subgrid–scale vertical mixing, and the temperature tendency due to the change in the thickness of the mixed layer itself. In the earlier studies, the three terms are conflated into a single vertical entrainment term with an effective entrainment velocity diagnosed using the turbulent kinetic energy balance. The entrainment velocity is suitable for computing budgets using observations or coarse–resolution reanalysis products in which vertical velocity and/or mixing is difficult to compute directly; however, this aspect of the calculation is unnecessary when fluxes from both vertical advection and parameterized vertical mixing are archived in the model. Therefore, our budget analysis considers the three terms separately, which have the benefit of permitting the decomposition of vertical and horizontal advective tendencies into velocity and temperature components associated with individual processes.

The complete point–wise temperature budget, following Kim04–07 and Bryan and Bachman (2015) is:

$$\frac{\partial T}{\partial t} = -\nabla \cdot (\mathbf{u}T) + \frac{1}{\rho C_\rho}\frac{\partial q}{\partial z} - \nabla_h^2 \left(A_H \nabla_h^2 T\right) + \frac{\partial}{\partial z}\left[\kappa\left(\frac{\partial T}{\partial z} - \Gamma\right)\right] \tag{5.1}$$

with $\mathbf{u} = (u, v, w)$ being the three–dimensional velocity, ∇ and ∇_h are the three–dimensional gradient operator and two–dimensional horizontal gradient operator respectively, $C_\rho = 3996\,\mathrm{J\,kg^{-1}\,K^{-1}}$ is the specific heat capacity of seawater, q is the net (radiative and turbulent) heat flux, κ is the vertical temperature diffusivity computed from KPP, and Γ is the non–local transport term for convection. The heat flux q

consists of the components

$$q|_{z=\eta} = q_{\mathrm{SW}}|_{z=\eta} + q_{\mathrm{LWup}} + q_{\mathrm{LWdown}} + q_{\mathrm{lat}} + q_{\mathrm{sens}} \tag{5.2}$$

$$q|_{z=-h} = q_{\mathrm{SW}}|_{z=-h} \tag{5.3}$$

with the depth coordinates η being the displacement of the free surface relative to $z = 0$ and h being the (absolute value of the) mixed layer depth. The flux components are q_{SW} the downward shortwave radiative flux, q_{LWup} and q_{LWdown} the upward and downward longwave radiative fluxes respectively, q_{lat} the latent heat flux and q_{sens} the sensible heat flux. All of the quantities on the right-hand side of (5.2) and (5.3) were archived during the model simulation; the longwave radiative flux, latent heat flux and sensible heat fluxes are only nonzero through the surface interface (i.e., at $z = \eta$).

The budget in (5.1) computed using POP output differs from the budgets in Kim04–07 in that horizontal diffusion is computed using a biharmonic diffusivity A_H, and a non–local source term Γ representing convection in the near–surface boundary layer is also included (Smith et al., 2010; Bryan and Bachman, 2015). The near-surface boundary layer is the actively turbulent part of the mixed layer; its depth is diagnosed by KPP based on a bulk Richardson number criterion, and is generally slightly less than the mixed layer depth.

The point-wise temperature budget (5.1) is volume–averaged in the mixed layer with the operator $\langle\ \rangle$. The volume average of a term A is given by

$$\langle A \rangle \equiv \frac{1}{V} \iiint_V A \, dv \tag{5.4}$$

with V the volume of the mixed layer region being averaged and dv a unit element of that volume, following Bryan and Bachman (2015). In our analysis, the volume V has horizontal boundaries (either the boundaries of a single horizontal grid cell, or a multi-celled region) that do not change with time. In the vertical dimension, the boundaries are the spatially- and temporally-variable $z = -h(x, y, t)$ and $z = \eta(x, y, t)$. The mixed layer depth was computed in the model run based on the methodology of Large et al. (1997), by comparing the local, interpolated vertical potential density gradient to bulk depth–averaged values of the gradient between the surface and discrete grid levels. The mixed layer depth h is the shallowest depth at which

$$-\left.\frac{\partial \rho_\theta}{\partial z}\right|_{z=-h} = \mathrm{max}_{\mathrm{k}=1,2,\ldots,\mathrm{k}_{\mathrm{max}}} \left\{ \frac{(\rho_\theta - \rho_\theta|_{\mathrm{k}=1})}{|\mathrm{z}_\mathrm{k}|} \right\} \tag{5.5}$$

holds true for the value of the vertical potential density gradient $\partial \rho_\theta / \partial z$ interpolated at $z = -h$, where $k = 1$ is the surface grid cell level, k_{max} is the deepest vertical grid cell level above topography, and z_k is the depth at the center of the grid cell at level k (a more detailed description is given in Large et al., 1997).

By the chain rule, the volume–averaged budget $\langle (5.1) \rangle$ is related to the tendency in the volume–averaged temperature $\langle T \rangle$ as follows:

$$\frac{\partial}{\partial t}\langle T \rangle = -\frac{1}{V^2}\frac{\partial V}{\partial t} \iiint_V T \, dv + \frac{1}{V} \iint_{\partial V} \frac{\partial \mathbf{v}}{\partial t} T \cdot \hat{\mathbf{n}} \, da + \langle (5.1) \rangle \tag{5.6}$$

with ∂V the boundary surface of the averaged region V, da an element of the boundary surface, $\hat{\mathbf{n}}$ a unit vector facing normally outward from the region's boundary, and $\partial \mathbf{v} \equiv (\partial V / \partial a)\hat{\mathbf{n}}$ the vector representing the local change in the position of the boundary ∂V. The first two terms on the right–hand side of (5.6) are simplified by evaluating

the integral in the first term to obtain $V\langle T\rangle$, then absorbing this into the second term. The result is a volume–averaged budget with one more term than (5.1), due to the temporal change in the mixed layer's volume.

$$\frac{\partial}{\partial t}\langle T\rangle = \frac{1}{V}\iint_{\partial V}\frac{\partial \mathbf{v}}{\partial t}\left(T-\langle T\rangle\right)\cdot\hat{\mathbf{n}}\,da - \frac{1}{V}\iiint_{V}\nabla\cdot(\mathbf{u}T)\;dv + \frac{1}{V}\iint_{\partial V(z=-h,\eta)}\frac{1}{\rho C_\rho}\,q\;\hat{\mathbf{k}}\cdot\hat{\mathbf{n}}\,da$$
$$-\frac{1}{V}\iiint_{V}\nabla_h^2\left(A_H\nabla_h^2 T\right)\;dv + \frac{1}{V}\iint_{\partial V(z=-h)}\kappa\left(\frac{\partial T}{\partial z}-\Gamma\right)\hat{\mathbf{k}}\cdot\hat{\mathbf{n}}\,da \tag{5.7}$$

with $\hat{\mathbf{k}}$ a unit vector in the vertical direction, pointing upward.

Finally, the budget ishe part of the temperature flux $\mathbf{u}T$ that does not contribute to temperature tendency is removed by rescaling the temperature by $\langle T\rangle$.

Following Bryan and Bachman (2015), we use Gauss's law to rewrite the remaining volume integrations as fluxes through the boundaries. This includes rewriting the first two terms on the right-hand side (Lee et al., 2004) so that the temperature is rescaled by $\langle T\rangle$, i.e., $T_\Delta \equiv T - \langle T\rangle$. Since $\nabla\cdot\mathbf{u}=0$ in the model calculations, it is straightforward to show that $\iint_{\partial V}\mathbf{u}T\cdot\hat{\mathbf{n}}\,da = \iint_{\partial V}\mathbf{u}T_\Delta\cdot\hat{\mathbf{n}}\,da$. Hence the budget in this study is computed in the form

$$\frac{\partial}{\partial t}\langle T\rangle = -\frac{1}{V}\iint_{\partial V}\mathbf{u}T_\Delta\cdot\hat{\mathbf{n}}\,da + \frac{1}{V}\iint_{\partial V}\frac{\partial \mathbf{v}}{\partial t}T_\Delta\cdot\hat{\mathbf{n}}\,da + \frac{1}{V}\iint_{\partial V(z=-h,\eta)}\frac{1}{\rho C_\rho}\,q\;\hat{\mathbf{k}}\cdot\hat{\mathbf{n}}\,da$$
$$-\frac{1}{V}\iint_{\partial V}\nabla_h\left(A_H\nabla_h^2 T\right)\cdot\hat{\mathbf{n}}\,da + \frac{1}{V}\iint_{\partial V(z=-h)}\kappa\frac{\partial T}{\partial z}\,\hat{\mathbf{k}}\cdot\hat{\mathbf{n}}\,da - \frac{1}{V}\iint_{\partial V(z=-h)}\Gamma\;\hat{\mathbf{k}}\cdot\hat{\mathbf{n}}\,da \tag{5.8}$$

with the volume change term moved from the first to the second position on the right-hand side, in order to highlight the role of the advective term which will be

the primary focus of this paper. The budget terms on the right-hand side of (5.8), in order, are: the advective term (Advec), the volume change term (VCh), the radiative/turbulent heat flux or surface flux term (Surf), the horizontal diffusion term (HDiff), the vertical mixing term (VMix), and the convective term (Convec). In the figures of this manuscript, the surface flux term is decomposed as follows: the shortwave fluxes through the top and bottom of the mixed layer are summed together to give the total shortwave contribution, and the upward and downward longwave fluxes through the surface are summed together to give the total longwave contribution

$$\iint_{\partial V(z=-h,\eta)} \frac{1}{\rho C_\rho}\, q\, \hat{\mathbf{k}} \cdot \hat{\mathbf{n}}\, da = \iint_A \frac{1}{\rho C_\rho} \left(q_{\mathrm{SW}} + q_{\mathrm{LW}} + q_{\mathrm{lat}} + q_{\mathrm{sens}}\right)\, dA \tag{5.9}$$

with A indicating the horizontal area contained within the boundaries of the volume V, and dA a surface element of this area.

In order to highlight the contributions to temperature tendency from flow through each side of our region, we also make use of the boundary-flux form presented in Lee et al. (2004). In essence, by using the rescaled temperature T_Δ, the part of the temperature flux $\mathbf{u}T$ from each side that does not contribute to temperature tendency is removed. Thus, for a volume with 4 fixed walls facing horizontally (north, west, south, east) and top and bottom surfaces, the advective term in (5.8) can be decomposed as

$$-\frac{1}{V}\iint_{\partial V}\mathbf{u}T_{\Delta}\cdot\hat{\mathbf{n}}\,da=\frac{1}{V}\left(-\iint_{\partial V_{\text{north}}}-\iint_{\partial V_{\text{west}}}-\iint_{\partial V_{\text{south}}}-\iint_{\partial V_{\text{east}}}\right.$$
$$\left.-\iint_{\partial V_{\text{top}}}-\iint_{\partial V_{\text{bottom}}}\right)\mathbf{u}T_{\Delta}\cdot\hat{\mathbf{n}}\,da \qquad (5.10)$$

with $\partial V_{\text{north}}$ representing the north wall of the volume V.

One aspect of the budget geometry to note is that the horizontal walls of the region do not need to be zonal or meridional, and some of the walls of our study region south of Java are not. In budget computations using the model output, a boundary that is not aligned with the model grid is adjusted to align with model grid cell walls. For example, in the Java region outlined in Fig. 5.1, the "east" boundary is actually facing southeast (oriented southwest-northeast) to align more closely with the extent of the anomalous cooling. Therefore, in order to close the mass and temperature budgets in this case, fluxes were computed through both the south and east faces of grid cells along the boundary; the zig-zag shape of this revised boundary still forms a closed, continuous interface. However, the bottom wall (i.e., the mixed layer base) is treated differently, as the mixed layer depth is generally not aligned with the vertical interface of a grid cell. Vertical fluxes are interpolated to the actual mixed layer depth, while the horizontal components of fluxes through the sloping mixed layer base are computed through the horizontally-facing partial walls of cells.

5.4 Box-averaged temperature budget south of Java

Using the formulation described in Section 5.3, the temperature budget was averaged for the mixed layer, in the region south of Java extending to 10°S, as outlined in Figure 5.1. First, we consider the seasonal cycle of each of the terms (Figure 5.5), as computed by fitting the annual cycle and its first 3 harmonics to the 31 years of model output. Of the budget terms in (5.8), the surface flux term makes the largest contribution to the overall seasonal variation (Fig. 5.5a); this includes the start of seasonal cooling off Java in May-June. The decrease in incoming shortwave radiation as the solar radiation maximum reaches its furthest northward extent and daylight hours decrease is the dominant contributor to this cooling (Fig. 5.5b), though changes in cloudiness (suggested by increases in both outgoing and incoming longwave radiation; not shown) may also play a role. However, as incoming shortwave radiation starts to increase in July-August, advection and vertical mixing prolong the seasonal cooling (Fig. 5.5a). Applying the decomposition in (5.10), we find that advective cooling during the May-July onset phase is driven by temperature fluxes through the bottom edge of the box (i.e., the mixed layer base), as well as through the west wall of the box (Fig. 5.5c). The net volume fluxes through each wall of the box (Fig. 5.5d) suggest a seasonal advection of about 3 Sv through the bottom boundary (i.e., the mixed layer base). Advective cooling is also supported by a large flow (approximately 4 Sv) of relatively warm water leaving the box towards the west, likely due to the geostrophic response to lower sea surface height near the Java coast; this warm water is mostly replaced with cooler waters from below The seasonal cycle temperature budget

derived from POP is broadly consistent with the ECCO-based budget of Halkides and Lee (2009), though their budget did not find horizontal or vertical advection to be a substantial source of seasonal cooling; this discrepancy may be due to their different box limits, or the lower–resolution of ECCO (1° in the zonal direction, and 1/3° in the meridional direction within 10° of the equator).

With the seasonal cycle removed, we now consider the development of anomalies in the budget terms during various pIOD years. The budget terms and their surface and advective breakdowns are shown for three of these pIOD years (Figure 5.6), as examples of how anomalous pIOD cooling might manifest in a given year, and particularly to illustrate differences in the timing and evolution of cooling during pIOD years. In 1983 and 1994 the cooling develops as early as April or May and is initially driven by latent heat loss (similarly to the Java composite budget in Du et al., 2008), while no such contribution from latent heat flux cooling is observed in 2008 (Fig. 5.6d-f). The features that are common to all these years include advective and vertical mixing contributions to cooling, and a large shortwave-driven anomalous warming roughly coincident with the end of each cooling episode. As with the seasonal budget, the anomalous advective cooling comes predominantly from the mixed layer base and the west side of the box, with fluxes from the south acting as a warming influence (Fig. 5.6g-i).

To highlight the budget anomalies common to all eight pIOD years, composites were constructed of the anomalous temperature budget and surface/advective components, as well as of the volume flux anomalies (Figure 5.7). In these plots, pIOD composite averages that are not below the 5th or above the 95th percentile (as determined by bootstrap averaging of random 8-year combinations, with $n = 10{,}000$)

are grayed out, in order to consider only those features of the anomalous budget that are distinctive in pIOD years. Notably, vertical mixing-induced cooling and surface flux warming are the most long-lasting contributions to the budget that surpass the significance threshold (Fig. 5.7a). The significant contributions from advection are more sporadic during the year; however, they crucially overlap with the period of strongest pIOD-related cooling, and the composite total temperature tendency most closely tracks the advective contribution to temperature tendency anomalies during approximately June–July. The surface flux components each surpass the significance threshold for part of the year (Fig. 5.7b), but only the positive shortwave anomaly appears to make enough of a contribution to explain the significant total warming in October–November of the composite year (corresponding to the end of the anomalous pIOD cooling). As for the advective components, the contributions from the mixed layer base and west edge of the box together explain the anomalous cooling in June and July (Fig. 5.7c). The signs of both the tendencies and the volume fluxes at these edges reflect the seasonal contributions (Fig. 5.7c-d), so the anomalous advective term's contribution seems to be the result of an intensification in the seasonal upwelling and westward flow; however, it is not clear which of these processes is driving the intensification. Another feature of note is the warming contribution from the southerly inflow in July–August of the composite pIOD year (Fig. 5.7c), which coincides with an effective cessation of further cooling in the total tendency anomaly (Fig. 5.7a). At first glance this would appear to support the finding of Ogata and Masumoto (2010) that mesoscale eddy fluxes from the south are capable of stabilizing or reversing anomalous Java SST cooling, but a more targeted analysis of our model output is needed to determine whether mesoscale eddies can explain this warming contribution.

5.5 Maps of temperature budget terms

5.5.1 Seasonal cycle and anomaly maps

The volume-averaged temperature budget in (5.8) can also be used to compute a vertically-averaged budget in the mixed layer, by considering each horizontal grid cell as a distinct region and volume-averaging over the vertical stack of cells contained in the mixed layer. We use this to construct maps of the mixed layer temperature budget terms, showing the spatial distribution of the terms in the Java upwelling region and surrounding area. The maps (Figures 5.8–5.9) have values masked out at grid cells where a threshold for the budget closure is not met. The threshold for budget closure is whether the residual of the 30-day smoothed budget terms is less than $0.005°\text{C day}^{-1}$, for over 10% of the times being averaged; in this case, the times being averaged consist of May-July during the 8 pIOD years being composited. Despite having all of the budget terms theoretically needed for closure archived, the budget does not completely close due to variations in the thickness of the top layer of the model (the free surface), which affect the temperature changes in that layer; high-frequency variations in top layer thickness and temperature can not be completely reconstructed from 5-day averages. As a result, most of the Java Sea north of Java is masked out, since this is a region where the ocean is very shallow and such high-frequency variations can have an especially large impact.

The seasonal averages of the temperature budget terms during May-July (Figure 5.8) highlight the onset of the seasonal upwelling that distinguishes the Java upwelling region from its surroundings. The seasonal advective component of temperature tendency (Fig. 5.8a) produces warming in most areas, and most strongly in the

Lombok and Sunda Straits and their outflows; however, near the south coast of Java advection has a cooling influence. The surface fluxes induce cooling during this season nearly everywhere in the region (Fig. 5.8c) except within 20–30 km of the Java coast, where the surface flux produces warming that counteracts some of the advective cooling; as Fig. 5.5a indicates, the surface fluxes are still a net cooling in the Java upwelling region as a whole, which extends southward to 10°S. The other term to make a sizable contribution to the seasonal cooling is vertical mixing (Fig. 5.8e) which serves to reinforce the advective cooling along much of the coast of Java, while along with counteracting advective warming from the Lombok Strait outflow and within Sunda Strait.

We can also use the budget formulation in (5.8) to consider the contributions of each term to the temperature budget anomaly relative to the seasonal cycle (i.e., with the fields in Fig. 5.8 removed), and create May-July (i.e., onset of cooling) composites of the terms from the 8 pIOD years in the model output. In these composite anomaly maps (Figure 5.9) the major influences come from the same three terms as the seasonal tendencies, i.e., advection, surface fluxes, and vertical mixing. In the composite anomalies, however, there is little anomaly contribution south of approximately 10°S, as might be expected given the geographical constraints of the area that cools as pIOD events develop (Fig. 5.2). In the Java upwelling region itself, pIOD events involve an intensification of the seasonal tendencies, as both advection (Fig. 5.9a) and vertical mixing (Fig. 5.9e) provide anomalous cooling along the south coast of Java. The surface fluxes (Fig. 5.9c) produce anomalous warming near the coast of Java but have very weak nonseasonal tendencies further offshore, such that the surface fluxes have a net warming influence on the temperature anomaly as shown in the box-averaged

composite pIOD budget (Fig. 5.7a).

5.5.2 Seasonal velocity and temperature decomposition

In Sections 5.4 and 5.5.1, the seasonal cycle was regressed onto the budget terms directly. However, by applying the regressions separately to the velocity and temperature fields in the advective term, we can also gain some insight into the interactions of the seasonal cycle with intraseasonal or interannual anomalies, and make inferences about the phenomena (linear or nonlinear) likely to drive the associated temperature tendency contributions. The seasonal regression operator $\mathbf{R_S}$ converts a time series into its regressed counterpart

$$\mathbf{R_S} = \mathbf{A}\left[\left(\mathbf{A}^T\mathbf{A}\right)^{-1}\right]\mathbf{A}^T \tag{5.11}$$

where $\mathbf{A}$ is the matrix whose columns contain the cosine and sine values for the annual cycle and its 3 harmonics at each time value t_m in the model output, i.e., $\mathbf{A}_{m,n} = \cos\left\{2\pi\left[(\mathrm{n}+1)/2\mathrm{T}\right]\mathrm{t_m}\right\}$ and $\mathbf{A}_{m,n} = \sin\left\{2\pi\mathrm{T}\left(\mathrm{n}/2\mathrm{T}\right)\mathrm{t_m}\right\}$ with $T = 365$ days. (There are no leap days in the OGCM simulation.) Given this seasonal regression operator, the three-dimensional velocity $\mathbf{u}$ and rescaled temperature T_Δ fields can be written as

$$\mathbf{u} \equiv \mathbf{R_S}\mathbf{u} + \mathbf{u}^* = \mathbf{u^S} + \mathbf{u}^* \tag{5.12}$$

$$T_\Delta \equiv \mathbf{R_S}T_\Delta + T_\Delta^* = T_\Delta^S + T_\Delta^* \tag{5.13}$$

with $\mathbf{u_S}$ and T_Δ^S the velocity and rescaled temperature respectively obtained from

regressing the annual cycle and its harmonics, and $\mathbf{u}^*$ and T^* the residual (nonseasonal) velocity and rescaled temperature anomalies.

Therefore the advective term in the original pointwise budget in (5.1) can be written as

$$-\nabla \cdot (\mathbf{u}T) = -\nabla \cdot \left(\mathbf{u}^{\mathbf{S}} T_{\Delta}^{S}\right) - \nabla \cdot \left(\mathbf{u}^{*} T_{\Delta}^{S}\right) - \nabla \cdot \left(\mathbf{u}^{\mathbf{S}} T_{\Delta}^{*}\right) - \nabla \cdot (\mathbf{u}^{*} T_{\Delta}^{*}) \tag{5.14}$$

and the above terms can be volume-averaged and written in the same form as the boundary fluxes in (5.10), which is how the individual terms on the right-hand side of (5.14) are computed—though it is not written out here for the sake of brevity. The sum of the four right-hand side terms in (5.14) is the total advective contribution to the temperature tendency. If we are only interested in the parts contributing to the *anomalous* advective contribution to temperature tendency, the seasonal means are computed and removed from each volume-averaged term, resulting in the balance

$$\langle -\nabla \cdot (\mathbf{u}T) \rangle^{*} = \left\langle -\nabla \cdot \left(\mathbf{u}^{\mathbf{S}} T_{\Delta}^{S}\right) \right\rangle^{*} + \left\langle -\nabla \cdot \left(\mathbf{u}^{*} T_{\Delta}^{S}\right) \right\rangle^{*} + \left\langle -\nabla \cdot \left(\mathbf{u}^{\mathbf{S}} T_{\Delta}^{*}\right) \right\rangle^{*} + \langle -\nabla \cdot (\mathbf{u}^{*} T_{\Delta}^{*}) \rangle^{*} \tag{5.15}$$

If the mixed layer depth was constant, the term $\left\langle -\nabla \cdot \left(\mathbf{u}^{\mathbf{S}} T_{\Delta}^{S}\right)\right\rangle^{*}$ would be essentially zero because the components that contribute to it are already seasonally periodic—however, since the volume range being averaged changes from year to year, this term can have a non-negligible contribution.

The composite pIOD values of the components (Figure 5.10) in (5.15) show tendencies that may reflect a difference in the temperature changes produced by

quasi-linear dynamics (e.g., wind forcing and coastal Kelvin waves), vs. nonlinear dynamics (mesoscale eddies). In practice, the anomalous contribution of the seasonal velocity-seasonal temperature term $\left\langle -\nabla \cdot \left(\mathbf{u}^{\mathbf{S}} T_{\Delta}^{S} \right) \right\rangle^{*}$ is negligible except within the outflow of Lombok Strait (Fig. 5.10a), so we consider the contributions of the other components to anomalous Java mixed layer cooling. The anomalous advection of seasonal temperature term (Fig. 5.10b) has an anomalous cooling effect on the upwelling region; this is important, as both local wind forcing and Kelvin waves would exert their initial influence by inducing an anomalous velocity field. However, the seasonal advection of anomalous temperature term (Fig. 5.10c) also contributes substantially to the anomalous cooling. Meanwhile, the anomalous advection of anomalous temperature term (Fig. 5.10d) acts as a strong warming influence on the Java upwelling region. As this last term is likely to be most representative of nonlinear intraseasonal variability (e.g., mesoscale eddies), this would support the hypothesis that eddies act as a warming influence. For example, the result is consistent with the finding that the product of intraseasonal velocity and intraseasonal temperature variations exerted a net warming effect on the region starting in June-July of the 1994 pIOD event (Fig. 9a of Ogata and Masumoto, 2010).

5.6 Process-specific contributions to the temperature tendency

5.6.1 Methodology

One of the key objectives of this study is to move beyond the seasonal and anomalous temperature budgets analyzed in previous studies of this region, and

attempt to estimate the contributions associated with three specific processes: local wind stress forcing, Kelvin waves, and mesoscale eddies. As these processes will influence the temperature budget most directly through advection, our estimates will use the regression-based decomposition method of the advective term introduced in Section 5.5.2. However, instead of regressing onto the annual cycle and its harmonics, the process decomposition is carried out by regressing a time series (or multiple time series) onto the velocity and temperature anomaly fields. Once the regression is used to extract the part of the nonseasonal velocity and temperature field associated with the process, the seasonal velocities and temperatures are added to the residual (i.e., not process-related) velocities and temperatures.

For example, let A_P be either a column vector of the time series representing a process, or a matrix with columns consisting of each time series that represents a part of the process. Then analogously to (5.11)–(5.13), the regression operator R_P is

$$\mathbf{R_P} = \mathbf{A_P}\left[\left(\mathbf{A_P}^T\mathbf{A_P}\right)^{-1}\right]\mathbf{A_P}^T \tag{5.16}$$

and the velocity and temperature decompositions are

$$\mathbf{u} \equiv \mathbf{R_P}\mathbf{u}^* + \mathbf{u}' + \mathbf{u^S} = \mathbf{u^P} + \mathbf{u}^\circ \tag{5.17}$$

$$T_\Delta \equiv \mathbf{R_P}T_\Delta^* + T_\Delta' + T_\Delta^S = T_\Delta^P + T_\Delta^\circ \tag{5.18}$$

with $\mathbf{u^P}$ and T_Δ^P the anomalous velocity and temperature respectively associated with the process, $\mathbf{u}'$ and T_Δ' the residuals of anomalous velocity and temperature not associated with the process, and $\mathbf{u}^\circ = \mathbf{u}' + \mathbf{u^S}$ and $T_\Delta^\circ = T_\Delta' + T_\Delta^S$ the residuals plus

the seasonal values. Analogously to (5.15), the terms are volume adjusted and the seasonal means removed to summarize the contributions to anomalous temperature tendency

$$\langle -\nabla \cdot (\mathbf{u}T) \rangle^* = \left\langle -\nabla \cdot \left(\mathbf{u}^{\mathbf{P}} T_\Delta^P\right) \right\rangle^* + \left\langle -\nabla \cdot \left(\mathbf{u}^\circ T_\Delta^P\right) \right\rangle^* + \left\langle -\nabla \cdot \left(\mathbf{u}^{\mathbf{P}} T_\Delta^\circ\right) \right\rangle^* + \langle -\nabla \cdot (\mathbf{u}^\circ T_\Delta^\circ) \rangle^* \tag{5.19}$$

The first three terms on the right-hand side of (5.19) are considered collectively to be the contribution of the process to the advective temperature tendency anomaly. We carry out the regressions of each of the 3 processes independently, as a multivariate regression approach with all of the processes simultaneously would lead to a number of cross-product terms between processes, adding complexity and making attribution of the tendency anomalies to specific processes difficult. However, our chosen approach implies that the 3 processes are independent enough to be regressed individually for an estimate of each process's contribution. In this case the cross–correlations between the process indices (as defined in Section 5.6.2) are all below 0.2, so the independence of the processes is not a concern; however this approach would need to be altered for more closely related processes.

5.6.2 Indices to represent each process

In order to apply the process-based regressions in Section 5.6.1, time series are needed to represent each process. For the purposes of our study, the process-based regressions are carried out based on the 31 years of OGCM output for May-July only, as the velocity and temperature variations associated with each process are likely to shift with seasonal changes in circulation and temperature stratification. Once the

regressions have been computed, pIOD anomaly composites are formed by averaging the budget terms during May-July of the 8 pIOD years.

Local wind stress forcing is known to affect the velocity field by three mechanisms: zonal momentum transfer (from τ^x), meridional momentum transfer (from τ^y), and the effect of wind stress curl $\nabla \times (\tau^x, \tau^y)$, which induces vertical velocities from the convergences or divergences of the Ekman transport. So the process matrix $\mathbf{A_P}$ for wind stress consists of three columns: anomalies of τ^x, τ^y and $\nabla \times (\tau^x, \tau^y)$. By changing the velocity fields each process can also change the temperature gradients in the ocean, enhancing or reducing the effectiveness of advection in contributing oto the temperature tendency; hence we also regress temperature fields onto $\mathbf{A_P}$ to account for these effects. Since the objective is to determine the effect of anomalous *local* wind stress, the three wind stress quantities are spatially–averaged in 2° x 2° boxes, which are regressed onto velocities and temperatures in the same regions of the ocean; the regressed quantities from each of the boxes are then superimposed in a tapered overlapping patchwork with centers 1° latitude and 1° longitude apart, to construct continuous velocity and temperature fields that are regressed with local wind stress. (This is a compromise between averaging wind stress over the entire region, which would likely miss the impact of local variations in wind stress, and doing separate regressions for wind stress in each 0.1° x 0.1° horizontal grid cell which is computationally expensive.)

For Kelvin waves, an index is computed based on the meridional profile of Kelvin waves in the eastern equatorial Indian Ocean, where the vast majority of Kelvin waves propagate through in order to get to the coast of Java (e.g., Iskandar et al., 2005; Drushka et al., 2010; Delman et al., 2016b). Sea surface height anomalies

(relative to the seasonal cycle) are spatially-averaged in the region 90°–95°E, 2°S–2°N (η_{eq}), and in regions to the south and north: 90°–95°E, 5°–3°S (η_S) and 90°–95°E, 3°–5°N (η_N). Then as a bulk approximation to identifying the amplitude of a Kelvin wave based on its meridional profile (e.g., Boulanger and Menkes, 1995, 1999; Delman et al., 2016a), an upwelling Kelvin wave index η_K is defined by differencing the sea surface height around the Kelvin wave crests/troughs from that on either side: $\eta_K = -[\eta_{eq} - 0.5\,(\eta_S + \eta_N)]$. Unlike the spatially-varying wind stress regressions, velocities and temperatures throughout the entire map domain are regressed with the same Kelvin wave index, derived from the equatorial 90°–95°E region. To confirm that the velocity fields regressed with the upwelling Kelvin wave index are credible representations of local Kelvin wave activity, the correlations of the mixed layer-averaged velocity field are computed with the upwelling Kelvin wave index at various velocity orientations and lags, and the optimum correlation coefficients and velocity orientations/lags are plotted (Figure 5.11a). The upwelling Kelvin wave index has elevated correlations with mixed layer velocity near the Java and Sumatra coasts in a generally westward orientation, and at the outflow of Lombok Strait in a generally southwestward orientation. The optimum lead times for the index are 5–10 days relative to velocities near the coast of Java (Fig. 5.11b), and based on this a lead time of 10 days is used to estimate the Kelvin wave impact on anomalous temperature tendency in Section 5.6.3.

To define an index representing mesoscale eddy activity, we use surface meridional velocity, band-passed for mesoscale frequencies (20–180 days). The band-passed velocity is averaged in 2° x 2° boxes centered at 12°S, the axis of mesoscale eddy variability in the region (Feng and Wijffels, 2002), and at longitude centers spaced 1°

apart throughout the region. As the eddies propagate nearly zonally in a band near 12°S (Feng and Wijffels, 2002; Yu and Potemra, 2006), an overlapping patchwork of regressions is again employed in this case, but only to account for zonal variations in eddy activity. For example, band-passed meridional surface velocity averaged in the box 13°–11°S, 109°–111°E is regressed onto velocity and temperature fields between longitudes 109°E and 111°E, at all latitudes. Then this regression range is tapered and overlapped with adjacent regression ranges of longitudes 108°–110°E and 110°–112°E, and so on in each direction, so that we are considering the influence of the mesoscale eddy activity closest to the velocities/temperatures being regressed. The correlations of the mixed layer-averaged velocity field for the mesoscale eddy index centered at 110°E (Fig. 5.11c) show some effect of eddies on the velocity field all the way to the Java coast, though the correlation coefficients decrease substantially north of 10°S. The optimum lead times for eddy influence range from 0–10 days (Fig. 5.11d), and a lead time of 0 days is used for the mesoscale eddy regressions, though a 5-day lead time was also tested and did not yield a substantially different result.

5.6.3 Maps of process contributions to temperature tendency

Based on the regression methodology described in Section 5.6.1, the pIOD composite patterns seen in the anomalous advective contribution to temperature tendency along the coast of Java (Figure 5.12a) can largely be explained by the three processes that are the focus in this study. Anomalous wind stress forcing has a fairly uniform cooling effect within 30–50 km of the Java coast (Fig. 5.12b), and a warming effect on the outflow of Lombok Strait, where southeasterly wind stress anomalies drive a stronger Ekman transport through the strait. The Kelvin wave influence also

has a cooling influence, which is less uniform along the coast (Fig. 5.12c); in some areas the Kelvin waves produce robust cooling, while in other places the influence is fairly neutral. Thus the wind stress and Kelvin wave influences both appear to be important contributors to anomalous cooling, a result that contrasts with findings from observations that wind stress anomalies have little influence on the evolution of Java SST (Delman et al., 2016b).

The mesoscale eddy influence based on our regression method acts to remove heat from the Lombok Strait ouflow, and spread it mostly in the onshore direction (Fig. 5.12d), though very little of this warming reaches the immediate coastal region where the most robust anomalous cooling happens. Instead, the eddies appear to have the effect of translating the warm tongue of the Lombok Strait outflow to the north of 10°S, with the most pronounced impact in the range 112°–115°E, but the warming effect associated with mesoscale eddies by this method falls well short of the warming influence associated with the anomalous velocity-anomalous temperature term (Fig. 5.10d).

5.7 Conclusions

When Saji et al. (1999) identified the Indian Ocean Dipole as an independent mode of climate variability they noted that the cool SST anomalies associated with pIOD events first appear in the upwelling region along the south coast of Java. Therefore quantifying the influence of the various processes that influence surface mixed layer temperature south of Java is critical to understanding how pIOD events evolve; however, these processes have not been well-resolved in most earlier model budget studies. Our analysis takes advantage of 31 years of interannually-varying

OGCM output with a horizontal resolution of approximately 0.1° to quantify not only the seasonal temperature budget and anomalies relative to it, but also to estimate the contributions that can be attributed to specific processes. The results of our seasonal temperature budgets (Fig. 5.5, 5.8), and of composite pIOD anomaly budgets (Fig. 5.7, 5.9), are generally consistent with earlier studies (e.g., Du et al., 2008; Halkides and Lee, 2009), but our budgets attribute somewhat more cooling to horizontal and vertical advection, which may have been underestimated in the earlier work using coarser-resolution output. For the first time, maps of the temperature budget terms (Fig. 5.8–5.9) are presented illustrating that most of the advective cooling is concentrated very close to the coast (within 30–50 km). The seasonal cycle decomposition shows that the anomalous velocity-anomalous temperature cross-term representing nonlinear interactions of the velocity and temperature fields has a net warming influence on the region, while anomalous (seasonal) advection of seasonal (anomalous) temperature gradients both have cooling effects.

A methodology is introduced to isolate the part of the advective temperature tendency that may be attributed to a specific process, by regressing the velocity and temperature fields onto an index (or indices) representing the process. In this way local wind stress and Kelvin waves have a comparable amount of cooling attributed to them in the Java upwelling region (Fig. 5.12b,c); the local wind stress more concentrated near the coast and evenly distributed in the along-coast direction, while the Kelvin wave contribution is focused in certain areas along the coast but extends somewhat further offshore. Mesoscale eddies just to the south of the upwelling region are identified as having a warming influence (Fig. 5.12d), but their effect is fairly modest and confined to the southeastern corner of the upwelling region, where steep

lateral temperature gradients flank the Lombok Strait outflow. In aggregate, we show that the combined effects of local wind stress forcing and Kelvin waves can plausibly explain the anomalous SST cooling observed south of Java during pIOD years.

One of the key results from this study contrasts with earlier work (Delman et al., 2016b) suggesting that local wind stress anomalies have little effect on the SST anomaly south of Java. Moreover, while Delman et al. (2016b) found upwelling Kelvin wave activity originating in the equatorial Indian Ocean to be a robust predictor of the development of pIOD events, the results in this manuscript indicate that Kelvin waves would only be responsible for about half of the local anomalous cooling. We note that another study (Chen et al., 2015) found that local wind stress (specifically, meridional wind stress and wind stress curl) exerts some influence on SST anomalies south of Java, in a HYCOM OGCM simulation with 0.25° horizontal resolution. While an earlier observational analysis of 0.25° x 0.25° scatterometer-based CCMP wind observations (not shown) did not show either meridional wind stress or wind stress curl to be a robust influence on Java SST anomalies, it is possible that the wind stress observations closest to the coast are degraded by land interference. A temporal low-pass smoothing filter in the observational analysis also may have excluded the effects of variations in the wind stress or wind stress curl at periods shorter than 30 days. Another possibility is that the CORE wind stress used to force the model, which is interpolated from NCEP reanalysis with approx. 1.9° horizontal resolution and corrections from scatterometer data (Large and Yeager, 2009), has inaccuracies near the coast of Java.

In addition to affecting advection, ocean processes such as those considered in this study may also influence the temperature budget by inducing changes in vertical

mixing. These effects are not as direct as the contributions from advection; instead, the advection associated with a given process may have an effect on vertical gradients of temperature and velocity, which in turn influence the amount of vertical mixing that is parameterized in the POP OGCM simulation. The KPP parameterization of vertical mixing used in POP depends on the temperature stratification, and on the the diffusivity which in most areas is a function of a bulk Richardson number in the surface layer (Large et al., 1994; Smith et al., 2010). Baroclinic Kelvin waves affect the temperature stratification $\partial T/\partial z$ (e.g., for upwelling Kelvin waves, by compressing isopycnals near the surface), as well as the vertical velocity shear that goes into the parameterized diffusivity; upwelling (downwelling) Kelvin waves would tend to increase (decrease) the vertical velocity shear associated with the cross-shore density gradient by the thermal wind relation. Upwelling induced by local wind stress would also be expected to affect the temperature stratification at the base of the mixed layer, but its effect on vertical velocity shear is much less certain, especially since seasonal local winds (southeasterly trade winds) are already strong. Hence, it is possible that Kelvin waves contribute much more than wind stress to cooling by vertical mixing. It might be possible to use an analysis framework to separate the influences of wind stress and Kelvin waves on mixing-induced cooling as we have done for advective cooling, but we would expect this to contain some challenges, such as attempting to estimate the accumulated effect of high-frequency variations in diffusivity and temperature stratification using 5-day averages. A salinity-stratified barrier layer may also influence temperature changes due to vertical mixing along the Java coast; the impact of the barrier layer along the Sumatra coast has been established (e.g., Masson et al., 2004; Delman et al., 2016b), but it is possible that process-induced barrier layer thickness

changes along the Java coast could also have effects on the temperature budget.

Our results also showed that the impact of mesoscale eddies on mixed layer temperature south of Java appears to be very modest during the onset of anomalous cooling; however, we consider it likely that eddies have a greater effect on the Java SST anomaly than that depicted in Figure 5.12d, particularly as the anomalous SST cooling reaches and passes its peak. For example, in the box-averaged composite pIOD budget (Fig. 5.7c), the warming tendency associated with advection from the south edge of the region only becomes significant starting in July, and it continues to be influential through August, so a focus on the peak phase of Java SST cooling might show larger contributions from mesoscale eddies. Moreover, a large warming contribution from the anomalous advection of anomalous temperature term (Fig. 5.10d) remains unexplained. It is possible that our chosen index of mesoscale eddy activity, centered on 12°S, may not capture the effects of other smaller-scale instabilities that develop closer to the Java coast. A more targeted approach to isolating the contributions of intraseasonal variability might have some success in characterizing the source of this warming tendency. Such an analysis could use band-passing similar to the work done by Ogata and Masumoto (2010), but would also need to consider the spatial distribution of intraseasonal contributions to the advective term in order to determine how close to the coast the warming effects of intraseasonal variability can be considered important.

5.8 Acknowledgements

Andrew Delman (ASD) was supported by a NASA Earth and Space Science Fellowship, grant number NNX13AM93H. Janet Sprintall (JS) and Julie McClean (JLM) were supported by NASA award number NNX13AO38G. Lynne Talley (LDT),

JLM, and ASD were also supported by NSF grant OCE–0927650. JLM was also supported by U.S. Department Of Energy Office of Science (BER) grant entitled "Ultra-High Resolution Global Climate Simulation" via a Los Alamos National Laboratory subcontract. The CCMP wind data were obtained from the Physical Oceanography Distributed Active Archive Center (PO.DAAC) at the NASA Jet Propulsion Laboratory, Pasadena, CA (http://podaac.jpl.nasa.gov). The optimal interpolation SST data were produced and distributed through the National Centers for Environmental Information (NCEI) of NOAA (https://www.ncdc.noaa.gov/oisst). The altimeter products were produced by Ssalto/Duacs and distributed by Aviso, with support from CNES (http://www.aviso.oceanobs.com/duacs/).

We owe profuse thanks to Ben Johnson and Jim Carton, who provided access to the output from the high-resolution simulation of POP that was the basis of this study. We also are grateful to the National Center for Atmospheric Research (NCAR) for giving us resources on the Yellowstone computing environment (account CSIO0001), and on the Geyser machine in particular, in order to carry out the analysis computations. Finally, ASD would like to thank the Scripps/UCSD/NCAR New and Young (SUNNY) program for supporting his working visits to NCAR, which initiated a collaboration with Frank Bryan that was essential to completing this work.

Chapter 5, in full, is currently being prepared for submission for publication of the material, by Delman, A. S., McClean, J. L., Sprintall, J., Talley, L. D., and F. O. Bryan. I was the primary investigator and author of this paper; the co-authors supervised and assisted with the preparation of the manuscript, and helped with understanding the methodology of computations using the model output.

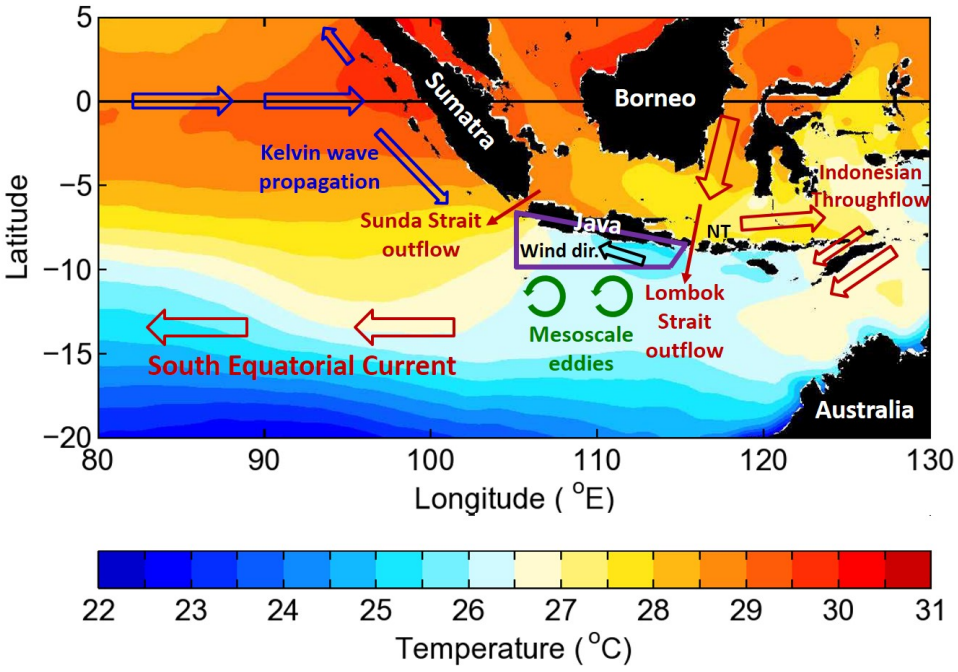

Figure 5.1: Map of the area surrounding Java. The Java upwelling region that will be the focus of this analysis is indicated by the purple box outline; various dynamical processes in the region are annotated. Major landmasses and islands are also labeled, including the Nusa Tenggara island chain (abbreviated as NT). The shading is the climatological mean SST during July–August, from AVHRR satellite data.

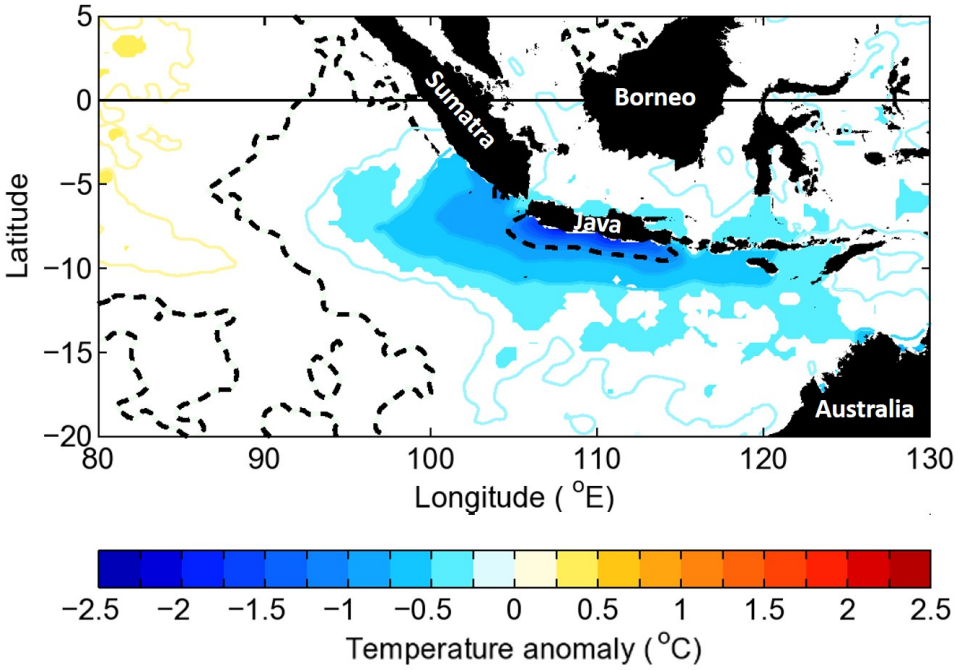

Figure 5.2: Composite July–August SST anomalies from AVHRR satellite data, derived from 8 pIOD years (1982, 1983, 1994, 1997, 2003, 2006, 2007, 2008). The seasonal cycle was defined based on the AVHRR data record for 1982–2013. Shaded areas indicate values that pass the 95% confidence threshold, based on bootstrap sampling (composite averages of random combinations of 8 July–August periods, with $n = 1000$). The contour interval is 0.25°C, with the dashed black contours corresponding to values of -1°C and 0°C.

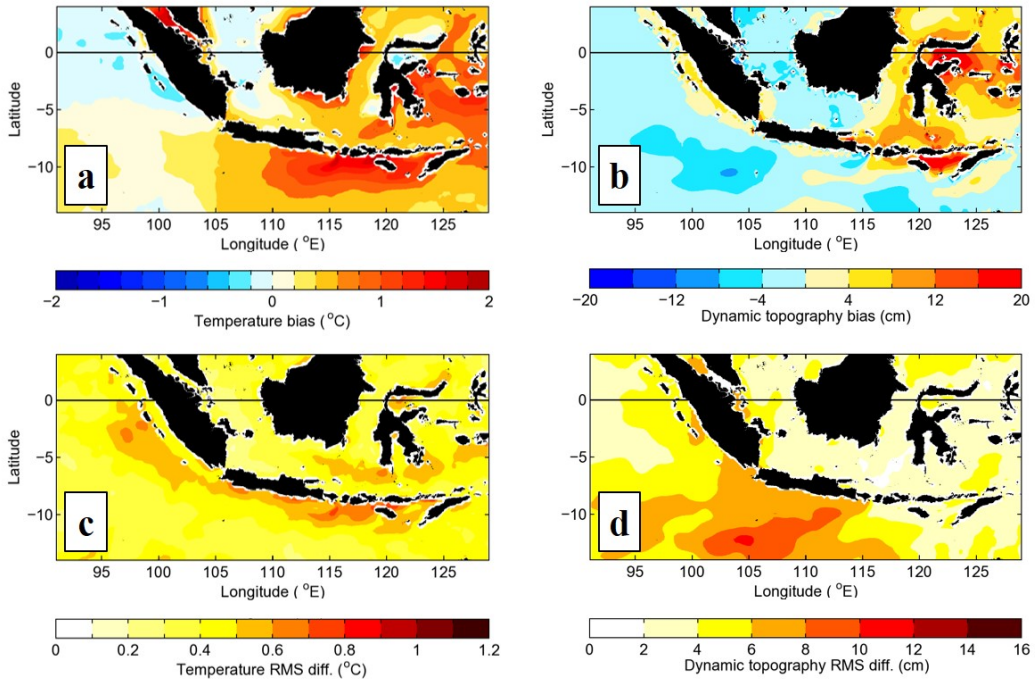

Figure 5.3: (a) SST bias of the POP simulation, relative to AVHRR satellite data, and (b) Surface dynamic topography bias of POP simulation, relative to AVISO maps of absolute dynamic topography (MADT), during May-July of 8 pIOD years. (c) RMS difference between temporally-coincident values of SST in the POP simulation and AVHRR data, and (d) RMS difference between temporally-coincident values of dynamic topography in the POP simulation and AVISO data, for May-July of pIOD years, with the mean bias in each location removed. All time series of SST and dynamic topography were temporally-smoothed with a 30–day moving average prior to computations.

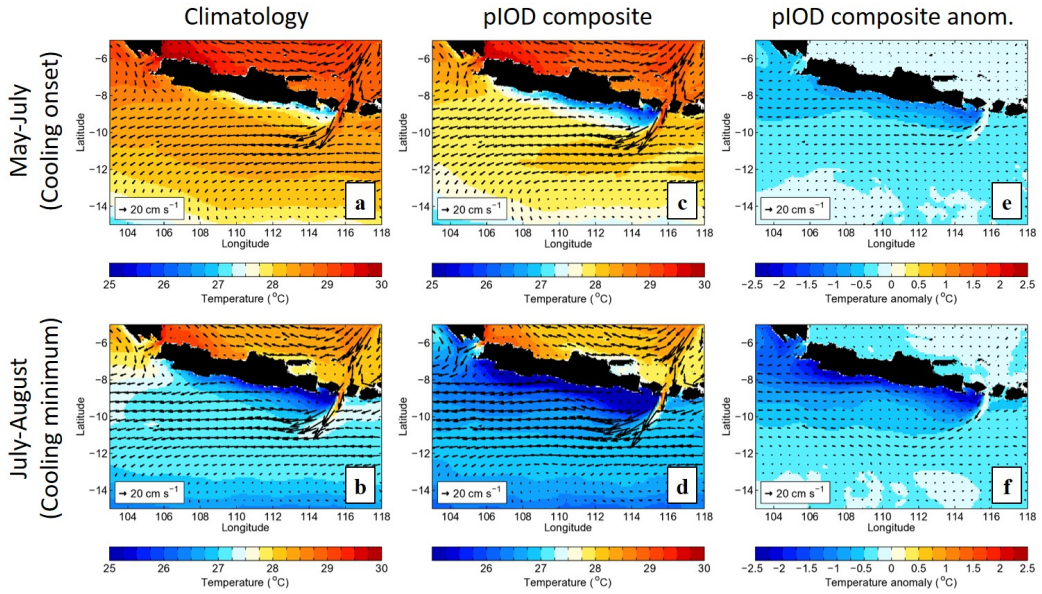

Figure 5.4: (a) Averages of the seasonal mixed layer temperature (shaded) and velocity (vectors) in May-July, the "cooling onset" period. (b) Same as (a), but averaged during July-August, the "cooling minimum" period. (c, d) Averages of mixed layer temperature (shaded) and velocity (vectors) during 8 pIOD years, for May-July and July-August respectively. (e, f) Composite anomalies of mixed layer temperature (shaded) and velocity (vectors) averaged during May-July and July-August of the 8 pIOD years.

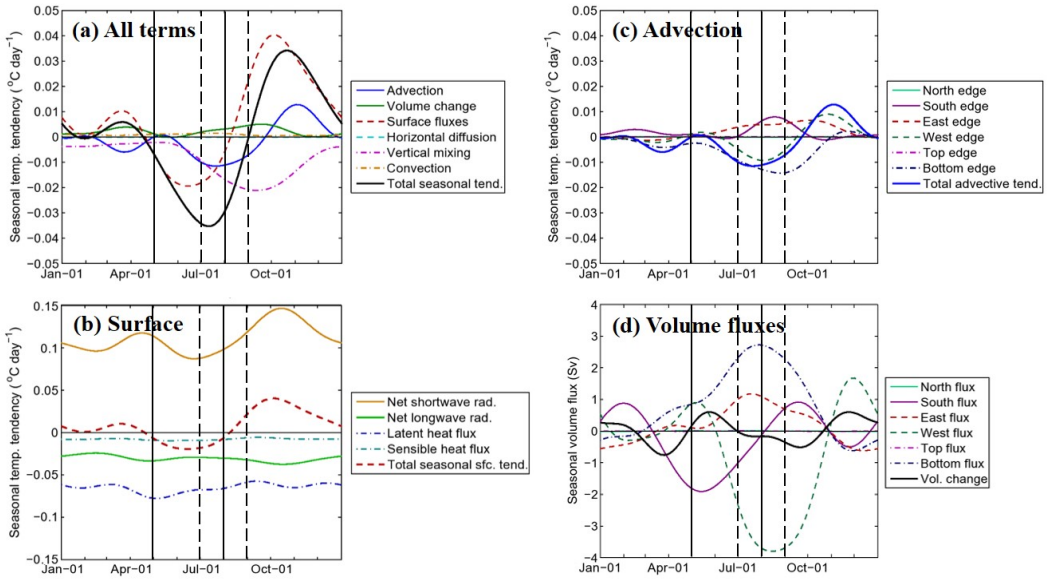

Figure 5.5: (a) The seasonal cycle of the temperature budget terms as formulated in (5.8), computed from 31 years of POP output (1979–2009), and averaged in the mixed layer within the region south of Java outlined in Figure 5.1. The seasonal cycle is computed from each of the terms by a multivariate regression of the annual cycle and its first 3 harmonics. (b) Seasonal cycle of the surface flux components that contribute to the temperature tendency, as given in (5.9). (c) Seasonal cycle of the advective components that contribute to the temperature tendency, as given in (5.10). (d) Seasonal cycle of the volume fluxes through each boundary of the region, with positive (negative) values indicating a flux into (out of) the region. The solid vertical lines indicate the bounds of the cooling onset season (May-July), and the dashed vertical lines indicate the bounds of the cooling minimum season (July-August).

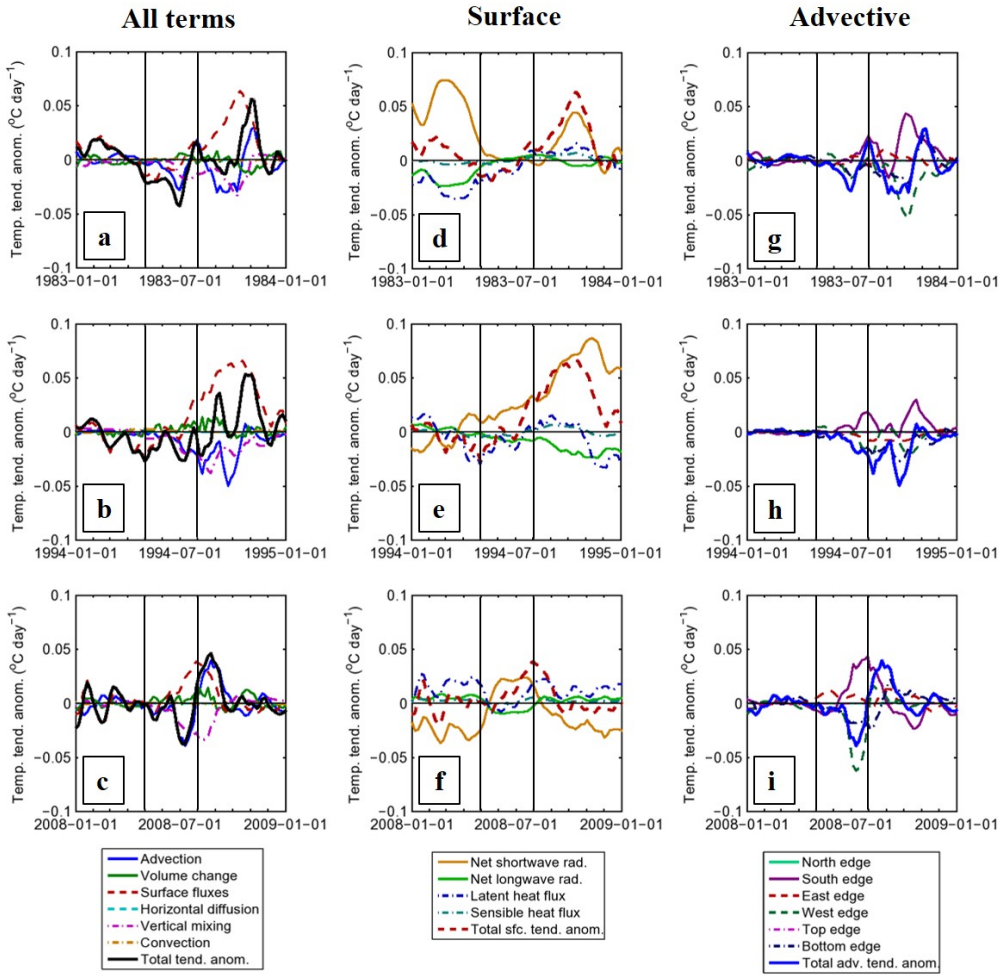

Figure 5.6: (a)-(c) The anomalies of the temperature budget terms averaged in the mixed layer south of Java, relative to the seasonal cycle, for 3 pIOD years (1983, 1994, and 2008 respectively). (d)-(f) Same as (a)-(c), but for the surface flux components that contribute to the temperature tendency anomaly. (g)-(i) Same as (a)-(c), but for the advective components that contribute to the temperature tendency anomaly. The solid vertical lines indicate the bounds of the cooling onset season (May-July).

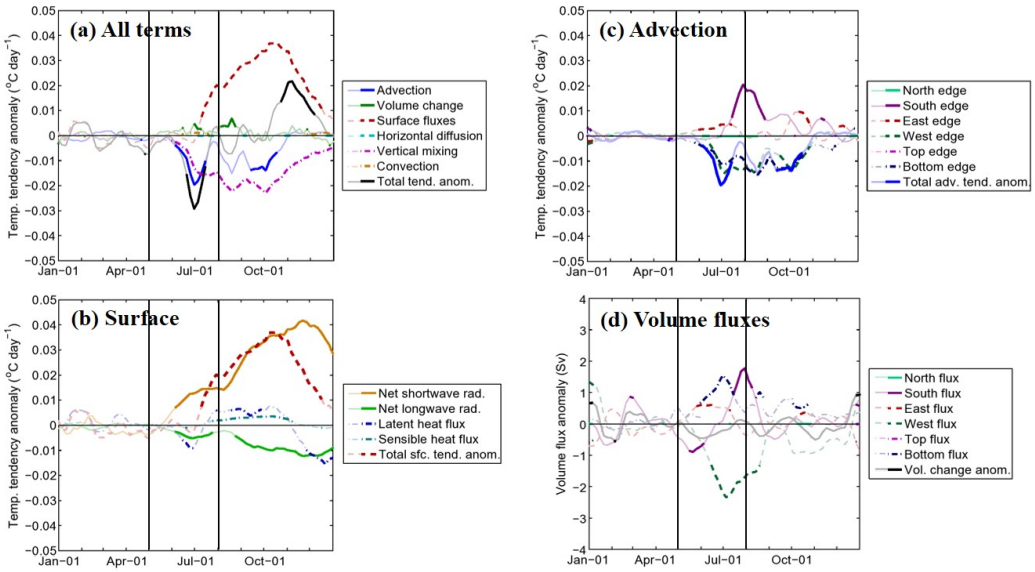

Figure 5.7: (a) Composite anomalies of the temperature budget terms averaged in the mixed layer south of Java, from 8 pIOD years (1982, 1983, 1994, 1997, 2003, 2006, 2007, 2008). A bootstrap method of averaging random 8-year combinations ($n = 10{,}000$) was used to establish a significance threshold, and composite values that are not greater or less than 95% of the random year combinations have been washed out. (b) Same as (a), but for composite values of the surface flux components that contribute to the temperature tendency anomaly. (c) Same as (a), but for composite values of the advective components that contribute to the temperature tendency anomaly. (d) Same as (a), but for the volume fluxes through each boundary of the region. The solid vertical lines indicate the bounds of the cooling onset season (May-July).

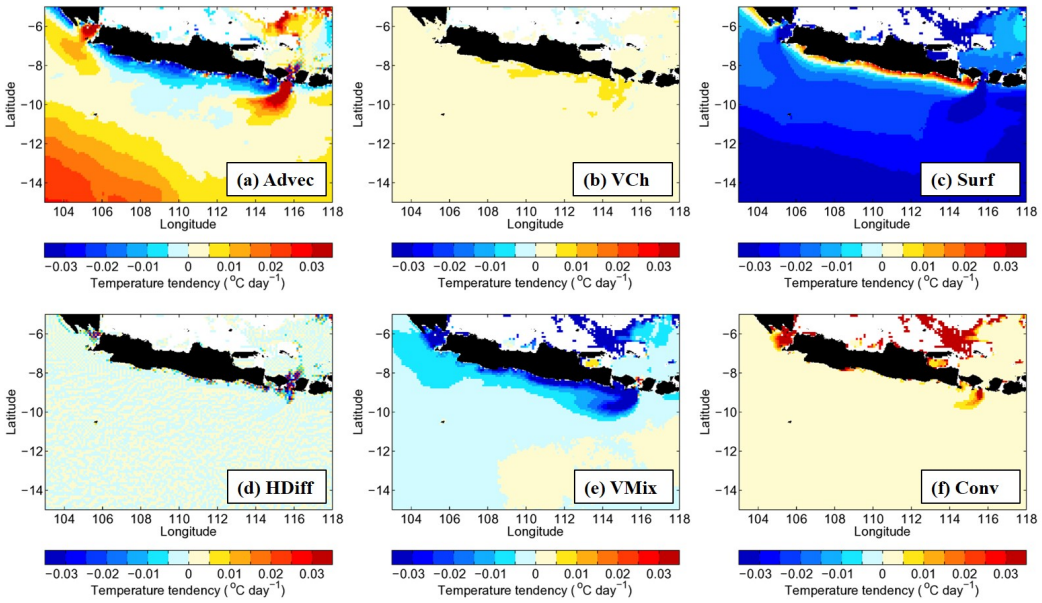

Figure 5.8: Seasonal cycle maps of the temperature budget terms in (5.8), depth-averaged in the mixed layer at each horizontal grid cell of the model. The terms are presented in the same order as in the legend of Figure 5.5a, specifically: (a) advection, (b) mixed layer volume change, (c) surface fluxes, (d) horizontal diffusion, (e) vertical mixing, and (f) boundary layer convection. Values are masked out for grid cells where the 30–day smoothed budget has a residual of larger than 0.005°C day^{-1}, at more than 10% of times within the composite pIOD averaging periods (i.e., May-July of the 8 pIOD years).

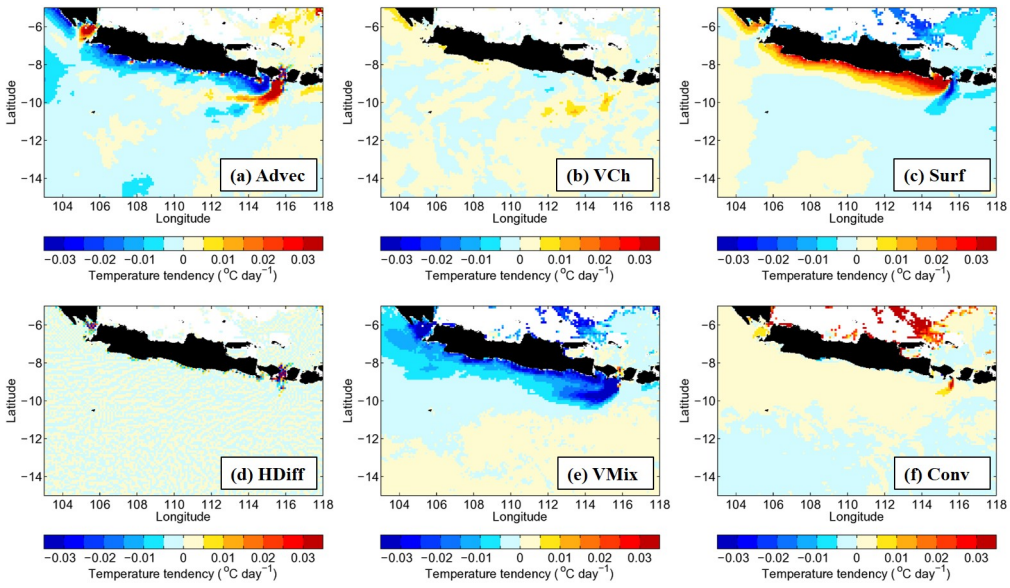

Figure 5.9: Composite pIOD anomaly maps of the temperature budget terms in (5.8), depth-averaged in the mixed layer at each horizontal grid cell of the model, and averaged during May-July of the 8 pIOD years in the model output. The terms are presented in the same order as in the legend of Figure 5.8, with values also masked out using the same criteria as in Figure 5.8.

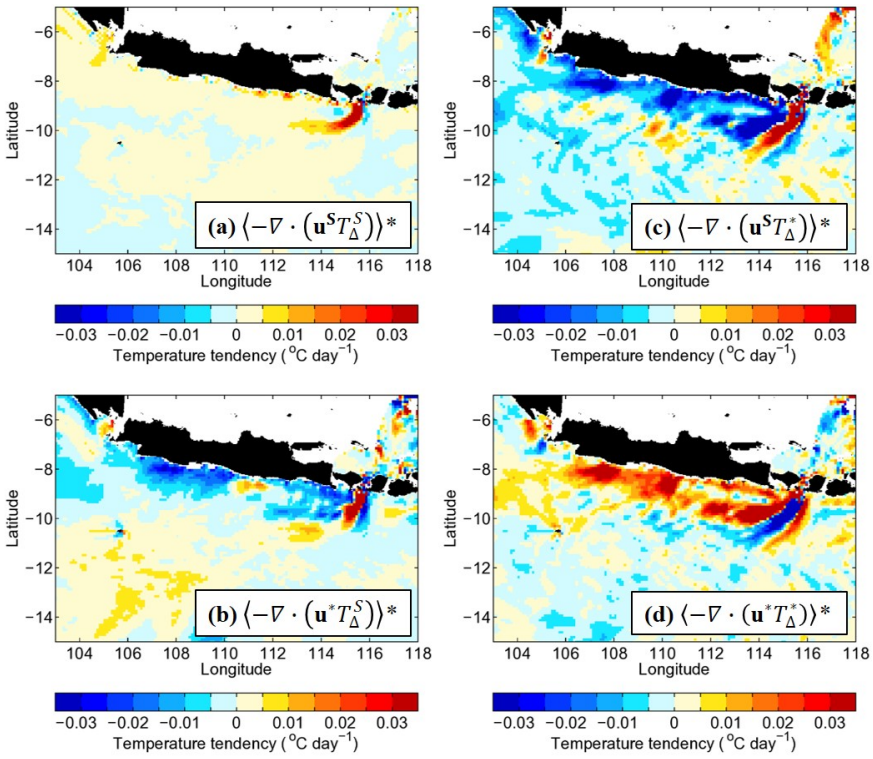

Figure 5.10: Decomposition of the anomalous advective temperature tendency (Figure 5.9a) into components due to the cross-products of seasonal and anomalous velocity and rescaled temperature, as indicated in (5.15). Values are masked out as in figures 5.8–5.9, and also for grid cells at which any corrupted values in the model output impacted the seasonal cycle regressions of velocity and rescaled temperature.

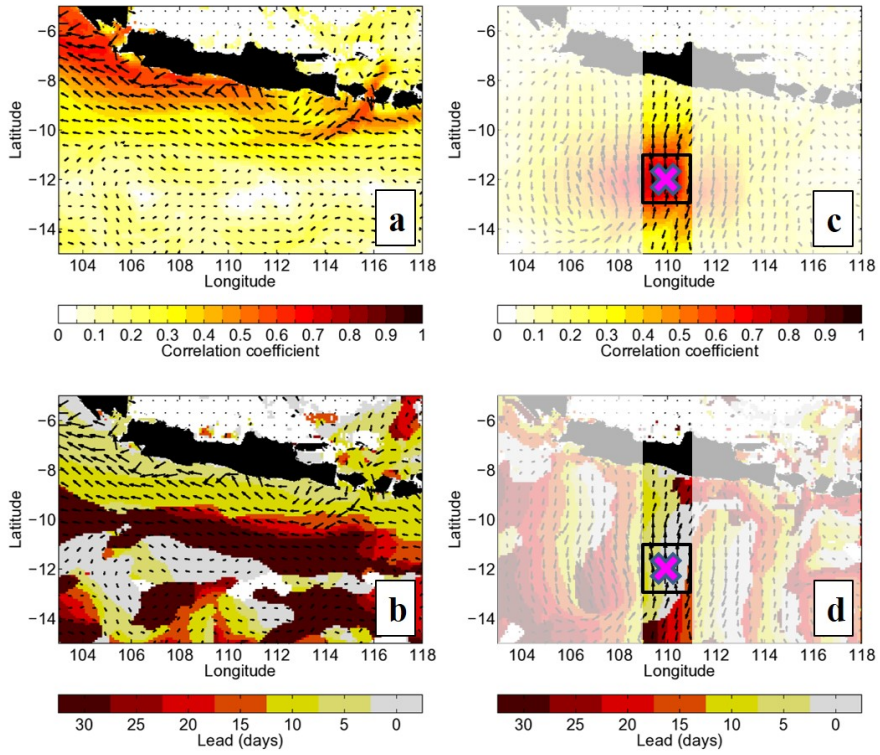

Figure 5.11: (a) Correlation coefficient (shading) of the upwelling Kelvin wave index with mixed layer-averaged velocity in the Java region, at optimal velocity orientations and lead times of the Kelvin wave index; only correlations surpassing the 95% confidence threshold are shaded. Vectors indicate the orientation of the optimal correlation with the upwelling Kelvin wave index. (b) Optimum lead times (shading) of the upwelling Kelvin wave index, relative to velocities in the Java region, with optimum orientations plotted as in (a). (c) Same as (a), but for the mesoscale eddy index centered at 12°S, 110°E (magenta "X"); the index centered at 110°E is averaged in the indicated black box and applied only to longitudes in the range 109°–111°E, as described in Section 5.6.2. (d) Optimum lead times (shading) of the upwelling Kelvin wave index, relative to velocities in the Java region, with optimum orientations plotted as in (c).

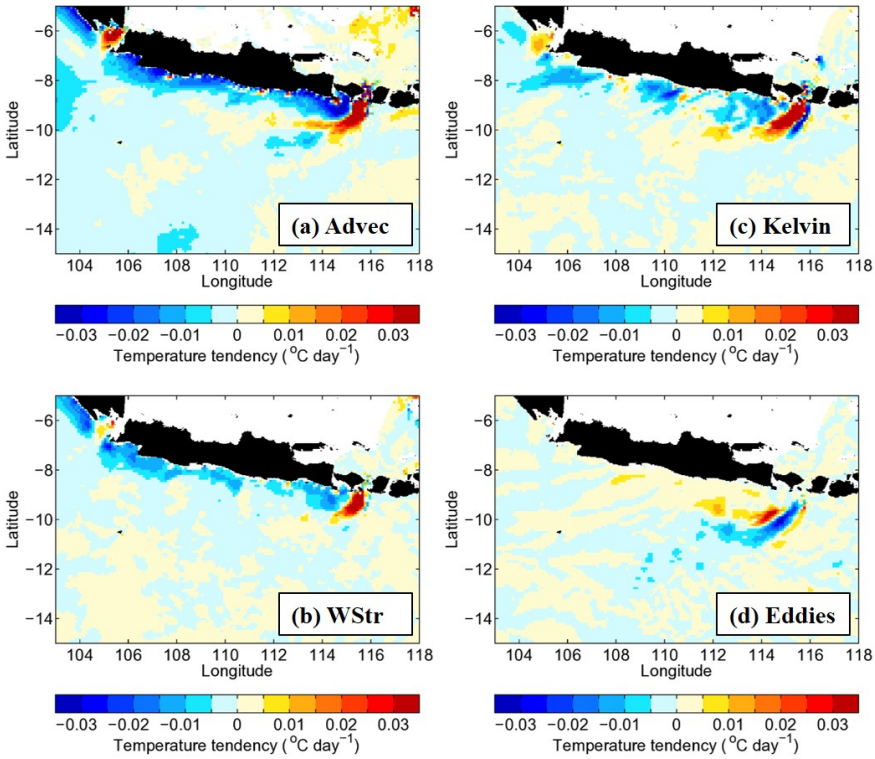

Figure 5.12: (a) The total advective contribution to the temperature tendency, composited from May-July of the 8 pIOD years and reproduced from Figure 5.9a, and pIOD composites for the temperature tendencies from advection associated with (b) local wind stress forcing, (c) Kelvin waves, and (d) mesoscale eddies. Values are masked out as in Figure 5.10.

Chapter 6

Conclusions

In this thesis, the contributions of specific mesoscale processes to the mean state and variability of the near-surface ocean were described, both qualitatively and quantitatively, using several novel analysis frameworks. Chapter 2 examined the eddy–mean flow interaction in the Kuroshio Extension (KE) region, using a vorticity budget analysis of ocean GCM output, and a coordinate system was defined relative to the KE jet axis to focus on the eddy contributions to along-jet velocity and cross–jet gradients. The eddy vorticity budget terms indicate that the vorticity anomalies associated with the recirculation gyres (and thus the gyres themselves) are eddy-driven, rather than the result of potential vorticity advection of the mean flow. Most importantly, near the KE jet axis and its associated front, the budget in the jet reference frame revealed a complex structure of eddy-induced decelerations and accelerations that could not be identified from Eulerian averages. Specifically, eddies tend to decelerate the mean jet along its axis, but that they also can accelerate the jet as flow moves from a crest to a trough in the jet's topographically–induced meanders. This pattern of eddy-mean flow interaction, previously undescribed along the KE jet, highlights the role mesoscale

eddies may play in frontogenesis and the role of topography in determining how eddies interact with a strong jet.

The remainder of this work focuses the local impacts of the passage of Kelvin waves and—to a lesser extent—mesoscale eddies on the surface ocean south of Java, with a particular focus on their role in the evolution of positive IOD climate events. Chapter 3 describes the use of a new method to isolate the Kelvin wave signal from satellite altimetry data, using projections of theoretical cross-wave profiles and harmonic basis functions followed by a least-squares fit. The method provides a means of estimating the Kelvin wave amplitude from sea surface height data alone, while taking into account both the cross-wave structure and its zonal or along-coast phase propagation to improve the estimate. A sample year and statistical assessments indicate that the common practice of tracking Kelvin waves using only raw sea surface height values, without considering sea surface height gradients or signal propagation, may not accurately indicate the origin of the wave. Chapter 4 applied the method developed in Chapter 3 in tandem with other datasets to highlight the role of wind forcing and Kelvin waves in producing anomalous cooling south of Java, during the early stages of pIOD events. In this chapter it was found that wind stress west of Sumatra near the equator is much more influential than local wind stress at producing the cool Java SST anomalies associated with pIOD events; moreover, upwelling Kelvin wave activity in April-June was shown to be a robust predictor of positive IOD index values in July–December. Chapter 4 suggests that the Java SST anomalies that help initiate pIOD events are the result of easterly wind forcing along the equator or coastal Sumatra, which generates upwelling Kelvin waves during austral fall/boreal spring. Due to the deep thermocline and barrier layer in the eastern equatorial Indian Ocean,

these Kelvin waves do not generate cool SST anomalies until reaching the coast of Java, where the surface cooling begins the coupled atmosphere-ocean interactions associated with pIOD events (e.g., Li et al., 2003; Annamalai et al., 2003).

Chapter 5 made use of ocean GCM output to compute the temperature budget in the surface mixed layer for the region south of Java; for the first time, maps of the temperature budget terms in this region were produced for the onset of pIOD events, as well as box-averaged budgets for the region south of Java. The contributions of individual mesoscale processes to the temperature tendency were isolated by regressing indices representing these processes onto velocity and temperature fields. The application of this process-based decomposition allowed for much of the anomalous cooling to be explained by specific types of dynamics, indicating that local wind forcing and Kelvin waves are nearly equally important in producing anomalous cooling south of Java at the onset of positive IOD events. A warming effect from mesoscale eddies in the same region was also identified, though this was of a lesser magnitude than the cooling influences of the other processes.

The research carried out for this thesis raised some questions that are beyond the scope of this work, but may be key to interpreting the results in the larger context of global ocean and climate variability. These questions are both region-specific and globally-relevant; some of the regional questions are:

- The Kuroshio Extension jet varies on interannual timescales between a stable, weakly meandering state and an unstable, strongly meandering state, with the latter associated with much higher eddy activity (Mizuno and White, 1983; Qiu and Chen, 2005b). How do the eddy forcing patterns identified in Chapter 2 change on interannual timescales, and how might they influence the transitions

between the two states?

- Some of the results in the Java upwelling region from Chapters 4 and 5 suggest that Lombok Strait exerts an important influence on anomalous Java cooling as positive IOD events develop. However, it is difficult to separate the direct effect of the strait flow from Kelvin wave activity, as upwelling (downwelling) Kelvin waves produce a large increase (decrease) in the flow through Lombok Strait (e.g., Syamsudin et al., 2004; Drushka et al., 2010). Given the model bias in Lombok Strait flow I was wary of trying to isolate the strait contribution in Chapter 5, but previous studies have indicated that the heat flux through the strait is important to the region south of Java, at least in the seasonal cycle of near-surface temperature (e.g., Qu et al., 1994; Du et al., 2005). Could the effect of Lombok Strait outflow on Java SST be reasonably estimated by considering years during which there is relatively little Kelvin wave activity, either in observations or GCMs?

- In Chapter 5, it was found that both local wind stress forcing and Kelvin wave activity are comparable contributors to anomalous Java SST cooling; this conflicts with the observation-based result in Chapter 4 that local wind stress has little effect on Java SST anomalies at the onset of the upwelling season during pIOD years. Could inaccuracies in the wind stress products used (i.e., a $1/4^\circ$ resolution scatterometer wind product in Chapter 4, versus a 1.9° reanalysis with scatterometer corrections in Chapter 5) account for the difference obtained? Is the quality of the scatterometer wind product degraded near the coast of Java? Or can the difference be (at least partially) accounted for by Kelvin waves making a larger contribution to the conditions that are favorable for turbulent

vertical mixing?

Questions that arose from this work that have broader global implications include:

- Chapter 2 revealed an apparent association between quasi-permanent meander structure and the spatial distribution of eddy-mean flow interaction. What is the physical mechanism to explain this association between topographically-induced meanders and eddy forcing? Can a similar association be found in other mid- and high-latitude jets (e.g., Antarctic Circumpolar Current, Agulhas Return Current, North Atlantic Current)?

- The method described in Chapter 3 was developed to quantify the sea surface height signal associated only with Kelvin waves. Could a similar method be extended to effectively quantify the sea surface height signal associated with Rossby waves near the equator? Could the resulting Kelvin and Rossby wave coefficients yield new insights about nonlinear rectification of these waves and their interactions with coastlines, by comparison with idealized linear models?

- Eddy tracer fluxes (e.g., temperature fluxes) have generally been computed from the simple product of velocity and the tracer with their means removed. If an approach similar to those employed in Chapter 5 were used to target specifically the contribution of mesoscale rings, would a different picture emerge of the contributions of the eddies to regional tracer budgets? This could be done, for example, by regressing the velocity and temperature fields onto eddy-centered coordinates based on eddy tracks in the Chelton et al. (2011) dataset.

All of the questions listed above could represent useful applications of the techniques and results discussed in this thesis, and I hope to pursue some of these topics in future research.

Bibliography

Adamec, D. (1998). Modulation of the seasonal signal of the Kuroshio Extension during 1994 from satellite data. *J. Geophys. Res. 103*, 10209–10222.

Adcroft, A., C. Hill, and J. Marshall (1997). Representation of topography by shaved cells in a height coordinate ocean model. *Mon. Wea. Rev. 125*, 2293–2315.

Andrews, D. G. and M. E. McIntyre (1976). Planetary waves in horizontal and vertical shear: the generalized Eliassen-Palm relation and the mean zonal acceleration. *J. Atmos. Sci. 33*, 2031–2048.

Annamalai, H., R. Murtugudde, J. Potemra, S.-P. Xie, P. Liu, and B. Wang (2003). Coupled dynamics of the Indian Ocean: spring initiation of the Zonal Mode. *Deep-Sea Res. II 50*, 2305–2330.

Atlas, R., R. N. Hoffman, J. Ardizzone, S. M. Leidner, J. C. Jusem, D. K. Smith, and D. Gombos (2011). A cross–calibrated, multiplatform ocean surface wind velocity product for meteorological and oceanographic applications. *Bull. Amer. Meteor. Soc. 92*, 157–174.

Bell, M. J. (1999). Vortex stretching and bottom torques in the Bryan-Cox ocean circulation model. *J. Geophys. Res. 104*, 23,545–23,563.

Bingham, F. M. (1992). Formation and spreading of subtropical mode water in the North Pacific. *J. Geophys. Res. 97*, 11,177–11,189.

Bishop, S. P. (2013). Divergent eddy heat fluxes in the Kuroshio Extension at 144°-148°E. Part 2: spatiotemporal variability. *J. Phys. Oceanogr. 43*, 2416–2431.

Bishop, S. P. and F. O. Bryan (2013). A comparison of mesoscale eddy heat fluxes from observations and a high-resolution ocean model simulation of the Kuroshio Extension. *J. Phys. Oceanogr. 43*, 2563–2570.

Bishop, S. P., D. R. Watts, and K. A. Donohue (2013). Divergent eddy heat fluxes in the Kuroshio Extension at 144°-148°E. Part 1: mean structure. *J. Phys. Oceanogr. 43*, 1533–1550.

Bjerknes, J. (1969). Atmospheric teleconnections from the equatorial Pacific. *Mon. Wea. Rev. 97*, 163–172.

Boulanger, J.-P. and C. Menkes (1995). Propagation and reflection of long equatorial waves in the Pacific Ocean during the 1992–1993 El Niño. *J. Geophys. Res. 100*, 25,041–25,059.

Boulanger, J.-P. and C. Menkes (1999). Long equatorial wave reflection in the Pacific Ocean from TOPEX/POSEIDON data during the 1992–1998 period. *Clim. Dyn. 15*, 205–225.

Bower, A. S. (1989). Potential vorticity balances and horizontal divergence along particle trajectories in Gulf Stream meanders east of Cape Hatteras. *J. Phys. Oceanogr. 19*, 1669–1681.

Bower, A. S. and H. T. Rossby (1989). Evidence of cross-frontal exchange processes in the Gulf Stream based on isopycnal RAFOS float data. *J. Phys. Oceanogr. 19*, 1177–1190.

Bryan, F. and S. Bachman (2015). Isohaline salinity budget of the north Atlantic salinity maximum. *J. Phys. Oceanogr. 45*, 724–736.

Cane, M. and E. Sarachik (1976). Forced baroclinic ocean motions, I, The linear equatorial unbounded case. *J. Mar. Res. 34*, 629–665.

Cane, M. and E. Sarachik (1981). The response of a linear baroclinic equatorial ocean to periodic forcing. *J. Mar. Res. 39*, 651–693.

Charney, J. G. and M. E. Stern (1962). On the stability of internal baroclinic jets in a rotating atmosphere. *J. Atmos. Sci. 19*, 159–172.

Chelton, D. B., M. G. Schlax, and R. M. Samelson (2011). Global observations of nonlinear mesoscale eddies. *Prog. Oceanog. 91*, 167–216.

Chen, G., W. Han, Y. Li, D. Wang, and T. Shinoda (2015). Intraseasonal variability of upwelling in the equatorial Eastern Indian Ocean. *J. Geophys. Res. Oceans 120*.

Chen, R., J. L. McClean, S. T. Gille, and A. Griesel (2014). Isopycnal eddy diffusivities and critical layers in the Kuroshio Extension from an eddying ocean model. *J. Phys. Oceanogr. 44*, 2191–2211.

CNES (2010). Coastal and hydrology altimetry product (PISTACH) handbook. version 1.0, Centre National d'Études Spatiales, SALP-MU-P-OP-16031-CN.

CNES (2014). SSALTO/DUACS user handbook: (M)SLA and (M)ADT near-real time and delayed time products. version 4.1, Centre National d'Études Spatiales, SALP-MU-P-EA-21065-CLS.

de Boyer Montégut, C., G. Madec, A. S. Fischer, A. Lazar, and D. Iudicone (2004). Mixed layer depth over the global ocean: an examination of profile data and a profile–based climatology. *J. Geophys. Res. 109*, C12003.

Delcroix, T., J.-P. Boulanger, F. Masia, and C. Menkes (1994). Geosat–derived sea level and surface current anomalies in the equatorial Pacific during the 1986–1989 El Niño and La Niña. *J. Geophys. Res. 99*, 25,093–25,107.

Delman, A. S., J. L. McClean, J. Sprintall, L. D. Talley, E. Yulaeva, and S. R. Jayne (2015). Effects of eddy vorticity forcing on the mean state of the Kuroshio Extension. *J. Phys. Oceanogr. 45*, 1356–1375.

Delman, A. S., J. Sprintall, J. L. McClean, and L. D. Talley (2016a). A harmonic projection and least–squares method for quantifying Kelvin wave activity. *Ocean Sci.*. Submitted.

Delman, A. S., J. Sprintall, J. L. McClean, and L. D. Talley (2016b). Anomalous Java cooling at the initiation of positive Indian Ocean Dipole events. *J. Geophys. Res. Oceans*. In revision.

Deshpande, A., J. S. Chowdary, and C. Gnanaseelan (2014). Role of thermocline–SST coupling in the evolution of IOD events and their regional impacts. *Clim. Dyn. 43*, 163–174.

Dong, S. and K. A. Kelly (2004). Heat budget in the Gulf Stream region: the importance of heat storage and advection. *J. Phys. Oceanogr. 34*, 1214–1231.

Donohue, K., D. R. Watts, K. Tracey, M. Wimbush, J.-H. Park, N. Bond, M. Cronin, S. Chen, B. Qiu, P. Hacker, N. Hogg, S. Jayne, J. McClean, L. Rainville, H. Mitsudera, Y. Tanimoto, and S.-P. Xie (2008). Program studies of the Kuroshio extension. *EOS Trans. Amer. Geophys. Union 89*, 161–162.

Drushka, K., J. Sprintall, S. T. Gille, and I. Brodjonegoro (2010). Vertical structure of Kelvin waves in the Indonesian Throughflow exit passages. *J. Phys. Oceanogr. 40*, 1965–1987.

Du, Y., W. Cai, and Y. Wu (2013). A new type of Indian Ocean Dipole since the mid–1970s. *J. Climate 26*, 959–972.

Du, Y., K. Liu, W. Zhuang, and W.-D. Yu (2012). The Kelvin wave processes in the equatorial Indian Ocean during the 2006–2008 IOD events. *Atmos. Oceanic Sci. Lett. 5*, 324–328.

Du, Y., T. Qu, and G. Meyers (2008). Interannual variability of sea surface temperature off Java and Sumatra in a global GCM. *J. Climate 21*, 2451–2465.

Du, Y., T. Qu, G. Meyers, Y. Masumoto, and H. Sasaki (2005). Seasonal heat budget in the mixed layer of the southeastern tropical Indian Ocean in a high–resolution ocean general circulation model. *J. Geophys. Res. 110*, C04012.

Ducet, N., P. Y. L. Traon, and G. Reverdin (2000). Global high–resolution mapping of ocean circulation from TOPEX/Poseidon and ERS–1 and –2. *J. Geophys. Res. 105*, 19,477–19,498.

Emery, W. J. and R. E. Thomson (2001). *Data Analysis Methods in Physical Oceanography.* Elsevier.

Feng, M. and G. Meyers (2003). Interannual variability in the tropical Indian Ocean: a two–year time–scale of Indian Ocean Dipole. *Deep-Sea Res. II 50*, 2263–2284.

Feng, M. and S. Wijffels (2002). Intraseasonal variability in the South Equatorial Current of the East Indian Ocean. *J. Phys. Oceanogr. 32*, 265–277.

Fischer, A. S., P. Terray, E. Guilyardi, S. Gualdi, and P. Delecluse (2005). Two independent triggers for the Indian Ocean Dipole/Zonal Mode in a coupled GCM. *J. Climate 18*, 3428–3449.

Fu, L.-L., I. Fukumori, and R. N. Miller (1993). Fitting dynamic models to the Geosat sea level observations in the tropical Pacific ocean. Part II: a linear, wind–driven model. *J. Phys. Oceanogr. 23*, 2162–2181.

Gentle, J. E. (1998). *Random number generation and Monte Carlo methods*. Springer.

Giese, B. S. and D. E. Harrison (1990). Aspects of the Kelvin wave response to episodic wind forcing. *J. Geophys. Res. 95*, 7289–7312.

Gill, A. E., J. S. A. Green, and A. J. Simmons (1974). Energy partition in the large-scale ocean circulation and the production of mid-ocean eddies. *Deep-Sea Res. 21*, 499–528.

Gouretski, V. and K. P. Koltermann (2004). WOCE global hydrographic climatology. Technical Report Nr. 35, Berichte des Bundesamtes für Seeschifffahrt und Hydrographie.

Greatbatch, R. J., X. Zhai, M. Claus, L. Czeschel, and W. Rath (2010). Transport driven by eddy momentum fluxes in the Gulf Stream Extension region. *Geophys. Res. Lett. 37*, L24401.

Greene, A. D., D. R.Watts, G. G. Sutyrin, and H. Sasaki (2012). Evidence of vertical coupling between the Kuroshio Extension and topographically controlled deep eddies. *J. Mar. Res. 70*, 719–747.

Griffies, S. M., M. Winton, B. Samuels, G. Danabasoglu, S. Yeager, S. Marsland, H. Drange, and M. Bentsen (2012). Datasets and protocol for the CLIVAR WGOMD Coordinated Ocean–sea ice Reference Experiments (COREs). Technical report, CLIVAR Working Group on Ocean Model Development.

Guo, F., Q. Liu, S. Sun, and J. Yang (2015). Three types of Indian Ocean Dipoles. *J. Climate 28*, 3073–3092.

Halkides, D. J. and T. Lee (2009). Mechanisms controlling seasonal–to–interannual mixed layer temperature variability in the southeastern tropical Indian Ocean. *J. Geophys. Res. 114*, C02012.

Hall, M. M. (1991). Energetics of the Kuroshio Extension at 35°n, 152°e. *J. Phys. Oceanogr. 21*, 958–975.

Hendon, H. H., B. Liebmann, and J. D. Glick (1998). Oceanic Kelvin waves and the Madden–Julian oscillation. *J. Atmos. Sci. 55*, 88–101.

Hogg, N. G. (1994). Observations of Gulf Stream meander-induced disturbances. *J. Phys. Oceanogr. 24*, 2534–2545.

Holland, W. R. and P. B. Rhines (1980). An example of eddy-induced ocean circulation. *J. Phys. Oceanogr. 10*, 1010–1031.

Horii, T., Y. Masumoto, I. Ueki, H. Hase, and K. Mizuno (2009). Mixed layer temperature balance in the eastern Indian Ocean during the 2006 Indian Ocean dipole. *J. Geophys. Res. 114*, C07011.

Horii, T., I. Ueki, and K. Ando (2013). Contrasting development and decay processes of Indian Ocean Dipoles in the 2000s. *SOLA 9*, 183–186.

Howard, L. N. and P. G. Drazin (1964). On instability of parallel flow of inviscid fluid in a rotating system with variable Coriolis parameter. *J. Math. and Phys. 43*, 83–99.

Howe, P. J., K. A. Donohue, and D. R. Watts (2009). Stream-coordinate structure and variability of the Kuroshio Extension. *Deep-Sea Res. I 56*, 1093–1116.

Hunke, E. C. and J. K. Dukowicz (1997). An elastic-viscous-plastic model of sea ice dynamics. *J. Phys. Oceanogr. 27*, 1849–1867.

Hunke, E. C. and W. H. Lipscomb (2010). CICE: the Los Alamos sea ice model documentation and software user's manual version 4.1. Technical Report LA-CC-06-012, Los Alamos National Laboratory.

Iskandar, I., W. Mardiansyah, Y. Masumoto, and T. Yamagata (2005). Intraseasonal Kelvin waves along the southern coast of Sumatra and Java. *J. Geophys. Res. 110*, C04013.

Iskandar, I., Y. Masumoto, K. Mizuno, H. Sasaki, A. K. Affandi, D. Setiabudidaya, and F. Syamsuddin (2014). Coherent intraseasonal oceanic variations in the eastern equatorial Indian Ocean and in the Lombok and Ombai Straits from observations and a high–resolution OGCM. *J. Geophys. Res. Oceans 119*, 615–630.

Jayne, S. R., N. G. Hogg, and P. Malanotte-Rizzoli (1996). Recirculation gyres forced by a beta-plane jet. *J. Phys. Oceanogr. 26*, 492–504.

Jayne, S. R., N. G. Hogg, S. N. Waterman, L. Rainville, K. A. Donohue, D. R. Watts, K. L. Tracey, J. L. McClean, M. E. Maltrud, B. Qiu, S. Chen, and P. Hacker (2009). The Kuroshio Extension and its recirculation gyres. *Deep-Sea Res. I 56*, 2088–2099.

Johnson, B. K., F. O. Bryan, S. A. Grodsky, and J. A. Carton (2016). Climatological annual cycle of the salinity budgets of the subtropical maxima. *J. Phys. Oceanogr.*. In revision.

Kelly, K. A., L. Thompson, W. Cheng, and E. J. Metzger (2007). Evaluation of HYCOM in the Kuroshio Extension region using new metrics. *J. Geophys. Res. 112*.

Kim, S.-B., I. Fukumori, and T. Lee (2006). The closure of the ocean mixed layer temperature budget using level–coordinate model fields. *J. Atmos. Oceanic Technol. 23*, 840–853.

Kim, S.-B., T. Lee, and I. Fukumori (2004). The 1997–1999 abrupt change of the upper ocean temperature in the north central Pacific. *Geophys. Res. Lett. 31*, L22304.

Kim, S.-B., T. Lee, and I. Fukumori (2007). Mechanisms controlling the interannual variation of mixed layer temperature averaged over the Niño–3 region. *J. Climate 20*, 3822–3843.

Kuo, H.-L. (1949). Dynamic instability of two-dimensional nondivergent flow in a barotropic atmosphere. *J. Met. 6*, 105–122.

Kwon, Y.-O., C. Deser, and C. Cassou (2011). Coupled atmosphere-mixed layer ocean response to ocean heat flux convergence along the kuroshio current extension. *Clim. Dyn. 36*, 2295–2312.

Large, W. G., G. Danabasoglu, S. C. Doney, and J. C. McWilliams (1997). Sensitivity to surface forcing and boundary layer mixing in a global ocean model: annual–mean climatology. *J. Phys. Oceanogr. 27*, 2418–2447.

Large, W. G., J. C. McWilliams, and S. C. Doney (1994). Oceanic vertical mixing: a review and a model with nonlocal boundary layer parameterization. *Rev. Geophys. 32*, 363–403.

Large, W. G. and S. G. Yeager (2004). Diurnal and decadal global forcing for ocean and sea-ice models: the data sets and flux climatologies. NCAR Tech. Note. NCAR/TN-460+STR.

Large, W. G. and S. G. Yeager (2009). The climatology of an interannually-varying air sea flux data set. *Clim. Dyn. 33*, 341–364.

Lee, T., I. Fukumori, and B. Tang (2004). Temperature advection: internal versus external processes. *J. Phys. Oceanogr. 34*, 1936–1944.

Li, T., B. Wang, C.-P. Chang, and Y. Zhang (2003). A theory for the Indian Ocean Dipole–Zonal Mode. *J. Atmos. Sci. 60*, 2119–2135.

Locarnini, R. A., A. V. Mishonov, J. I. Antonov, T. P. Boyer, H. E. Garcia, O. K. Baranova, M. M. Zweng, C. R. Paver, J. R. Reagan, D. R. Johnson, M. Hamilton, and D. Seidov (2013). World Ocean Atlas 2013, Volume 1: Temperature. S. Levitus, *Ed.*, A. Mishonov, *Technical Ed.*, NOAA Atlas NESDIS 73, 40 pp.

Long, B. and P. Chang (1990). Propagation of an equatorial Kelvin wave in a varying thermocline. *J. Phys. Oceanogr. 20*, 1826–1841.

Long, R. B. and W. C. Thacker (1989a). Data assimilation into a numerical equatorial ocean model. I. The model and the assimilation algorithm. *Dyn. Atmos. Oceans 13*, 379–412.

Long, R. B. and W. C. Thacker (1989b). Data assimilation into a numerical equatorial ocean model. II. Assimilation experiments. *Dyn. Atmos. Oceans 13*, 413–439.

Maltrud, M. E., F. O. Bryan, and S. Peacock (2010). Boundary impulse response functions in a century-long eddying global ocean simulation. *Environ. Fluid Mech. 10 (1-2)*, 275–295.

Maltrud, M. E., R. D. Smith, A. J. Semtner, and A. J. Malone (1998). Global eddy-resolving ocean simulations driven by 1985-1995 atmospheric winds. *J. Geophys. Res. 103*, 30825–30853.

Mantua, N. J., S. R. Hare, Y. Zhang, J. M. Wallace, and R. C. Francis (1997). A Pacific interdecadal climate oscillation with impacts on salmon production. *Bull. Amer. Meteor. Soc. 78 (6)*, 1069–1079.

Masson, S., J.-P. Boulanger, C. Menkes, P. Delecluse, and T. Yamagata (2004). Impact of salinity on the 1997 Indian Ocean dipole event in a numerical experiment. *J. Geophys. Res. 109*, C02002.

Masson, S., P. Delecluse, J.-P. Boulanger, and C. Menkes (2002). A model study of the seasonal variability and formation mechanisms of the barrier layer in the eastern equatorial Indian Ocean. *J. Geophys. Res. 107*, 8017.

McCreary, J. P. (1981). A linear stratified model of the coastal undercurrent. *Philos. Trans. R. Soc. London A 302*, 385–413.

McDougall, T. J. and P. M. Barker (2011). *Getting started with TEOS–10 and the Gibbs Seawater (GSW) Oceanographic Toolbox*. SCOR/IAPSO WG127, ISBN 978–0–646–55621–5.

McDougall, T. J., D. R. Jackett, D. G. Wright, and R. Feistel (2003). Accurate and computationally efficient algorithms for potential temperature and density of seawater. *J. Atmos. Oceanic Technol. 20*, 730–741.

McPhaden, M. J., J. A. Proehl, and L. M. Rothstein (1986). The interaction of equatorial Kelvin waves with realistically sheared zonal currents. *J. Phys. Oceanogr. 16*, 1499–151.

McPhaden, M. J. and X. Yu (1999). Equatorial waves and the 1997–98 El Niño. *Geophys. Res. Lett. 26*, 2961–2964.

Meinen, C. S. and D. S. Luther (2003). Comparison of methods of estimating mean synoptic current structure in "stream coordinates" reference frames with an example from the Antarctic Circumpolar Current. *Deep-Sea Res. I 50*, 201–220.

Meyers, G. (1996). Variation of Indonesian throughflow and the El Niño — Southern Oscillation. *J. Geophys. Res. 101*, 12,255–12,263.

Miller, R. N. and M. A. Cane (1989). A Kalman filter analysis of sea level height in the tropical Pacific. *J. Phys. Oceanogr. 19*, 773–790.

Mizuno, K. and W. B. White (1983). Annual and interannual variability in the Kuroshio current system. *J. Phys. Oceanogr. 13*, 1847–1867.

Mizuta, G. (2009). Rossby wave radiation from an eastward jet and its recirculations. *J. Mar. Res. 67*, 185–212.

Murray, R. J. (1996). Explicit generation of orthogonal grids for ocean models. *J. Comp. Phys. 126(2)*, 251–273.

Murtugudde, R. and A. J. Busalacchi (1999). Interannual variability of the dynamics and thermodynamics of the tropical Indian Ocean. *J. Climate 12*, 2300–2326.

Murtugudde, R., J. P. McCreary, and A. J. Busalacchi (2000). Oceanic processes associated with anomalous events in the Indian Ocean with relevance to 1997–1998. *J. Geophys. Res. 105*, 3295–3306.

Nagura, M. and M. J. McPhaden (2010). Dynamics of zonal current variations associated with the Indian Ocean dipole. *J. Geophys. Res. 115*, C11026.

Niiler, P. P., N. A. Maximenko, G. G. Panteleev, T. Yamagata, and D. B. Olson (2003). Near-surface dynamical structure of the Kuroshio Extension. *J. Geophys. Res. 108*, 3193.

Ogata, T. and Y. Masumoto (2010). Interactions between mesoscale eddy variability and Indian Ocean dipole events in the southeastern tropical Indian Ocean—case studies for 1994 and 1997/1998. *Ocean Dyn. 60*, 717–730.

Pratt, L. J., J. Earles, P. Cornillon, and J.-F. Cayula (1991). The nonlinear behavior of varicose disturbances in a simple model of the Gulf Stream. *Deep-Sea Res. 38*, S591–S622.

Qiu, B. and S. Chen (2005a). Eddy-induced heat transport in the subtropical North Pacific from Argo, TMI, and altimetry measurements. *J. Phys. Oceanogr. 35*, 458–473.

Qiu, B. and S. Chen (2005b). Variability of the Kuroshio Extension jet, recirculation gyre, and mesoscale eddies on decadal time scales. *J. Phys. Oceanogr. 35*, 2090–2103.

Qiu, B. and S. Chen (2010). Eddy-mean flow interaction in the decadally modulating Kuroshio Extension system. *Deep-Sea Res. II 57*, 1097–1110.

Qiu, B., S. Chen, P. Hacker, N. G. Hogg, S. R. Jayne, and H. Sasaki (2008). The Kuroshio Extension northern recirculation gyre: profiling float measurements and forcing mechanism. *J. Phys. Oceanogr. 38*, 1764–1779.

Qiu, B. and K. A. Kelly (1993). Upper–ocean heat balance in the Kuroshio Extension region. *J. Phys. Oceanogr. 23*, 2027–2041.

Qiu, Y., W. Cai, L. Li, and X. Guo (2012). Argo profiles variability of barrier layer in the tropical Indian Ocean and its relationship with the Indian Ocean Dipole. *Geophys. Res. Lett. 39*, L08605.

Qu, T. (2003). Mixed layer heat balance in the western north Pacific. *J. Geophys. Res. 108*, 3242.

Qu, T., G. Meyers, J. S. Godfrey, and D. Hu (1994). Ocean dynamics in the region between Australia and Indonesia and its inflluence on the variation of sea surface temperature in a global general circulation model. *J. Geophys. Res. 99*, 18,433–18,445.

Reynolds, R. W. (2009). What's new in version 2. National Climatic Data Center, National Oceanic and Atmospheric Administration, 10 pp.

Reynolds, R. W., T. M. Smith, C. Liu, D. B. Chelton, K. S. Casey, and M. G. Schlax (2007). Daily high–resolution-blended anlyses for sea surface temperature. *J. Climate 20*, 5473–5496.

Roxy, M., S. Gualdi, H.-Y. L. Drbohlav, and A. Navarra (2011). Seasonality in the relationship between El Nino and Indian Ocean dipole. *Clim. Dyn. 37*, 221–236.

Saji, N. H., B. N. Goswami, P. N. Vinayachandran, and T. Yamagata (1999). A dipole mode in the tropical Indian Ocean. *Nature 401*, 360–363.

Samelson, R. M. and J. Pedlosky (1990). Local baroclinic instability of flow over variable topography. *J. Fluid Mech. 221*, 411–436.

Schiller, A., S. E. Wijffels, J. Sprintall, R. Molcard, and P. R. Oke (2010). Pathways of intraseasonal variability in the Indonesian Throughflow region. *Dyn. Atmos. Oceans 50*, 174–200.

Shay, T. J., J. M. Bane, D. R. Watts, and K. L. Tracey (1995). Gulf Stream flow field and events near 68°W. *J. Geophys. Res. 100*, 22565–22589.

Smith, R. and P. Gent (2002). Reference manual for the Parallel Ocean Program (POP). Technical Report LAUR-02-2484, Los Alamos National Laboratory, and National Center for Atmospheric Research.

Smith, R., P. Jones, B. Briegleb, F. Bryan, G. Danabasoglu, J. Dennis, J. Dukowicz, C. Eden, B. Fox-Kemper, P. Gent, M. Hecht, S. Jayne, M. Jochum, W. Large, K. Lindsay, M. Maltrud, N. Norton, S. Peacock, M. Vertenstein, and S. Yeager (2010). The Parallel Ocean Program (POP) reference manual. Technical Report LAUR-10-01853, Los Alamos National Laboratory, and National Center for Atmospheric Research.

Song, Q., G. A. Vecchi, and A. J. Rosati (2007). Indian Ocean variability in the GFDL coupled climate model. *J. Climate 20*, 2895–2916.

Sprintall, J., A. L. Gordon, R. Murtugudde, and R. D. Susanto (2000). A semiannual Indian Ocean forced Kelvin wave observed in the Indonesian seas in May 1997. *J. Geophys. Res. 105*, 17,217–17,230.

Sprintall, J. and A. Révelard (2014). The Indonesian Throughflow response to Indo–Pacific climate variability. *J. Geophys. Res. Oceans 119*, 1161–1175.

Sprintall, J. and D. Roemmich (1999). Characterizing the structure of the surface layer in the Pacific Ocean. *J. Geophys. Res. 104*, 23,297–23,311.

Sprintall, J. and M. Tomczak (1992). Evidence of the barrier layer in the surface layer of the tropics. *J. Geophys. Res. 97*, 7305–7316.

Sprintall, J., S. E. Wijffels, R. Molcard, and I. Jaya (2009). Direct estimates of the Indonesian Throughflow entering the Indian Ocean: 2004–2006. *J. Geophys. Res. 114*, C07001.

Susanto, R. D., A. L. Gordon, and Q. Zheng (2001). Upwelling along the coasts of Java and Sumatra and its relation to ENSO. *Geophys. Res. Lett. 28*, 1599–1602.

Susanto, R. D., Q. Zheng, and X.-H. Yan (1998). Complex singular value decomposition analysis of equatorial waves in the Pacific observed by TOPEX/Poseidon altimeter. *J. Atmos. Oceanic Technol. 15*, 764–774.

Syamsudin, F. and A. Kaneko (2013). Ocean variability along the southern coast of Java and Lesser Sunda Islands. *J. Oceangr. 69*, 557–570.

Syamsudin, F., A. Kaneko, and D. B. Haidvogel (2004). Numerical and observational estimates of Indian Ocean Kelvin wave intrusion into Lombok Strait. *Geophys. Res. Lett. 31*, L24307.

Taguchi, B., B. Qiu, M. Nonaka, H. Sasaki, S.-P. Xie, and N. Schneider (2010). Decadal variability of the Kuroshio Extension: mesoscale eddies and recirculations. *OD 60*, 673–691.

Talley, L. D. (1983a). Radiating barotropic instability. *J. Phys. Oceanogr. 13*, 972–987.

Talley, L. D. (1983b). Radiating instabilities of thin baroclinic jets. *J. Phys. Oceanogr. 13*, 2161–2181.

Thacker, W. C. and R. B. Long (1988). Fitting dynamics to data. *J. Geophys. Res. 93*, 1227–1240.

Thomas, L. N. and T. M. Joyce (2010). Subduction on the northern and southern flanks of the Gulf Stream. *J. Phys. Oceanogr. 40*, 429–438.

Tracey, K. L., D. R. Watts, K. A. Donohue, and H. Ichikawa (2012). Propagation of Kuroshio Extension meanders between 143°E and 149°E. *J. Phys. Oceanogr. 42*, 581–601.

Vinayachandran, P. N., S. Iizuka, and T. Yamagata (2002). Indian Ocean dipole mode events in an ocean general circulation model. *Deep-Sea Res. II 49*, 1573–1596.

Vinayachandran, P. N., N. H. Saji, and T. Yamagata (1999). Response of the Equatorial Indian Ocean to an unusal wind event during 1994. *Geophys. Res. Lett. 26*, 1613–1616.

Wang, Y., J. Lan, and F. Cui (2014). Effect of nonlinear advection on the Indian Ocean dipole asymmetry. *Acta Oceanol. Sin. 33*, 77–82.

Waterman, S. N., N. G. Hogg, and S. R. Jayne (2011). Eddy-mean flow interaction in the Kuroshio Extension region. *J. Phys. Oceanogr. 41*, 1182–1208.

Waterman, S. N. and B. J. Hoskins (2013). Eddy shape, orientation, propagation, and mean flow feedback in western boundary current jets. *J. Phys. Oceanogr. 43*, 1666–1690.

Waterman, S. N. and S. R. Jayne (2011). Eddy-mean flow interaction in the along-stream development of a western boundary current jet: An idealized model study. *J. Phys. Oceanogr. 41*, 682–707.

Webster, P. J., A. M. Moore, J. P. Loschnigg, and R. R. Leben (1999). Coupled ocean–atmosphere dynamics in the Indian Ocean during 1997–98. *Nature 401*, 356–360.

White, W. B. and J. P. McCreary (1976). On the formation of the Kuroshio meander and its relationship to the large-scale ocean circulation. *Deep-Sea Res. 23*, 33–47.

Williams, R. G., C. Wilson, and C. W. Hughes (2007). Ocean and atmosphere storm tracks: the role of eddy vorticity forcing. *J. Phys. Oceanogr. 37*, 2267–2289.

Wunsch, C. (1999). Where do ocean eddy heat fluxes matter? *J. Geophys. Res. 104*, 13235–13249.

Wyrtki, K. (1962). The upwelling in the region between Java and Australia during the south–east monsoon. *Austr. J. Mar. Freshwat. Res. 13*, 217–225.

Xiang, B., W. Yu, T. Li, and B. Wang (2011). The critical role of the boreal summer mean state in the development of the IOD. *Geophys. Res. Lett. 38*, L02710.

Xie, S.-P., H. Annamalai, F. A. Schott, and J. P. McCreary (2002). Structure and mechanisms of south Indian Ocean climate variability. *J. Climate 15*, 864–878.

Yeager, S. G. (2013). *Understanding and predicting changes in North Atlantic Sea Surface Temperature.* Ph. D. thesis, U. of Colorado.

Young, W. R. (2012). An exact thickness-weighted average formulation of the Boussinesq equations. *J. Phys. Oceanogr. 42*, 692–707.

Yu, X. and M. J. McPhaden (1999). Seasonal variability in the equatorial Pacific. *J. Phys. Oceanogr. 29*, 925–947.

Yu, Z. and J. Potemra (2006). Generation mechanism for the intraseasonal variability in the Indo-Australian basin. *J. Geophys. Res. 111*, C01013.

Yuan, D. and H. Liu (2009). Long-wave dynamics of sea level variations during Indian Ocean Dipole events. *J. Phys. Oceanogr. 39*, 1115–1132.

Yuan, D., M. M. Rienecker, and P. S. Schopf (2004). Long-wave dynamics of the interannual variability in a numerical hindcast of the equatorial Pacific Ocean circulation during the 1990s. *J. Geophys. Res. 109*, C05019.

Yulaeva, E., N. Schneider, D. W. Pierce, and T. P. Barnett (2001). Modeling of north Pacific climate variability forced by oceanic heat flux anomalies. *J. Climate 14*, 4027–4046.

Zhong, A., H. H. Hendon, and O. Alves (2005). Indian Ocean variability and its association with ENSO in a global coupled model. *J. Climate 18*, 3634–3649.

Zweng, M. M., J. R. Reagan, J. I. Antonov, R. A. Locarnini, A. V. Mishonov, T. P. Boyer, H. E. Garcia, O. K. Baranova, D. R. Johnson, D. Seidov, and M. M. Biddle (2013). World Ocean Atlas 2013, Volume 2: Salinity. S. Levitus, *Ed.*, A. Mishonov, *Technical Ed.*, NOAA Atlas NESDIS 74, 39 pp.